Charles University in Prague
Faculty of Mathematics and Physics

MASTER THESIS

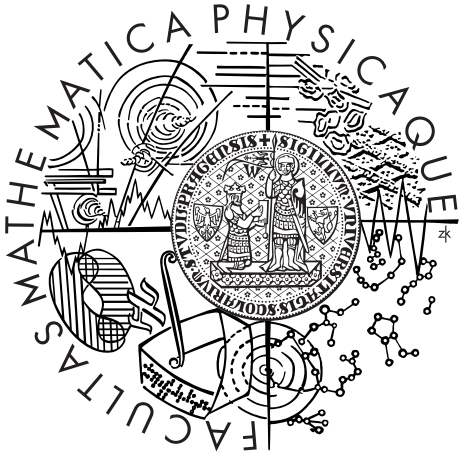

Bc. Emil Varga

Steady state and decay of quantum turbulence generated in channel flows and detected by second sound attenuation

Department of Low Temperature Physics

Supervisor of the master thesis:	prof. RNDr. Ladislav Skrbek, DrSc.
Consultant of the master thesis:	Simone Babuin, Ph.D.
Study programme:	Physics
Specialization:	physics of condensed matter and materials

Prague 2014

I would like to thank my supervisor L. Skrbek and my consultant S. Babuin for a lot of invaluable help throughout the duration of the master programme. The work presented in this thesis was supported by a grant of the Granting Agency of the Charles University in Prague under GAUK No. 366213.

I declare that I carried out this master thesis independently, and only with the cited sources, literature and other professional sources.

I understand that my work relates to the rights and obligations under the Act No. 121/2000 Coll., the Copyright Act, as amended, in particular the fact that the Charles University in Prague has the right to conclude a license agreement on the use of this work as a school work pursuant to Section 60 paragraph 1 of the Copyright Act.

In Prague date 3rd April 2014 signature of the author

Název práce: Steady state and decay of quantum turbulence generated in channel flows and detected by second sound attenuation

Autor: Bc. Emil Varga

Katedra: Katedra fyziky nízkých teplot

Vedoucí diplomové práce: prof. RNDr. Ladislav Skrbek, DrSc., KFNT

Konzultant diplomové práce: Simone Babuin, Ph.D., Fyzikální Ústav, AVČR

Abstrakt: Kvantová turbulencia je študovaná v supratekutom ^{4}He za klasického prúdenia. Turbulencia je generovaná prúdením cez 7×7 mm štvorcový kanál s regularizáciou prúdenia na vtoku buď s dodatočnou mriežkou alebo bez nej. Prúdenie je vyvolané mechanicky, stláčaním nerezového vlnovca. Hustota vírových čiar je meraná pomocou tlmenia druhého zvuku v ustálenom stave a v rozpade turbulencie v rozmedzí teplôt 1.17 – 2.16 K. V ustálenom stave je pozorované teplotne nezávislé škálovanie hustoty vírových čiar s rýchlosťou prúdu v tvare $L \propto V^{3/2}$. V rozpade je pozorovaná, pre veľké časy, pre mriežkovú turbulenciu typická závislosť $L \propto t^{-3/2}$. Oboje pozorovania sú vysvetlené na základe kvazi-klasického modelu kvantovej turbulencie, ktorý dovoľuje výpočet efektívnej kinematickej viskozity supratekutého hélia $\nu_{\mathtt{eff}}$. Tieto zhruba súhlasia s hodnotami dostupnými v literatúre. Taktiež sú vyvinuté dva modely založené na teórií protiprúdu a je tiež študovaný vplyv nehomogenity rozloženia hustory vírových čiar na meraciu techniku.

Klíčová slova: supratekuté hélium, kvantová turbulencia, druhý zvuk

Title: Steady state and decay of quantum turbulence generated in channel flows and detected by second sound attenuation

Author: Bc. Emil Varga

Department: Department of low temperature physics

Supervisor: prof. RNDr. Ladislav Skrbek, DrSc., KFNT

Consultant: Simone Babuin, Ph.D., Institute of Physics, AVČR

Abstract: Quantum turbulence is studied in superfluid ^{4}He under classical flow conditions. Turbulence is generated by a flow through a 7×7 mm square channel with a flow conditioner either with an additional grid or without it. The flow is generated mechanically by squeezing a stainless steel bellows. Vortex line density is measured by attenuation of second sound in both steady state and decay for a range of temperatures 1.17 – 2.16 K. In the steady state, temperature-independent scaling of the vortex line density with flow velocity of the form $L \propto V^{3/2}$ is observed. In the decay the expected late-time behaviour $L \propto t^{-3/2}$ is observed. Explanation for both of these observations is based on a quasi-classical model of quantum turbulence, that allows the extraction of the effective kinematic viscosity $\nu_{\mathtt{eff}}$, which approximately agree with the values available in the literature. Two models based on counterflow theory are also explored and the effect of inhomogeneous vortex line distribution on the measurement technique is studied.

Keywords: superfluid helium, quantum turbulence, second sound

Contents

Introduction

Turbulence in fluids is an important problem of classical physics, which, even after centuries of research, is yet to be solved satisfactorily. Providing a definition of turbulence that is both general enough to encompass the immense wealth of experimental phenomena of classical fluid dynamics and yet one that is not too vague and nebulous proves problematic. However, it is certain that turbulence involves complicated flows on a range of spatial scales that are non-trivially correlated in both space and time. The last point implies that, while turbulence is chaotic, it is not in general random. In turbulent systems *coherent objects*, often spontaneously, emerge. The most easily appreciable of such coherent objects are the vortices that emerge as features of vorticity, or the curl of the velocity field, which is an important quantity for dissipation of the turbulent kinetic energy and the vortices themselves are in turn of an utmost importance to the energy transfer between varying spatial scales.

The presented thesis explores the turbulence in a classical setup with a non-classical medium, superfluid ^{4}He. Superfluid helium, historically called the He-II, is a phase into which liquid helium enters at around 2.17 K at saturated vapour pressure, the so-called λ point. While liquid helium above the λ-transition (the He-I henceforth) is an ordinary liquid, albeit one that has a very small viscosity, in the He-II several effects inexplicable by classical physics are observed. For example, the lack of internal friction (viscosity) under certain circumstances, an effect that influenced the name of the phase in analogy to the superconductivity, or the quantization of circulation (a loop integral of velocity field); again, a similar phenomenon, the quantization of magnetic flux, is observed in superconductivity. Turbulence in superfluid ^{4}He, and other similar media, is referred to as *quantum turbulence*. The need for the separate name indicates important differences from the turbulence in classical fluids, which shall be addressed further in the following chapter.

The work presented in this thesis are two series of experiments with mechanically forced flows in a channel with square cross section and with two different configurations of a grid upstream from the detecting apparatus. An understanding of the observed behaviour in terms of several possible theoretical models is attempted, with an emphasis on a modification of a model developed for a quasi-classical behaviour of homogeneous and isotropic quantum turbulence in decay in [1, 2].

The thesis is structured as follows: chapter one provides necessary information

on the known fundamental properties of superfluidity and quantum turbulence for explanation of the measuring technique and also describes the experimental apparatus and protocol; chapter two presents the acquired experimental data; chapter three explores the theoretical models after which the conclusions of the thesis follow.

1. Essentials of superfluidity and the description of the experiment

1.1 Essential properties of superfluid ^{4}He

1.1.1 Overview of the microscopic concepts

When cooled below approximately 2.17 K at saturated vapour pressure, liquid ^{4}He undergoes a second-order phase transition and becomes superfluid. Historically, this phase is called He-II (and He-I above the transition). At pressures not exceeding some critical value, the liquid remains in this phase down to absolute zero. Thus, helium at saturated vapor pressure never solidifies as can be seen in the phase diagram in Fig. 1.1.

The ^{4}He atoms have a nucleus of two protons and two neutrons and a single filled $s-$orbital of electrons. The total spin of this system is 0, thus ^{4}He is a boson (unlike the fermionic isotope ^{3}He). As a consequence of this bosonic nature, superfluidity has been linked to the Bose-Einstein condensation since the earliest beginnings of the investigation of the phenomenon. Even though the microscopic theory of superfluidity is not available yet, the concept of Bose-Einstein condensation as a basis of superfluidity led to many important insights.

The idea that a macroscopic amount of particles resides in a single quantum state led to the description of the entirety a sample of He-II (at 0 K) with a *macroscopic wave-function*,

$$\Psi(\boldsymbol{r}) = \sqrt{\frac{\rho(\boldsymbol{r})}{m_4}} e^{iS(\boldsymbol{r})}, \tag{1.1}$$

where $\rho(\boldsymbol{r})$ is the density ^{4}He of at point $\boldsymbol{r}$, m_4 is the mass of ^{4}He atom and $S(\boldsymbol{r})$ the phase at point $\boldsymbol{r}$. In most cases incompressibility can be assumed, i.e., $\rho(\boldsymbol{r}) = \rho$. The above equation holds at 0 K, when only the base state (and few excited states due to interatomic interactions) is occupied. At non-zero temperatures some atoms are thermally excited and the set of atoms is separated (in momentum space) to those belonging to the condensate and those thermally excited. The normalisation of (1.1) then changes to include only the particles of the condensate, i.e. the total density is replaced by some superfluid density $\rho_s \leq \rho$. The rest of this subsection is concerned only with the part of ^{4}He described by (1.1).

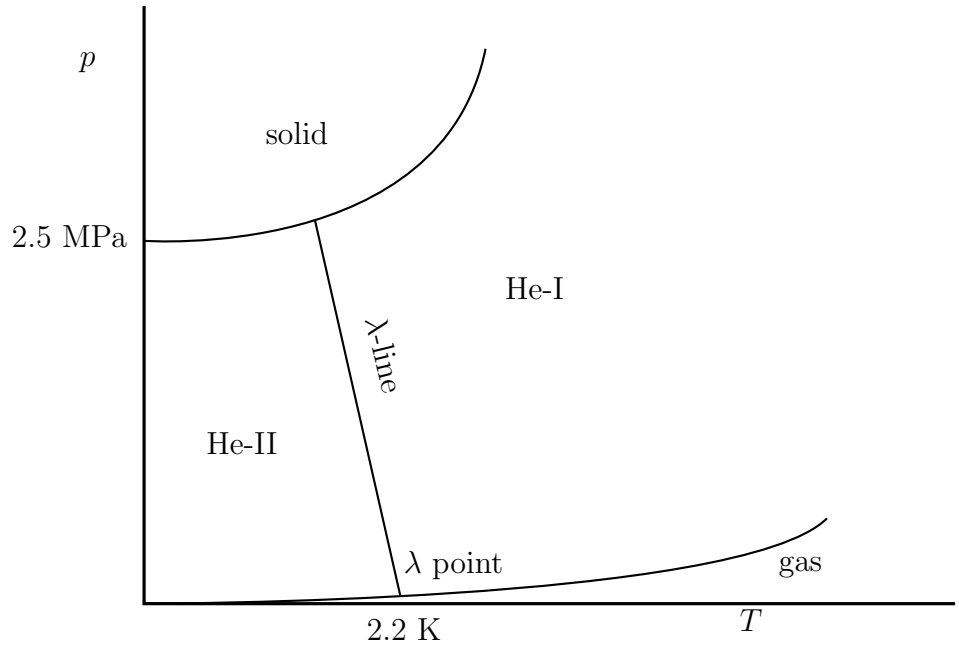

Figure 1.1: A sketch of the phase diagram of ^{4}He. For pressures less than approximately 25 bar, ^{4}He never solidifies. The vertical "λ-line" indicates the superfluid phase transition.

The velocity field $\boldsymbol{v}(\boldsymbol{r})$ (that is, the velocity in the Eulerian sense of continuum mechanics) is an eigenfunction of the standard quantum mechanical momentum operator of a single atom,

$$\boldsymbol{v}(\boldsymbol{r}) = \frac{1}{\Psi}\frac{-i\hbar\nabla}{m_4}\Psi = \frac{\hbar}{m_4}\nabla S(\boldsymbol{r}). \tag{1.2}$$

The flow is thus potential. The circulation Γ of this velocity around any closed contour $\mathcal{C}$ is then

$$\Gamma_{\mathcal{C}} = \oint_{\mathcal{C}} \boldsymbol{v}(\boldsymbol{r}) \cdot \mathrm{d}\,\boldsymbol{r} = \frac{\hbar}{m_4}\oint_{\mathcal{C}} \nabla S(\boldsymbol{r})\,\mathrm{d}\,\boldsymbol{r} = n\frac{2\pi\hbar}{m_4} = n\kappa, \quad n \in \mathbb{N}, \tag{1.3}$$

where $\kappa = h/m_4$ is the *quantum of circulation* and h is the Planck's constant. In a simply connected region n would be identically zero for arbitrary $\mathcal{C}$.

However, as was first envisioned by L. Onsager, He-II develops *quantised vortices* (or *vortex lines*), very thin (Å-sized) line defects where superfluidity is suppressed and around which the circulation is allowed to be non-zero. Since the vortices change the connectedness of a region of He-II they are often referred to as the topological defects. This requires that the vortices begin and end on the boundaries of the fluid or form closed loops.

The energy E of a vortex line per unit length is given by the kinetic energy of the flow around it, from which follows that $E \propto (n\kappa)^2$, thus only singly-quantised

$n = 1$ vortices commonly exist in the nature, since, for example, two singly-quantised lines require half the energy that a single doubly-quantised line while providing the same circulation. Quantised vortices interact with the quasiparticle thermal excitations (discussed further later in this chapter), other vortices and themselves. The vortex-vortex interaction is either through advection by the velocity field or through *reconnections*, which happen when two vortices (or two parts of the same vortex) approach sufficiently close together. In these events the vortex lines reconnect, i.e., if one vortex connects two points $A - B$ far from the point of reconnection and the second vortex connects $C - D$, the connectedness of the points after the reconnection could be either $A - C$ and $B - D$ or $A - D$ and $B - C$.

The existence of the quantised vortices has far-reaching consequences on the behaviour of the superfluid helium. One of the first examples were experiments with rotating buckets of He-II. Without the quantised vortices, the meniscus that develops on the fluid surface would be shallower than predicted by classical fluid mechanics, as it would be created only by the thermally excited subset of He-II. Experimentally observed fluid surface is, however, almost indistinguishable frome the classical prediction. This is possible due to quantised vortices creating a regular lattice threading the bulk of the liquid mimicking the classical solid body rotation of the fluid.

Probably the most important consequence of the existence of vortex lines is the possibility of turbulence in superfluid helium, since turbulence is not possible in potential flows. The turbulence, commonly referred to as *quantum turbulence*, takes the form of a complex *tangle of vortex lines* [3] capable of supporting, for example, turbulent energy cascade akin to the classical counterpart. The most commonly used characterisation of quantum turbulence in this thesis is the *vortex line density* L defined as the total length of vortex lines per unit volume.

This subsection provides only the basic ideas and terminology of superfluidity in ^{4}He and is not meant to be in any sense exhaustive. For more information see [4, 5, 6].

1.1.2 Two-fluid phenomenology

The most succesfull phenomenological model describing the properties of superfluid ^{4}He is the two-fluid model due to Landau and Tisza. The model describes superfluid ^{4}He as an intimate mixture of two components within the liquid – the normal (formed by the quasiparticle thermal excitations) and the superfluid component (formed by the condesnate). The superfluid component has zero viscosity

and carries no entropy while the normal component carries the entire entropy of the liquid and has non-zero viscosity. Each component of the liquid has a density associated with it, and the total density ρ of LHe is given by

$$\rho = \rho_s + \rho_n, \tag{1.4}$$

where ρ_s and ρ_n are the densities of the superfluid and normal component respectively. Each component also has a velocity field associated with it, which are coupled through the so-called mutual friction, but otherwise behave independently. It should be pointed out that due to zero viscosity of the superfluid component the two fluids presumably obey different boundary conditions at solid walls (zero velocity at a stationary wall for normal fluid, zero cartesian component of the velocity normal to the wall for the superfluid). The equations analogous to Navier-Stokes equations describing the evolution of the velocity fields for the superfluid and normal fluid (sometimes called the *Landau equations*) are

$$\begin{aligned} \rho_s \left(\frac{\partial \boldsymbol{v}_s}{\partial t} + (\boldsymbol{v}_s \cdot \nabla) \boldsymbol{v}_s \right) &= -\frac{\rho_s}{\rho} \nabla p + \rho_s s \nabla T - \boldsymbol{F}_{ns}, \\ \rho_n \left(\frac{\partial \boldsymbol{v}_n}{\partial t} + (\boldsymbol{v}_n \cdot \nabla) \boldsymbol{v}_n \right) &= -\frac{\rho_n}{\rho} \nabla p - \rho_s s \nabla T + \mu \Delta \boldsymbol{v}_n + \boldsymbol{F}_{ns}, \end{aligned} \tag{1.5}$$

where index n means normal fluid component and s the superfluid component, p is pressure, s the entropy per unit mass, T the temperature, μ is the normal fluid dynamic viscosity and

$$F_{ns} = B \frac{\rho_n \rho_s}{2\rho} \hat{\boldsymbol{\omega}} \times (\boldsymbol{\omega} \times (\boldsymbol{v}_n - \boldsymbol{v}_s)) + B' \frac{\rho_n \rho_s}{2\rho} \boldsymbol{\omega} \times (\boldsymbol{v}_n - \boldsymbol{v}_s) \tag{1.6}$$

is the mutual friction[7], where B and B' are temperature-dependent mutual friction parameters and $\boldsymbol{\omega} = \nabla \times \boldsymbol{v}_s$ (with $\hat{\boldsymbol{\omega}} = \boldsymbol{\omega}/|\boldsymbol{\omega}|$) is the superfluid vorticity. It is usually assumed that, at least locally, the magnitude of superfluid circulation is given by vortex line density $\omega = \kappa L$. These equations are in fact a simplified form of the more general HVBK equations (after Hall, Vinen, Bekarevich and Khalatnikov), for more details see [8]. Note that $\boldsymbol{v}_s$ in these equation is not the same as in microscopic relations, which is always irrotational. The $\boldsymbol{v}_s$ in HVBK equations is a result of coarse graining of the microscopic velocity field and thus is allowed to have non-zero curl. The scale of coarse graining is such that the quantised nature of the vortices becomes irrelevant, i.e. it is sufficiently larger than the inter-vortex distance $\delta = L^{-1/2}$.

Together with the equations of continuity for each component and the conservation of entropy (i.e., adiabatic flow) equations (1.5) account for the most of the observed phenomena of superfluidity of ^{4}He, of which the most important one

for the present purposes is the existence of the *second sound* (information on the fascinating thermo-mechanical effects occurring in superfluid ^{4}He can be found in [4, 5]). Second sound, as the name suggests, is a wave process in He-II. Normal everyday sound is a wave of pressure or density in the sound-carrying medium, which, of course, also exists in He-II under the name first sound. Second sound are, again, waves of density of the two components which are, however, out of phase, i.e. regions of increased density of either the superfluid or the normal fluid component alternate in space, while the total density ρ remains constant. Since the temperature or entropy density are uniquely determined by the ratio of normal and superfluid densities, second sound can be also seen as a wave of temperature or entropy.

1.1.3 Second-sound attenuation

Microscopically, the normal fluid is composed of quasiparticle thermal excitations in the system (in the temperature range where superfluidity exists these are mostly acoustic phonons). These quasiparticles can be scattered by the cores of quantised vortices. Second sound can be seen as a coherent movement of a large number of such quasiparticles. Random scattering of excitations constituting the second sound will only increase the density of the normal fluid, that is, the temperature. Second sound is thus attenuated by the presence of quantised vortices in the medium where the second sound propagates.

It can be shown (see the appendix in [9] (reproduced in Attachment 1) and also the Appendix A of the thesis) from (1.5) that, to within leading-order approximation, for a plane second sound wave the velocity difference between the normal and superfluid components $w = v_n - v_s$ is exponentially attenuated as it propagates (in positive x direction)

$$w = v_n - v_s \propto e^{-\alpha x} e^{i(\omega_s t - kx)}, \tag{1.7}$$

where k is the wave vector and ω_s is the frequency of the second sound. Furthermore it can be shown, assuming homogeneous vortex tangle, that in a continually driven second sound resonator the density of vortex lines is sufficiently accurately given by (see also Fig. 1.5, left)

$$L = \frac{6\pi\Delta}{B\kappa}\left(\frac{A_0}{A} - 1\right), \tag{1.8}$$

where A is the amplitude of the second sound in the resonance, A_0 is the same quantity while no vortices are present, Δ is the resonance width (the width parameter of a Lorenzian curve which describes the frequency dependence of the

component of the response in-phase with the drive). To derive (1.8), an assumption about the orientation of the vortex lines is necessary. Since the orientation of the lines is unknown, the intrinsic uncertainty on L calculated by (1.8) is about 33%.

Formula (1.8) forms the basis of the experimental technique. Second sound standing wave is generated (more details on how is this done in the following section) in a flow channel which acts as a resonator while the helium is quiescent (it is assumed that negligible number of vortex lines is present) and the frequency dependence of the response is scanned, yielding parameters Δ and A_0 in the equation (1.8) (see Fig. 1.5). After generating the turbulence, and thus the tangle of quantised vortices, it is sufficient to measure the amplitude A of the response in the resonance to determine the vortex line density. The last point requires that the resonant frequency does not shift after the turbulence is generated, which was verified to be the case.

1.2 Experimental apparatus and protocol

1.2.1 Description of the apparatus

Turbulence is generated in a brass channel with square cross-section of side-length 7 mm, see Fig. 1.2 for dimensions and Fig. 1 in [9] (in Attachment 1) for the overview of arrangement. The downstream end of the channel is opened to LHe bath. The upstream end is connected to stainless steel bellows which, upon squeezing, acts as a flow source. Both the bellows and the channel are immersed in LHe bath. The connection is through a bent brass pipe and a separating plastic piece necessary for electrical insulation. To prevent the possible advection of large scale eddies generated by the bend in the connecting pipe into the channel, a flow conditioner is installed at the entry to the channel. This flow conditioner consists of a stack of stainless steel capillaries of internal diameter of about 1 mm and length about 5 mm. The bellows is operated by a computer-controlled linear motor mounted on the cryostat flange. The volume of the bellows is calibrated against the coordinate of the motor that allows calculation of velocity inside the channel to within 3% precision.

The second sound detection setup consists of two approximately identical devices, sketched on Fig. 1.3, one of which is used to excite the second sound and the other to detect it. The mode of operation depends simply on whether a signal generator or a lock-in amplifier is connected to the device. The essential functional

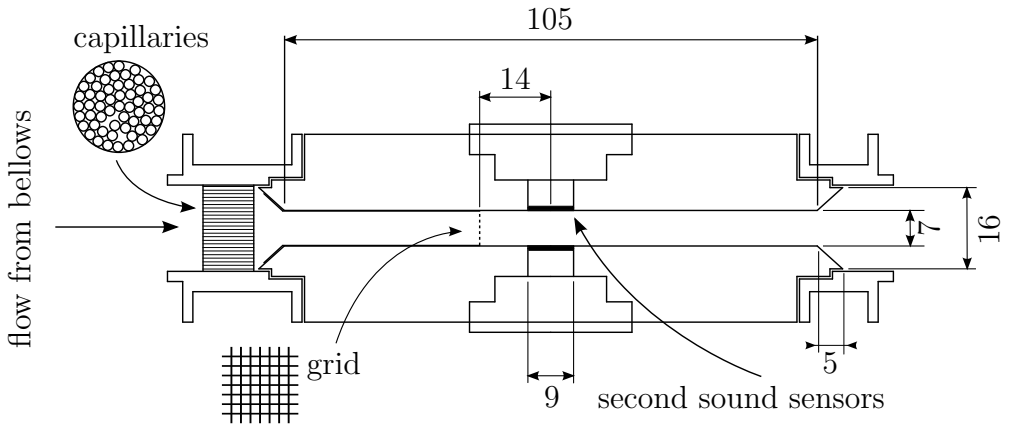

Figure 1.2: Geometry of the channel, given dimensions are in mm. The figure is to scale, except for the flow conditioner and grid sketches. The length of the capillaries in the flow conditioner is about 10 mm with internal width of about 1 mm. The grid has a 0.6 mm mesh with 0.1 mm wide tines (the gaps being 0.5 mm). In the experiment, the channel is oriented vertically with flow being from the bottom. See also Fig. 1 in [9] (Attachment 1).

parts of the sensor assembly are the stationary brass electrode and the Nuclepore membrane. The brass electrode is electrically insulated from the channel body and is connected to the input/output wire of the sensor. The membrane is gold-plated on the side facing away from the electrode and is electrically connected with the channel body. The channel body, and thus the membrane, is biased against the electrode by a DC voltage of 100 V. Connecting a harmonic AC voltage to the excitation device causes the membrane to oscillate. This oscillatory motion displaces mostly only the normal fluid component of the He-II, since the μm-sized holes in the membrane are large enough for the superfluid to move freely through the membrane. This causes the oscillation in local density of the normal fluid and the superfluid, i.e., the second sound. On the detecting device, the reverse process induces an AC voltage on the electrode, that is detected using a phase-sensitive lock-in amplifier synchronised to the excitation frequency. See the diagram on Fig. 1.3.

Essential for meaningful measurements is the temperature control. Cooling is provided by pumping the He vapours above the bath by a rotary vane pump alone or in series with a Roots pump, which can reach a temperature down to 1.16 K. Pumping can be only regulated through a manually operated valve, that is not suitable for achieving sufficiently stable temperature. For this purpose a control heater of about 50 Ω is placed in the bath and is connected to a computer-controlled DC current source. The current J to the heater is controlled by the

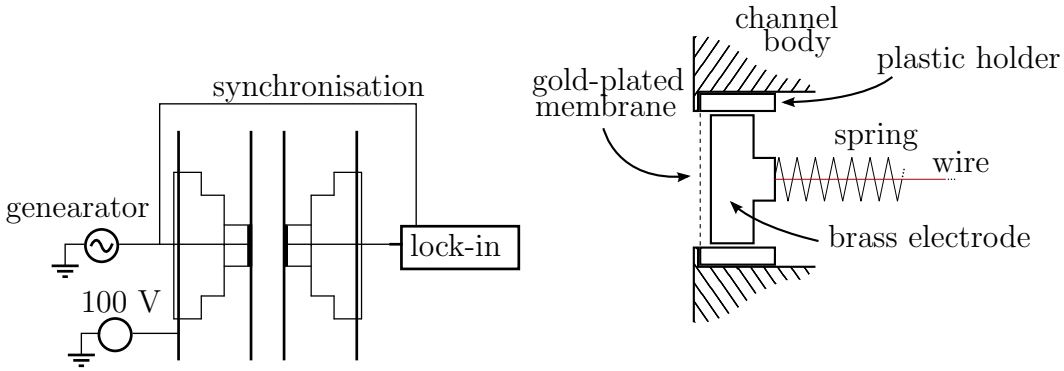

Figure 1.3: The diagram of the detecting apparatus (left) and the detail of the second sound sensor assembly (right).

proportional-integral algorithm

$$J(t) = P(T^* - T(t)) + I \int_{t_0}^{t} (T^* - T(t)) \, \mathrm{d}\, t, \tag{1.9}$$

where t is time, T^* is the desired temperature, $T(t)$ is the measured temperature, t_0 is manually chosen time origin and P and I are proportional and integral parameters.[1] If the current output were to be negative, it is set to zero. In practice, the pumping rate is manually set (with temperature control off) so that the dynamic equilibrium for the temperature is somewhat below the desired temperature T^*. Then the control heater is switched on and the pumping rate, P and I parameters, and the time origin t_0 are set so that $T(t) \approx T^*$ and power output from the control heater is around 0.3 W. No rigorous procedure for determining these parameters was used, but once they are set the algorithm can keep the temperature stable for up to several days. If the system is left undisturbed, the temperature is stable to within 0.1 mK. It should be noted, however, that the cooling efficiency of pumping, for example, does depend on the volume of LHe available in the cryostat, so the stability, especially against perturbations, tends to decrease over time, since the remaining adjustable parameters are not set to their optimal values.

For temperature measurement, two resistive thermometers, measured by a four-wire method, are placed inside the bellows and in the bath. A third temperature measurement is provided by the saturated vapour pressure. As an input for the temperature control, the resistive thermometer immersed in bath is used, or,

[1] This is PID, or proportional-integral-derivative, control scheme with $D = 0$. Noise in the temperature measurement did not allow the use of the derivative term. Exponential smoothing of the temperature time-series was attempted, but this decreased the responsiveness of the system.

if very near the λ-transition, the pressure, since the resistive thermometer does not have a calibration in that temperature region.

1.2.2 Experimental and analysis protocol

The temperature of the system is stabilised at the chosen temperature with the aforementioned control system. With stable temperature, the amplitude of both in-phase (quadrature) and out-of-phase (dispersion; phase with the reference excitation signal) component of the signal at the excitation frequency (henceforth the response) of the second sound resonator is measured as a function of excitation frequency.

First, the resonant frequencies are identified by scanning the response, usually in the range from 500 Hz up to several kHz. For standard measurements, the first resonant frequency is used. The higher harmonic frequencies are useful for determining the inhomogeneous distribution of the vortex line density within the turbulent tangle (this will be addressed further in chapter 3). After the working frequency is chosen, the phase compensation of the lock-in amplifier is set so that the in-phase component of the response acquires a Lorenzian shape (compensating the phase acquired on the measurement circuit). The integration time constant of the lock-in amplifier is set to 100 ms for steady-state turbulence and 10 ms for decaying turbulence measurements.

The excitation sensor is connected to AC voltage with maximum amplitude such that the amplitude of the response at resonance is still linearly dependent on the amplitude of the excitation, see Fig. 1.4. This is usually in the range 5 - 10 V with response usually in the mV range. The meaning of this criterion is that the movement of the sensor membrane is not significantly affected by mechanical constraints and that it does not generate significant turbulence on its own.

The main task of the experiment consists of measuring the resonant response while changing the flow conditions, i.e., starting and stopping the flow and changing the mean flow velocity. Two methods are used to calculate L from the immediate experimental data, see fig. 1.5. In the first, a Lorenzian curve,

$$f(\omega;\omega_0,\tilde{A},\Delta,b) = b + \frac{2\tilde{A}}{\pi}\frac{\Delta}{(\omega-\omega_0)^2+\Delta^2}, \tag{1.10}$$

is fitted onto the obtained quadrature of the response to determine the parameters entering (1.8), with $A = 2\tilde{A}/\pi\Delta$ for every flow velocity, while the parameters Δ and A_0 that enter (1.8) are obtained from quiescent helium (ω here means the angular frequency of the second sound, not the magnitude of vorticity). The second approach uses the fact that only the amplitude of the resonance A is

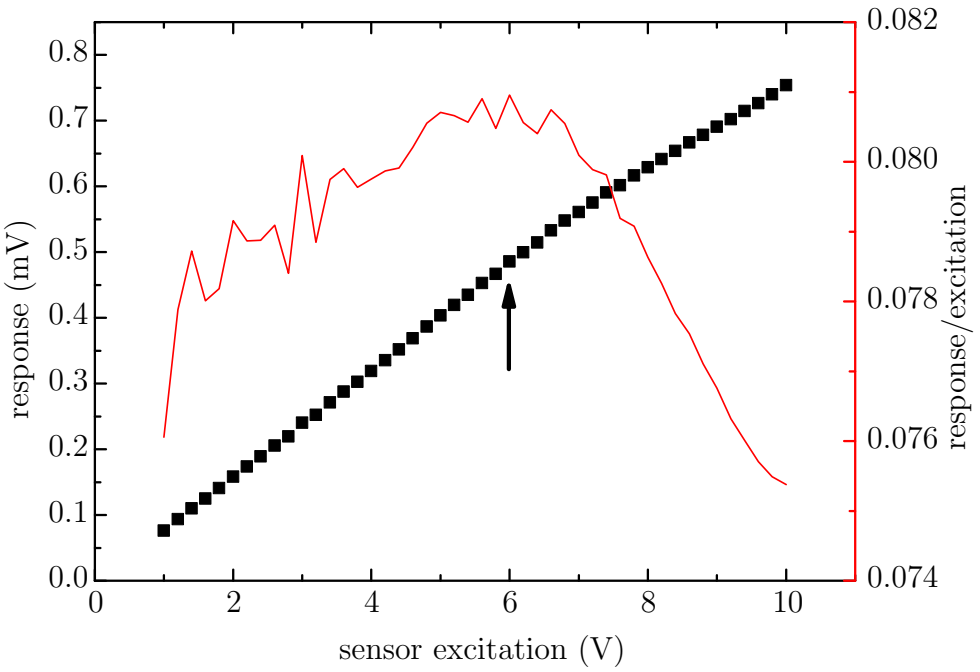

Figure 1.4: Amplitude of the response of the second sound detector as a function of the amplitude of the excitation. The right axis shows response linearly compensated by the drive. The used drive voltage (6 V) is indicated by the arrow.

required if Δ and A_0 are known. In this approach only the amplitude of the signal at the resonance is measured, that allows much faster data acquisition and construction of time dependence of the vortex line density $L(t)$.

The first approach is used primarily to check that the resonant frequency ω_0 is not changing due to changing flow velocities, what is taken as a requirement for any subsequent measurements, since to obtain $L(t)$ it is necessary to measure at the resonant frequency, and to characterise possible changes in the background b. The shifts in resonant frequency are due to temperature increasing locally inside the channel[2] (due to temperature-dependent second sound velocity), what in turn makes the temperature-sensitive material parameters of the superfluid helium, such as the mutual friction constant B, uncertain.

To study the turbulence in decay, $L(t)$ is measured in a process where the He-II is allowed to flow for 10 to 30 seconds after which the flow is suddenly (of the order of 10 ms) stopped. The sampling is irregular in time with average data acquisition rate of about 60 Hz. The reduced integration constant of the lock-in amplifier, 10 ms, causes increased noise in the data. To reduce it, each decay experiment is repeated up to 150 times with nominally identical conditions. The obtained $L(t)$ curves are then linearly interpolated onto a regular 100 Hz

[2]For example, as a result of dissipation of turbulent energy.

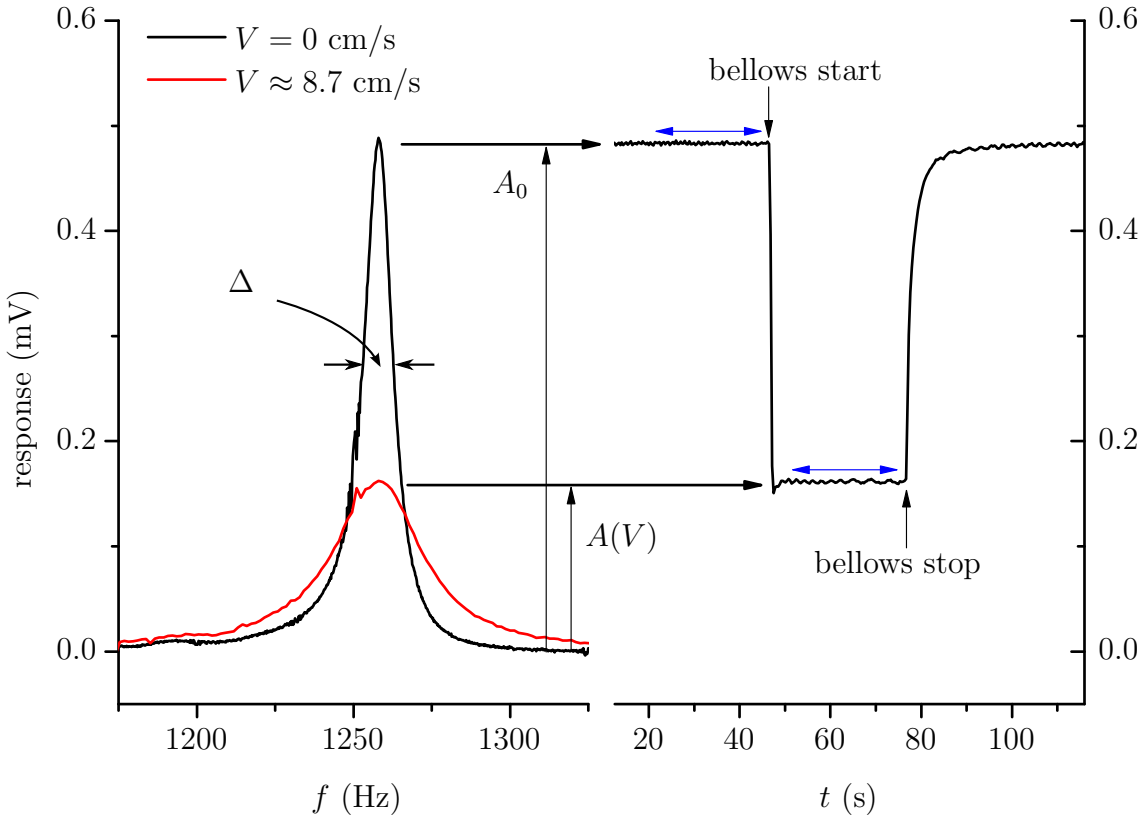

Figure 1.5: Obtaining L from the measured electrical signal. Figure on the left shows the meaning of the parameters in (1.8), and modification of the resonance curve with introduction of turbulence (the first approach in the text). Figure on the right shows the change in amplitude at resonance with introduction of quantum turbulence by switching on the flow (the second approach in the text). The parameters A and A_0 necessary for calculation of L are taken as averages over the indicated ranges before the flow starts and when the turbulence is fully developed. Parameter Δ is taken from a measurement of the full resonant curve for quiescent He-II as in approach 1. The legend shows mean flow velocity inside the channel.

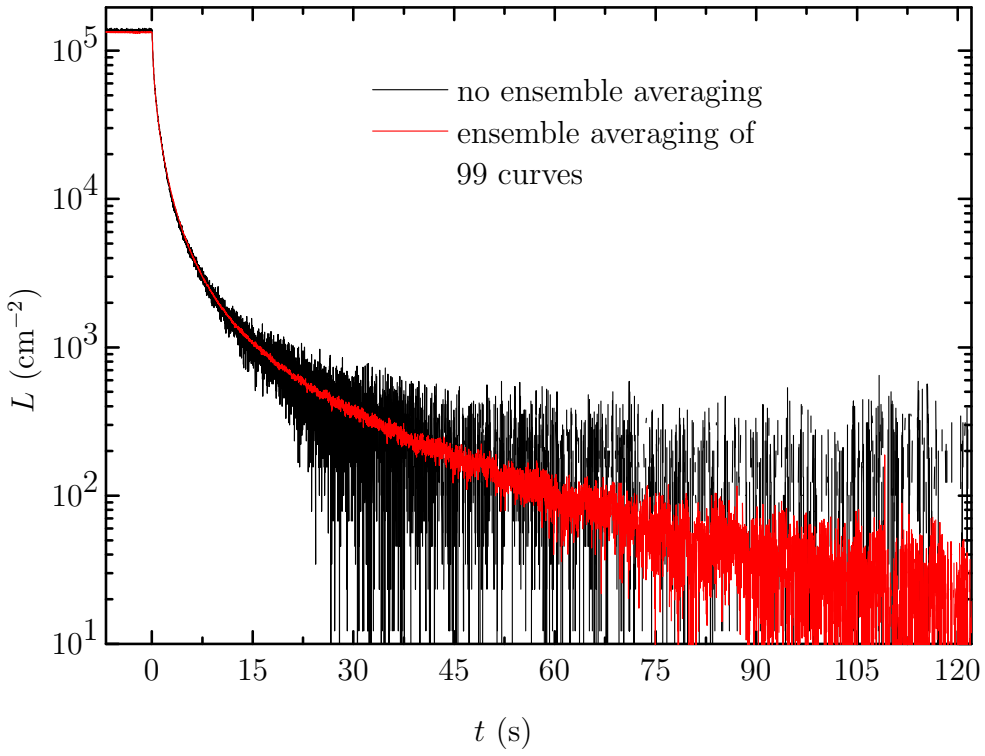

Figure 1.6: Typical reduction in noise after ensemble averaging. At least additional 30 s of well-characterised decay curve is gained. The steady state ends (squeezing of the bellows stops) at $t = 0$.

time-series and averaged point-wise. See Fig. 1.6 for an illustration of a typical reduction in noise.

2. Experimental results

Quantum turbulence was studied experimentally in both steady state and in decay. The experiments were performed in the range of temperatures spanning 1.17 – 2.16 K, or in terms of ratio of the normal fluid density to the total density of LHe, approximately 0.02 – 0.91. Turbulence was probed in the centre of the channel either 14 mm downstream from a grid placed behind the flow conditioner (labelled "grid" experiments) or with the grid removed (labelled "no grid" experiments) with only the flow conditioner upstream from the second sound sensors, see also Fig. 1.2. The flow conditioner was 55 mm upstream from the detection region. The grid was a regular square stainless steel mesh and the flow conditioner consisted of a stack of capillaries.

The flow conditioner can be, too, seen as a grid and the experiments could be regarded to be in the near or far wake of a grid. However, due to the relatively large distance of the detecting region, the flow produced by the conditioner is probably not a typical grid flow, but rather a mixture of grid and pipe flow, thus the labelling.

2.1 Steady state of turbulence

A part of the results in this section is submitted to Europhysics Letters. The latest draft at the time of writing is reproduced as Attachment 3. The main aim of the steady state experiments is the characterisation of $L = L(V)$ dependence of the vortex line density L upon some measure of the flow velocity V. In the experiments presented in this thesis, both normal and superfluid components of He-II are allowed to flow freely, with matching mean flow velocities, $\langle v_s \rangle = \langle v_n \rangle = V$ ($\langle \cdot \rangle$ denoting spatial averaging over the channel), so the flow velocity V is the mean flow of the LHe. This is in contrast with pure superflow [9], an experiment in which only the superfluid component is allowed to flow, where $\langle v_n \rangle = 0$ or thermal counterflow [10, 11], where the flow is activated by heat flux and $\langle v_n + v_s \rangle = 0$ with only $\langle v_n - v_s \rangle$ having a non-zero value.

The main steady state experimental result is in Fig. 2.1, showing both grid and no-grid experiments. The data exhibits a marked peak at $V \approx 2$ cm/s clearly visible in Fig. 2.1. The position of this peak is unchanged by variation of temperature, therefore its probable source is some mechanical resonance of the system, but its exact origin is unknown. Since the peak appears only for a very narrow range of velocities and does not seem to affect the $L(V)$ dependence

outside this range, it is removed in the subsequent analysis.

The pronounced "bends" at the ends of certain datasets in Fig. 2.1 are due to the resonance peak (see Fig. 1.5) being attenuated to the point of barely rising above the noise, what causes division by 0 in (1.8). Thus, as it's not a physical effect but rather an indication of the limit of the measurement technique, these features are, too, removed from the subsequent analysis.

Flows slower than a small, but finite, critical velocity V_c (of the order of 0.1 cm/s) do not produce detectable vortex line density. The dependence can be sufficiently accurately characterised by a simple power law

$$L(V) = L_r + A(V - V_c)^q, \tag{2.1}$$

where L_r is remnant vorticity of the order of 100 cm^{-2}, at least two orders of magnitude smaller than typical values of L for the fully-developed turbulence. The remnant vortex line density is an excess vortex line length relative to some earlier time (when the A_0 parameter of (1.8) was sampled) that remains constant even if the system is left undisturbed for up to several hours. The origin of this effect is most probably pinning of the vortices onto the channel walls. For the present purposes, it is merely a parasitic effect that reduces the sensitivity of the measurements in the limit of low flow velocities. The exponent q is approximately 1.5, as can be seen in the compensated plot in Fig. 2.2 and the plot of fitted exponents in Fig. 2.3. Similar experiments were reported in [12] where the exponents q varied between 0.9 – 1.3. However, it is possible that in these experiments the detection itself (through a pulsed heater instead of an oscillating membrane) generated additional turbulence which puts the results into question. Nevertheless, the present experiments extend the previous ones to a wider range of temperatures (in [12] restricted to only 1.5, 1.8 and 2.0 K) and velocities (the lower limit was pushed by an order of magnitude from approximately 1 cm/s to 0.1 cm/s).

It should be pointed out that non-linear least squares fitting of exponential functions of the form (2.1) is often problematic and the compensated figure is therefore a better indication of the scaling, however, the 1.5 exponent is still found, especially for the grid experiments in the temperature range 1.45 – 1.95 K.

The most striking feature of the obtained $L(V)$ curves is the lack of temperature dependence. This is in contrast with the thermal counterflow or pure superflow, see Fig. 2.4, experiments involving forced mean differences in the velocity of the fluid components of He-II. The superflow data in Fig. 2.4 (published

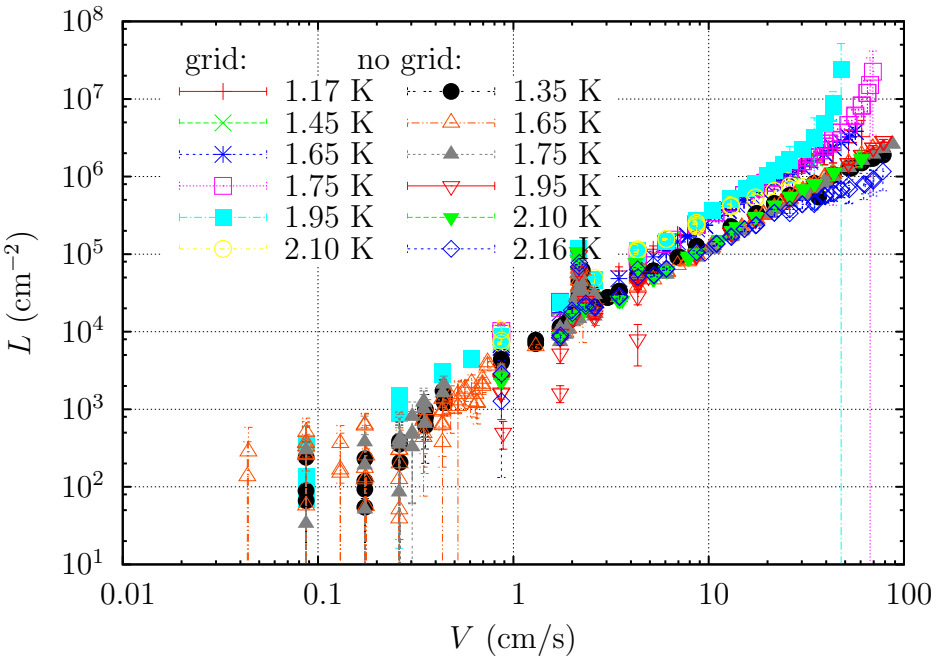

Figure 2.1: All available data on the dependence of the steady state vortex line density L on mean flow velocity V. The set of data corresponding to the experiments with additional grid exhibits approximately twice the vortex line density, as is clear above approximately $V = 3$ cm/s, where noise becomes less important, see also the compensated plot in Fig. 2.2. The "bends" at the ends of certain datasets and the peak at $V \approx 2$ cm/s are removed from subsequent analysis. The error bars are from (1.8) only.

in [9], reproduced here as Attachment 1)[1] were obtained in the same channel with the flow conditioner replaced by a *superleak*, a silver sinter "plug" that allows only the superfluid component of He-II to flow through. These experiments are usually understood in terms of the Vinen equation [14, 9],

$$\frac{\mathrm{d}\,L}{\mathrm{d}\,t} = \chi_1 \frac{\rho_n B}{2\rho} w L^{3/2} - \chi_2 \frac{\kappa}{2\pi} L^2, \tag{2.2}$$

where χ_1, χ_2 are temperature-dependent parameters, and $w = \langle v_n - v_s \rangle$ is the mean counterflow velocity. For the superflow in [9], the mean counterflow velocity is the same as the mean outflow from the bellows, $w = V$. In the steady state, $\mathrm{d}\,L/\mathrm{d}\,t \approx 0$, the equation predicts $L \propto w^2$ scaling with temperature-dependent prefactor. Possible connections between the Vinen equation and the present coflow measurements are discussed further in section 3.2.

[1] Pure superflow through silver sinter supearleaks was also the subjects of the author's Bachelor thesis [13] and a part of its result was published in [9]. Further details on these experiments can be found therein.

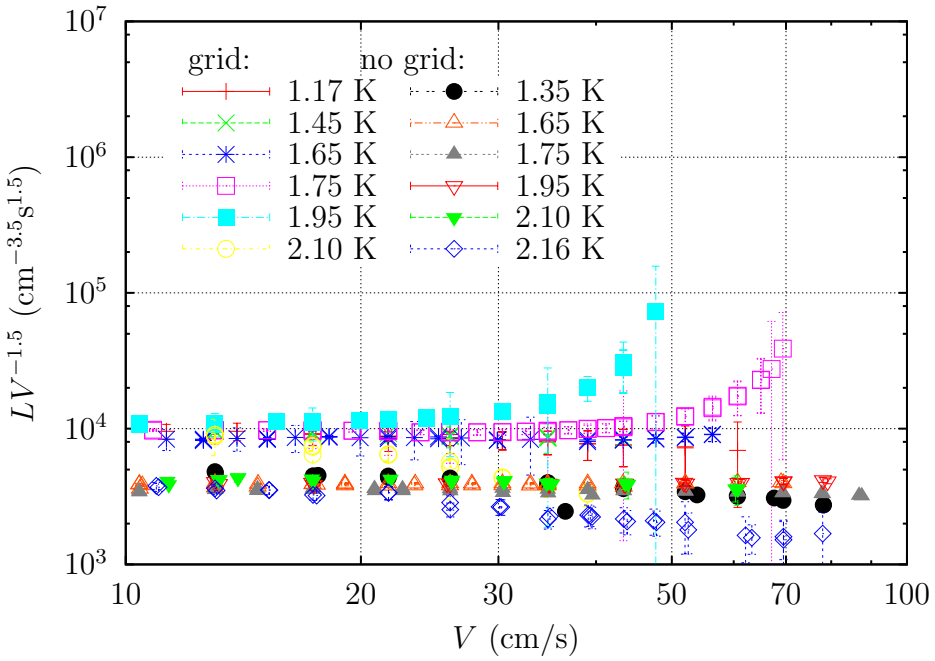

Figure 2.2: Compensated plots for scaling, same data as in Fig. 2.1.

The above results were measured at the first resonant frequency f_1 of the second sound resonator. Measuring at the second harmonic frequency $f_2 \approx 2f_1$, one arrives at significantly different vortex line density L, see Fig. 2.5.

During the measurements, a second sound standing wave is established in the channel. Such probing is, presumably, most sensitive in the regions of high amplitude of the second sound oscillations, which will be different for the first and the second resonant frequency. This hints at the possibility that the density of the vortex tangle is not homogeneous across the channel. Note that this violates the assumption of homogeneity of the vortex tangle that is behind (1.8), and puts into question the meaning of L obtained with this equation. The validity of equation (1.8) will be discussed and defended in the next chapter.

2.2 Decay of turbulence

The results in this section were published in the Journal of Low Temperature Physics [15] (attached as Attachment 2). The decay of turbulence is studied in the same conditions as the steady state case. The main aim, however, is the study of the time dependence of the vortex line density $L(t)$ after the forcing that generates and maintains the turbulence is suddenly switched off. In the experiments, the turbulence is first allowed to evolve in steady mean flow (the bellows being compressed at constant rate) for at least 10 seconds before the bellows is

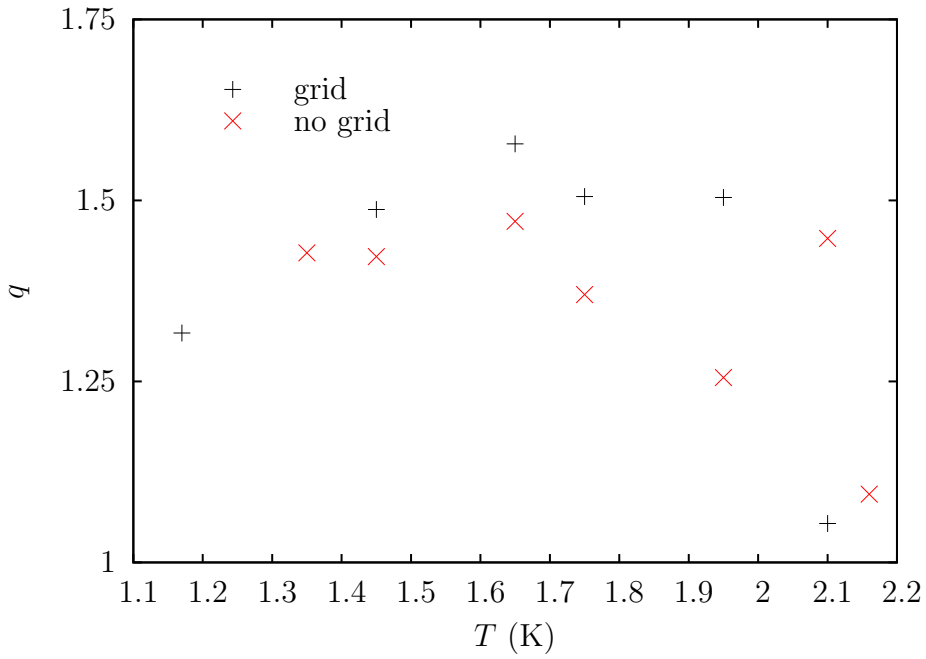

Figure 2.3: Exponents q from (2.1) corresponding to experiments with and without the additional grid. The mean values are (1.4 ± 0.2) with the additional grid and 1.35 ± 0.14 without it.

suddenly stopped (of order of 10 ms). The data in this section are mostly from the run with the additional grid, since at the time of the measurements with the flow conditioner alone, the ensemble averaging to reduce the noise in the signal was not yet possible. This set of data thus suffers from strong noise.

A typical set of data from one temperature, 1.45 K in this case, can be seen in Fig. 2.6. Characteristic of these decay processes is the $t^{-3/2}$ late time behaviour. Stalp, Skrbek and Donelly [1, 2] explained this behaviour, which was observed in a similar experiment [16], with a quasi-classical theory, see chapter 3 for further discussion. They find a time dependence of the form (time t is measured from the beginning of the decay, i.e., from the instant when the bellows stopped)

$$L(t) = b(t + t_0)^{-3/2} + L_r, \tag{2.3}$$

with t_0 usually called *virtual time origin* and b depending only on the channel size and possibly the temperature; L_r is the remnant vortex line density as in (2.1). The parameter b is connected with the concept of effective viscosity of He-II, which will be discussed further in chapter 3. This form of $L(t)$ suggests that, for a single temperature, one could obtain a collapse of individual decay curves in the late time by appropriate shifting of the time axis, regardless of the initial vortex line density $L_0 = L(t = 0)$.

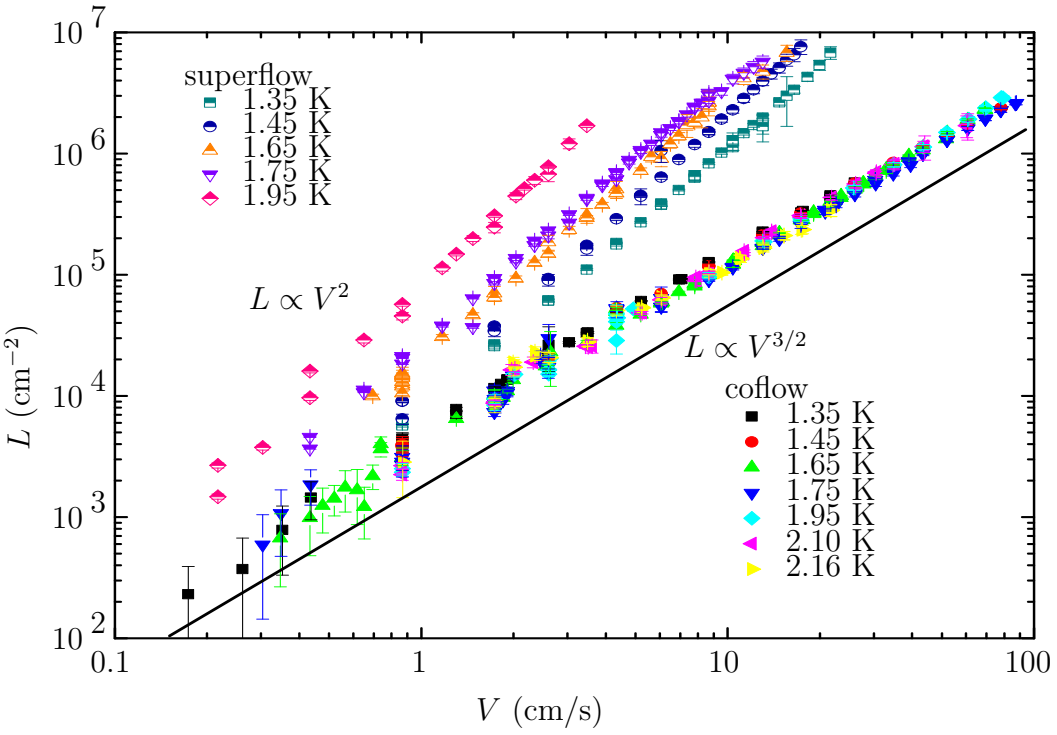

Figure 2.4: Comparison of the co-flow no-grid experiments and superflow [9] (reproduced in Attachment 1). In the superflow experiments, only the superfluid component is allowed to flow through the channel, contrary to the free flow of both components in the co-flow.

The late-time collapse of the $L(t)$ curves can be seen in Fig. 2.7. The values of t_0 were obtained by fitting and are plotted in Fig. 2.8.

A typical set of data for the decay without the grid can be seen in Fig. 2.9. The data is much more noisy, but the essential $t^{-3/2}$ behaviour in late time remains evident, except for the $L_0 = 10^6$ cm^{-2} case, which was probably affected by a temperature instability.

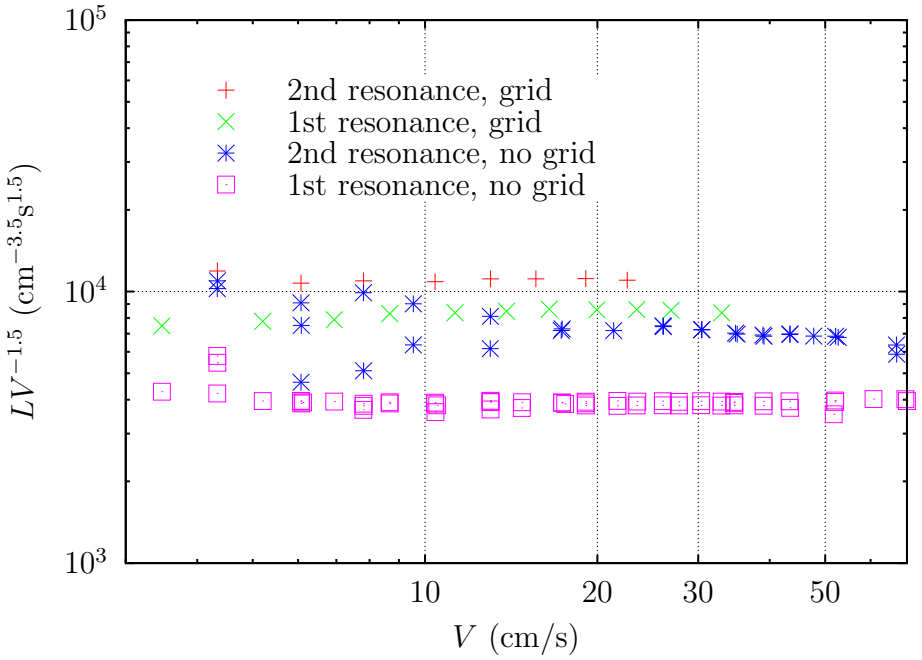

Figure 2.5: Vortex line density L deduced experimentally at first and second resonant frequency of the second sound resonator at 1.65 K. Figure shows the compensated quantity $LV^{-1.5}$ to accentuate the difference between the two resonances. Note that the relative difference is smaller for the grid data.

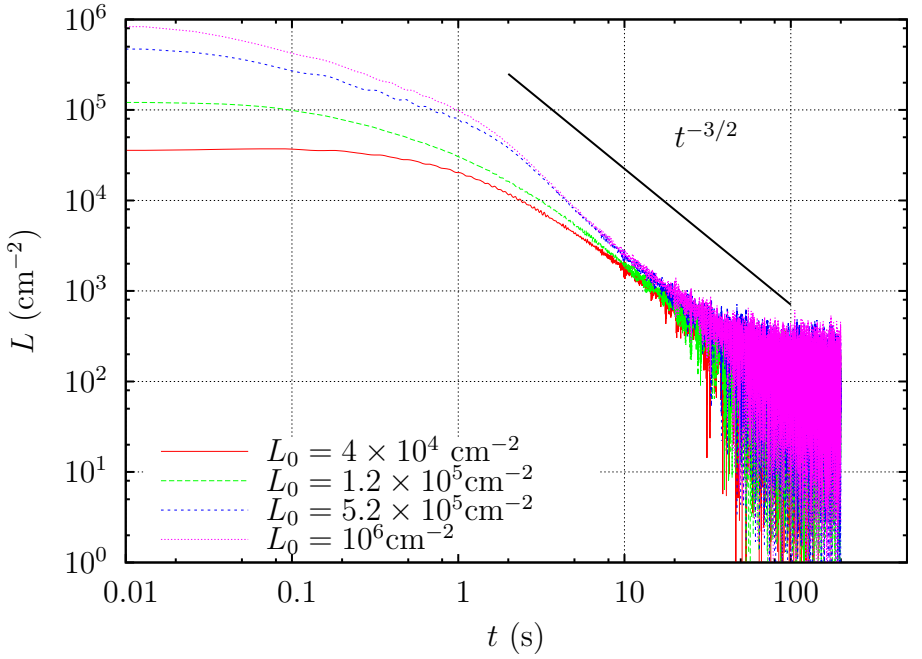

Figure 2.6: Decaying vortex line density $L(t)$ at 1.45 K, with 4 different initial vortex line densities. After a short transition time, all curves exhibit characteristic $t^{-3/2}$ behaviour.

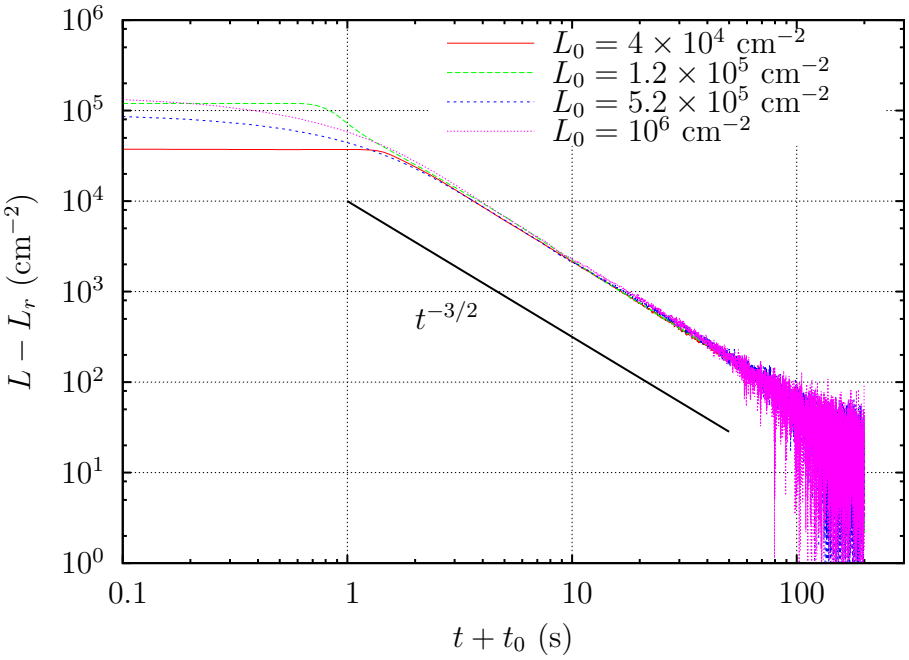

Figure 2.7: The collapse of individual decay curves regardless of the initial vortex line density. Same data as in Fig. 2.6.

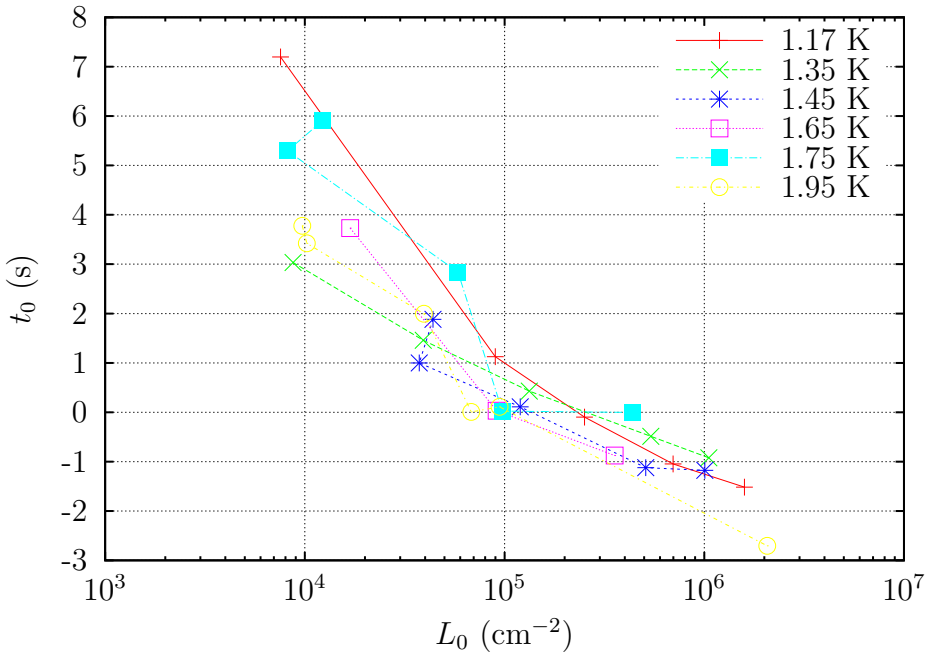

Figure 2.8: Virtual origin times t_0 of (2.3) for different temperatures as a function of initial vortex line density L_0.

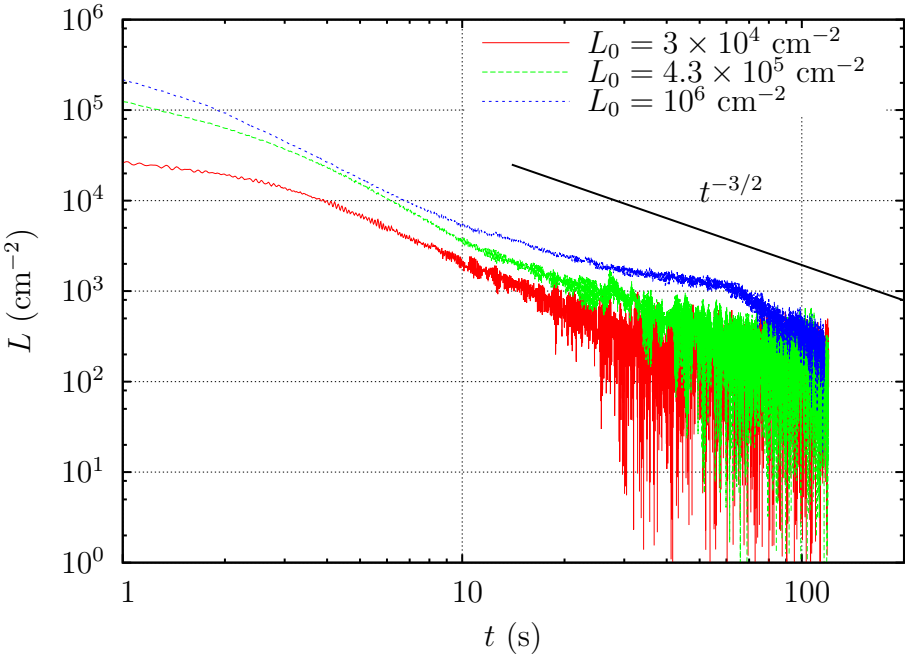

Figure 2.9: Decay without the grid. Even though the lack of ensemble averaging makes the signal much more noisy, the essential qualitative $t^{-3/2}$ late time behaviour is evident. The irregular behaviour of the $L_0 = 10^6$ cm^{-2} is probably caused by unstable temperature.

3. Discussion

3.1 Quasi-classical quantum turbulence and the effective kinematic viscosity

The work presented in this section forms a part of work published in Journal of Low Temperature Physics [15] (reproduced as Attachment 2) or submitted to Europhysics Letters (the latest draft at the time of writing reproduced as Attachment 3).

3.1.1 The decay of turbulence

Superfluid helium can be modelled in several different ways. Depending on the particular experiment, the two-fluid nature of He-II can be accentuated, as in thermal counterflow [10, 11] or superflow [9] experiments, or the flow arrangements can be of a more classical nature, such as pipe flows [17], or grid flows [16], where a more classical phenomenological picture of He-II is justified. The two-fluid description, of course, still remains valid, it is thus essential that for He-II to be described as a single fluid behaving essentially classically, the superfluid and normal components have to be locked together, behaving as one, at least on the relevant length scales.

This is the basis of the approach used by Smith, *et al.* [16], followed by Stalp, Skrbek and Donnelly [1, 2], who observed the decay of homogeneous and isotropic turbulence (*HIT* henceforth) generated by pulling a grid through stationary He-II. Detection was by a second sound attenuation. In these experiments the vortex line density (there interpreted as vorticity through $\omega = \kappa L$, which is disputable [18]) was observed to decay at late times as $t^{-3/2}$, much as in the currently presented results, with various transitional effects before the $t^{-3/2}$ decay sets in.

Stalp, Skrbek and Donnelly explained [1, 2] their observations (including the transitional effects) with a model that describes He-II as a single fluid with some *effective kinematic viscosity* $\nu_{\mathtt{eff}}$, i.e., the velocity fields of the two components are approximately equal except at very small scales (of order of the vortex line separation distance) where quantum mechanical constraints on the superfluid velocity field become important. Further they assume that the turbulence is classical in nature and is well described by the Richardson cascade and the Kolmogorov scaling laws (see, for example, chapter 6 in [19]), in particular, they assume that an

inertial subrange develops between the energy containing length scale[1] k_e^{-1} and the dissipation length scale k_η^{-1}, where viscosity becomes important, with the standard Kolmogorov form[2]

$$E(k) = C\epsilon^{2/3}k^{-5/3},\ k \in [k_e, k_\eta]\,, \tag{3.1}$$

where $C \approx 1.5$ is the 3D Kolmogorov constant, $\epsilon = -\,\mathrm{d}\,E/\,\mathrm{d}\,t$ is the dissipation rate (E being the *total* turbulent energy) and k is the wave number. Above the energy containing length scale k_e^{-1} the energy spectrum extends up to the channel size k_c^{-1} as $E(k) = Ak^m$, $k \in [k_c, k_e]$, with $m = 2$, with condition on A and k_e that $E(k)$ is continuous at k_e. For $k \notin [k_c, k_\eta]$ $E(k) = 0$, since it is impossible for the energy to exist on scales larger than the system itself and the truncation at high wave-numbers models the viscous dissipation. Such spectrum then decays in time, with energy containing length scale $k_e(t)$ increasing until it saturates at the system size k_c. It is assumed that the inertial subrange remains of the Kolmogorov form throughout the entire decay.

To connect the energy decay with the decay of the vortex line density, Stalp, Skrbek and Donnelly assume that the energy dissipation takes the form

$$\epsilon = \nu_{\mathtt{eff}}\kappa^2 L^2. \tag{3.2}$$

This form of energy dissipation is motivated by classical turbulence, where for HIT $\epsilon = \nu\langle\omega^2\rangle$ [20] where ω is the RMS of the turbulent vorticity fluctuations and $\langle\cdot\rangle$ denotes spatial averaging. However, as Vinen points out [18], due to the singular nature of quantised vortices, $\langle\boldsymbol{\omega}_s^2\rangle = \langle(\mathrm{curl}\,\boldsymbol{v}_s)^2\rangle$ is infinite ($\boldsymbol{v}_s$ and $\boldsymbol{\omega}_s$ being the superfluid velocity and vorticity). Classical analogies to (3.2) should therefore be regarded as only a motivation and (3.2) should be seen as an independent hypothesis.

The above assumptions are enough to derive the expression for the decaying vortex line density [1],

$$L(t) = \frac{D(3C)^{3/2}}{2\pi\kappa\sqrt{\nu_{\mathtt{eff}}}}(t + t_0)^{-3/2}, \tag{3.3}$$

where D is the channel size. This allows for determination of the effective kinematic viscosity from the experimental data. The kinematic viscosity as a function of temperature, as determined from the decay measurements, is shown in Fig. 3.1 in the next subsection, along with the original data from [1]. The values $\nu_{\mathtt{eff}}$ approximately agree, even though the two experiments are quite different: in the

[1] More precisely, the length scale is $(2\pi k)^{-1}$. The exact value of the scale is unimportant in the following discussion therefore the constant prefactor $(2\pi)^{-1}$ is omitted.

[2] Intermittency effects are also discussed in [2].

present experiments, the decay of turbulence is measured at a fixed downstream position from the grid from an initial state of fully developed turbulence that lasted at least 10 seconds, whereas in the towed grid experiments the relative position of the grid and sensor is initially changing with the final sensor-grid distance much greater than in the present experiments. Another important difference is the mean flow relative to the walls during the steady state in the current measurements, that opens the possibility that the studied turbulence is a mixture of channel and grid turbulence, instead of a pure grid turbulence as in the Oregon experiments.

Despite these differences, the values of kinematic viscosities approximately agree.

3.1.2 The steady state of turbulence

Equation (3.2) can also be utilised for interpreting the steady state experimental results. Defining the superfluid Reynolds number Re_κ as

$$\mathrm{Re}_\kappa = \frac{vH}{\kappa} = \frac{\epsilon^{1/3} H^{4/3}}{\kappa}, \tag{3.4}$$

where v is the root-mean-square (RMS) of velocity fluctuations and $H \equiv v^3/\epsilon$. The basis of the quasi-classical interpretation of the experiments is that the He-II behaves as a single fluid as described above, thus v describes fluctuations of both superfluid and normal fluid velocity. The scale H characterises the large scale (the size of the large eddies) of the turbulence [19].

Using this definition, equation (3.2) can be rewritten,

$$\frac{\delta}{H} = \frac{\nu_{\mathtt{eff}}}{\kappa} \mathrm{Re}_\kappa^{-3/4}, \tag{3.5}$$

where $\delta = L^{-1/2}$ is the vortex line separation. This scaling was also observed in [17] for a limited temperature range and predicted from numerical simulations [21]. Notice that the inter-vortex distance, a length scale where quasi-classical theories must break down because quantisation of circulation becomes important, scales exactly as the Kolmogorov dissipation length scale η, where viscosity starts to dominate over inertial effects in classical turbulence [19],

$$\frac{\eta}{H} = \mathrm{Re}^{-3/4} = \left(\frac{vH}{\nu} \right)^{-3/4}. \tag{3.6}$$

Quantities H and v are unknown in the present experiments, however if the RMS of velocity fluctuations is proportional to the mean flow velocity, $v \propto V$,

equation (3.5) is equivalent $L \propto V^{3/2}$ and thus allows for extraction of $\nu_{\mathtt{eff}}$ from the steady state, if H and v can be determined.

It was not possible to measure these quantities in the present experiments so an estimation must be attempted. The characteristic large scale H can be estimated as a typical length scale of the experiment. For the grid experiments, it is taken to be the grid constant, 0.6 mm. For the experiments with the flow conditioner alone, H just behind the flow conditioner would be typical size of the capillaries it consists of, i.e, 1 mm. However, due to the contraction in the channel cross-section immediately after the flow conditioner (see Fig. 1.2) the typical length scale is expected to contract as well and is estimated at 0.5 mm, neglecting any possible growth of the large structures downstream, see [22].

The RMS of velocity fluctuations v is assumed to be proportional to the mean flow velocity V through the intensity of turbulence τ, $v = \tau V$, as is common practice for classical turbulence. The turbulence intensity is in this case an adjustable parameter. The typical turbulence intensity in classical turbulence for grid and channel flows is of the order of 10%, so the chosen τ should be comparable. An additional condition imposed on the choice of τ is that the dependencies of δ/H on Re_κ collapse onto the same curve for both grid and grid-less experiments. This leads to the choice of $\tau = 9\%$ for flow with the grid and $\tau = 5\%$ for flow without the grid. The obtained collapse of 14 individual data sets is shown in Fig. 3.2. The motivation behind trying to collapse the data is that $\nu_{\mathtt{eff}}$ should be a well-defined material parameter of He-II and thus it should not depend on flow conditions. This may seem as circular reasoning, however, it is not a priory certain that such collapse is possible, or that it is possible for "reasonable" values of τ. This type of analysis shows that a unique $\nu_{\mathtt{eff}}$ is in principle possible and is the only available approach to its determination in the face of currently lacking independent measurements of τ and H.

Even though these choices of τ and H are based on reasonable approximations and analogies with classical turbulence, they should still be regarded as an adjustable parameters of the theory at this point. Therefore, an experiment measuring these quantities directly is highly desirable.

With a given τ and H, the effective kinematic viscosity can be deduced from the measurements via (3.5). This is possibly the first time the effective viscosity was extracted from the steady state of turbulence. The obtained values are in Fig. 3.1. The error bars indicated in the figure are only the errors due to fitting the relation (3.5) and are representative of the uncertainties of the relative position of the points. The absolute value of steady-state $\nu_{\mathtt{eff}}$ is influenced by

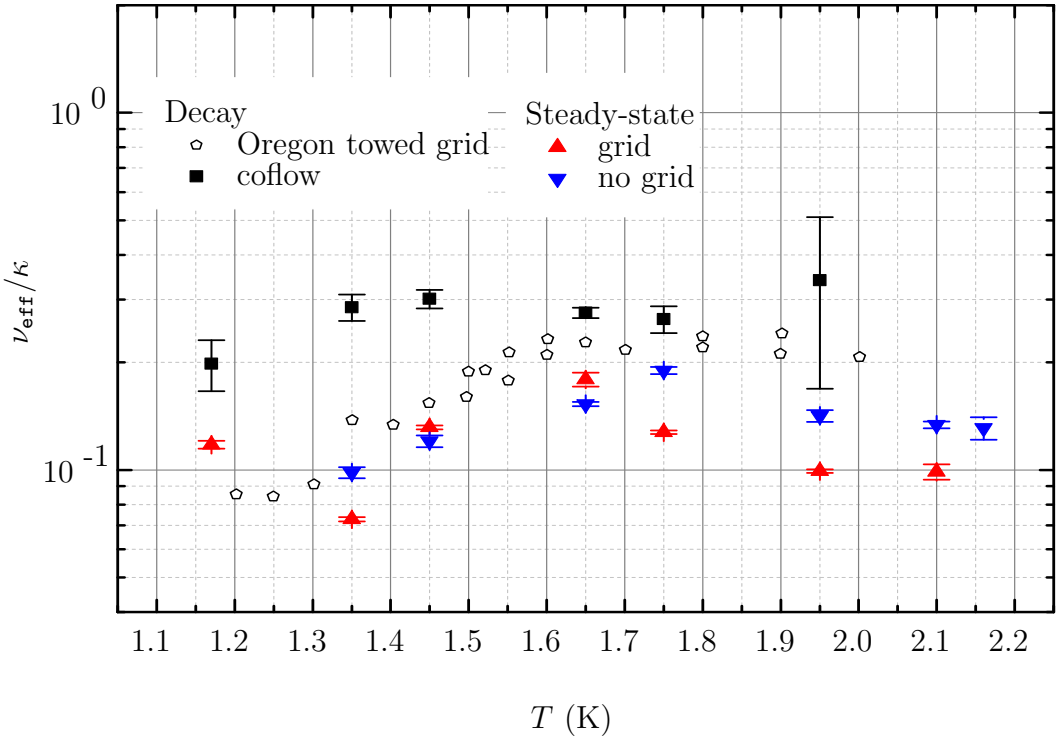

Figure 3.1: The effective kinematic viscosity of He-II in units of quantum of circulation κ from both decay experiments (published in [15], reproduced in Attachment 2), and the steady state (submitted to Europhysics Letters, latest draft at the time of writing reproduced in Attachment 3). Included for comparison are also Oregon towed grid data [1] which provide $\nu_{\mathtt{eff}}$ in a similar temperature range.

the uncertainties of H, τ and the vortex line density itself. Assuming that the uncertainty on H and τ can be as large as a factor of 2, the uncertainty on $\nu_{\mathtt{eff}}$can be up to factor of 8.

Notwithstanding these difficulties, the effective kinematic viscosities determined by three significantly different experiments approximately agree, which signalises that the concept of the effective viscosity for decaying superfluid turbulence is a valid and general description of dissipative mechanism for a class of quasi-classical quantum turbulence experiments.

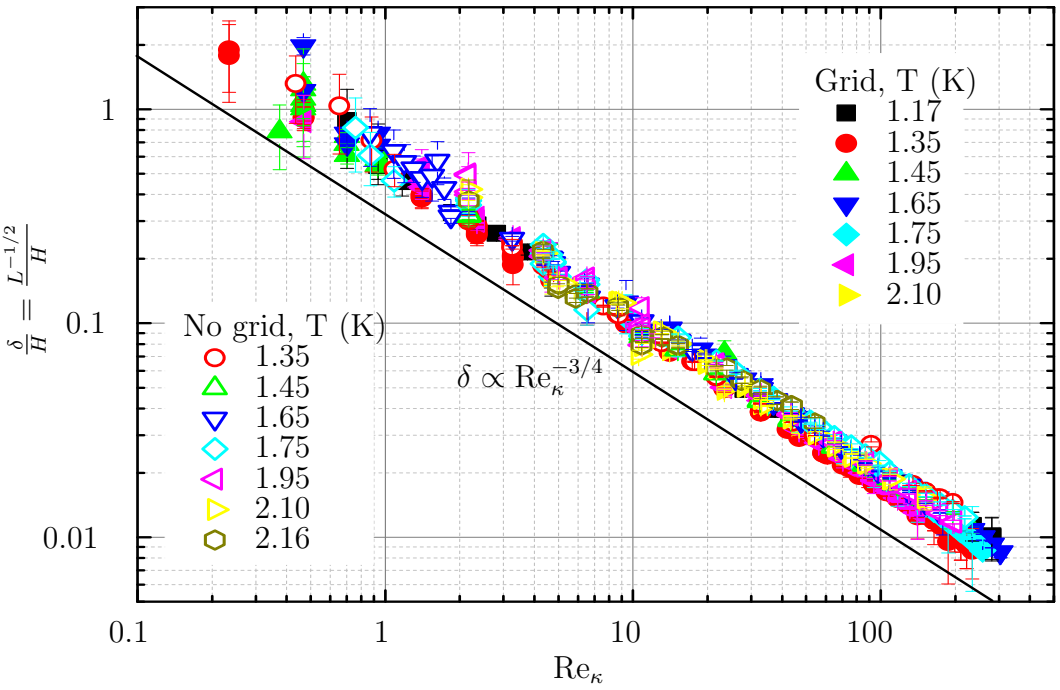

Figure 3.2: Inter-vortex distance δ normalised by the large scale of the turbulence H as a function of the superfluid Reynolds number $\mathrm{Re}_\kappa = \tau V H/\kappa$. Appropriate choices of τ and H allow for the 14 datasets to collapse onto a single curve.

3.2 Approaches to $L \propto V^{3/2}$ based on the counterflow theory

Prior to above model for the steady state was developed, different possibilities for explaining the $V^{3/2}$ scaling were attempted. Historically, the probably most explored setup of the quantum turbulence was the counterflow, where the mean velocities of the two components are forced to be different. Vinen [14] derived an equation that describes the dynamics of the vortex line density, that today bears his name,

$$\frac{\mathrm{d}\,L}{\mathrm{d}\,t} = \chi_1 \frac{\rho_n B}{2\rho} w L^{3/2} - \chi_2 \frac{\kappa}{2\pi} L^2, \tag{3.7}$$

where w is the mean counterflow velocity, B is the mutual friction constant and χ_1, χ_2 are temperature-dependent parameters. The equation is derived partly by dimensional analysis and by considering that the mutual friction, which is linearly proportional to w, see (1.6), causes linear (in time) growth of favourably oriented vortex line loops, that gives the first, positive, term linear in w. The second term is meant to capture the influence of vortex reconnections that decrease the total vortex line length.

This equation predicts, for constant w and arbitrary small initial $L(t=0) > 0$,

that $\lim_{t\to\infty} L(t) = L_\infty$ and $L_\infty \propto w^2$ (as can be seen by putting $\mathrm{d}\,L/\,\mathrm{d}\,t = 0$ in (3.7)). In practice, the steady state is achieved in order of 1 second, depending on w. Note that an enclosed He-II sample will typically contain certain number of vortex lines due to pinning on the walls. Thus the case $L(t = 0) = 0$ is practically impossible to achieve experimentally[3]. In the following the ∞ index will be dropped and L will always mean the limiting steady state.

The reasoning behind the individual terms in the Vinen equation (3.7) is in some sense "mesoscopic", as it refers to individual vortex lines and not necessarily to the global mean properties of the flow. Since the Vinen equation represents the only theory of its kind currently available, an attempt was made to understand the $L \propto V^{3/2}$ scaling with the same mesoscopic picture in mind. The following two subsections describe two such approaches as an alternatives to the above discussed quasi-classical picture.

3.2.1 Differing velocity profiles of the fluid components

The first attempt at explaining the scaling of L with mean flow velocity was to assume that Vinen's equation holds for this kind of flow and that the necessary counterflow velocity arises due to differences in velocity profiles of normal and superfluid component inside the channel (for example, normal fluid having profile resembling the parabolic one of Poiseuille flow and superfluid having a flat profile, since no-slip boundary condition does not apply to it).

Let S denote the cross-section of the channel and v_s and v_n the stream-wise cartesian components of the velocities of the He-II fluid components. The v_s and v_n are now functions defined on S. The mean counterflow velocity is

$$\bar{w} = \frac{1}{S}\int_S |v_n(\boldsymbol{x}) - v_s(\boldsymbol{x})|\,\mathrm{d}^2\,x. \tag{3.8}$$

The mass flow of each component through the channel is

$$Q_i = \rho_i \int_S v_i(\boldsymbol{x})\,\mathrm{d}^2\,x = \rho_i \bar{v}_i S, \quad i = n, s, \tag{3.9}$$

where $\bar{v}_i$ is the mean flow of the component through the channel.

The total mass flow $Q_s + Q_n$ must be equal to the outflow of the helium from the bellows, $Q = \rho S V$ where V is mean flow velocity inside the channel. Next, since the flow of both components is constrained equally, i.e., no superleaks are used, it is reasonable expect to that individual densities of components should

[3] In the original publication [14] this case is addressed by adding a weak L-independent growth function to the right hand side of (3.7).

not change inside the bellows (i.e., temperature does not change) so the outflows of both components should be in proportion to their densities, that is

$$\frac{Q_s}{\rho_s} = \frac{Q_n}{\rho_n} \implies \bar{v}_s = \bar{v}_n = V. \tag{3.10}$$

The mean counterflow velocity then becomes

$$\bar{w} = V \frac{1}{S} \int_S \left| \frac{v_n(\boldsymbol{x})}{\bar{v}_n} - \frac{v_s(\boldsymbol{x})}{\bar{v}_s} \right| \mathrm{d}^2 x \equiv V f(V), \tag{3.11}$$

where it is assumed that the integral f characterising the differences in the profiles is a function of V (i.e., the shape of the profiles changes as a function of the Reynolds number). The Vinen equation predicts $L \propto \bar{w}^2$, so in order to explain the $V^{3/2}$ scaling, the profile $f(V)$ would have to scale as $V^{-1/4}$. However, the constant profiles (parabolic for v_n and flat for v_s) as alluded to in the beginning of the subsection imply $f(V) = \text{const.}$, so the observed scaling cannot be explained with this simple example.

Strictly speaking, the boundary conditions of the normal and superfluid components of He-II on solid walls and the velocity profiles in pipe flows are not known, so $f(V) \propto V^{-1/4}$ is in principle possible. Obviously, the integral in (3.11) cannot be infinite, thus the required scaling can hold only for sufficiently large V. It is probably reasonable to assume that $V^{-1/4}$ scaling sets in gradually. However, the experiments show unchanged $L(V)$ dependence practically immediately after emergence above the noise. While this does not rule out this approach entirely, it makes it rather unlikely.

3.2.2 Fluctuating counterflow velocity

The second attempt assumes that the mechanism of generating vortex line length is the same as behind Vinen's equation, but the origin of the relative motion of the He-II components are random, and on small scales independent, fluctuations of both velocity fields. The main assumption is that Vinen's equation holds if the mean counterflow w is replaced by the RMS of the counterflow fluctuations w'. The steady state vortex line density is then

$$L = \gamma w'^2, \tag{3.12}$$

where w'^2 is the mean-square of the *counterflow velocity fluctuations* induced due to turbulence and γ is made up of the remaining constants in Vinen's equation. The scaling of w'^2 is estimated from dimensional analysis: dimension of w'^2 is $[L^2T^{-2}]$ (L is length, T is time) and we take that it can depend only on the

vortex line density L, dimension $[L^{-2}]$, and on energy input, i.e., how much the helium is stirred, ε, dimension $[L^2T^{-3}]$. The only possibility in this case is

$$w'^2 \propto \varepsilon^{2/3} L^{-1/3}. \tag{3.13}$$

Now we use the classical formula $\varepsilon \propto v^3/H$, which gives

$$w'^2 \propto \frac{v^2}{H^{2/3}} L^{-1/3}, \tag{3.14}$$

where H is the scale of large eddies and v is the RMS of velocity fluctuations as in the first section of this chapter. Substituting back to (3.12)

$$L \propto v^2 L^{-1/3}, \tag{3.15}$$

that is,

$$L \propto v^{3/2}. \tag{3.16}$$

The difficulty with this result is, again, that v is not the mean flow velocity and the constant turbulence intensity $v = \tau V$ needs to be assumed as in the first section of this chapter. In addition, this approach again assumes locking of the velocity fields at relevant length scales through the use of v, so the set of assumptions stays essentially the same as with the quasi-classical approach.

A particularly strange feature is that the randomly fluctuating drive of the creation of vortex length, given by (3.13), is decreasing with the strength of the present turbulence and, since we start from Vinen's equation, these results should also be temperature dependent. One could speculate that the factor of proportionality in (3.13) or (3.14) is also temperature dependent and that the dependence "cancels out" in the final equation. Unfortunately there is no clear way how to estimate how likely this could be.

3.3 Inhomogeneity of the vortex tangle and the second sound measurements

The experimentally observed second sound attenuation, and the corresponding vortex line density, is sensitive to which resonant frequency of the second sound resonator is used, while the derivation of (1.8) (see the Appendix to [9] and Appendix A of the thesis), based on the assumption of homogeneous distribution of the vortex line density, predicts that the measured L is independent of the order of the resonance frequency, which suggests that the vortices in the present experiment are distributed inhomogeneously across the channel.

To address this, a one dimensional mathematical model of the experimental technique is constructed that takes into account the second sound resonance explicitly. In the following, d denotes the channel width, the channel walls are placed at $x = 0$ and $x = d$, the excitation sensor is mounted on the $x = 0$ wall, and the detection sensor on the $x = d$ wall. Thus, the goal is to determine $w(d, \omega) = v_n(d, \omega) - v_s(d, \omega)$, where ω is the angular frequency of the second sound excitation[4].

We start by adding a localised harmonic forcing on the normal fluid[5] in (1.5), representing the idealised infinitely thin excitation sensor

$$F_e(x, t; \omega) = \rho_n E e^{i\omega t} \delta(x), \tag{3.17}$$

where E is amplitude of the excitation.

In order to describe the resonance, the reflective walls at $x = 0$ and $x = d$ need to be taken into account. This is achieved by expanding the domain to $(-\infty, \infty)$ and including reflected virtual forcing created by the walls, i.e., forcing at $x = 0$ is reflected by the wall at $x = d$ to $2d$ with negative sign, which in turn is reflected by the wall at 0 to $-2d$ with the original sign, etc., see Fig. 3.3. If the reflections were perfect, the velocity of the fluid at $x = d$ would be identically zero, therefore the factors of the δ-function in individual terms are assumed to be getting geometrically weaker with the number of the reflection with quotient $0 < p < 1$, thus the force on the superfluid due to the second sound excitation is

$$F_e(x, \omega) = \rho_n E e^{i\omega t} \left[\delta(x) + \sum_{n=1}^{\infty} p^n \left(-\delta(x - 2nd) + p\delta(x + 2nd) \right) \right]. \tag{3.18}$$

Using the mutual-friction-coupled two-fluid equations of motion, equations of continuity for mass of both fluid components and for entropy density, and the forcing (3.18) one arrives at (see Appendix A)

$$\begin{aligned} \frac{\partial^2 w}{\partial x^2} + \frac{\omega^2}{c_2^2} w - i\omega \frac{B\kappa L(x)}{3c^2} w - i\alpha_0 w = \\ - i\omega \frac{E}{c_2^2} \left[\delta(x) + \sum_{n=1}^{\infty} p^n \left(-\delta(x - 2nd) + p\delta(x + 2nd) \right) \right], \end{aligned} \tag{3.19}$$

where c_2 is the second sound velocity and B is the mutual friction constant and α_0 is intrinsic attenuation constant present regardless of any vortices being present.

[4]The Fourier component corresponding to the same frequency as the forcing is what corresponds to the measurement with lock-in amplifier synchronised to the excitation frequency.

[5]Movement of the superfluid component due to this forcing is induced only by the equation of continuity, as was explained in subsection 1.2.1.

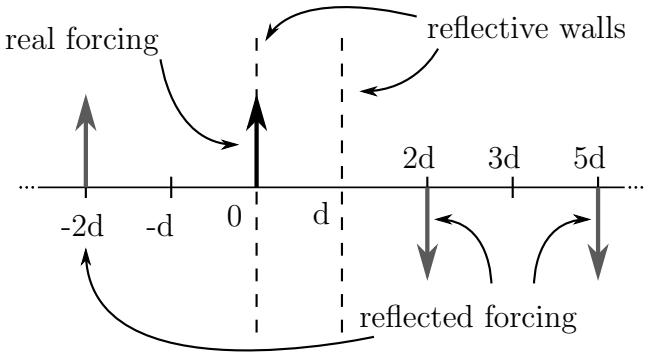

Figure 3.3: The replacement of the reflective walls by virtual forcing used in (3.19). To model imperfect reflection on the walls, the reflected forcing gets geometrically weaker with the number of reflections with coefficient $0 < p < 1$.

Any solution to (3.19) for $x \in (0, 2d)$, i.e., where $F_e \equiv 0$, can be written in the form[6]

$$w|_{x\in(0,2d)}(x) = aU(x) + bG(x), \tag{3.20}$$

where (prime denotes differentiation with respect to x) $U(0) = 1, U'(0) = 0$ and $G(0) = 0, G'(0) = 1$, i.e., $w(0) = a$ and $w'(0) = b$ and U and G being themselves solutions to (3.19) in $(0, 2d)$ with appropriate boundary conditions at $x = 0$. The solution $w(x)$ can be written in the form (3.20) for every interval $(2nd, 2(n+1)d)$, where n is an arbitrary integer, with differing a and b and with U and G being only appropriately shifted, that is, we look for solution to (3.19) on $(-\infty, \infty)$ in the form

$$\forall n : w|_{x\in(2nd,2(n+1)d)}(x) \equiv w_n(x) = a_n U(x - 2nd) + b_n G(x - 2nd). \tag{3.21}$$

The presence of the δ-functions on the right hand side of (3.19) imposes certain conditions at $x = 2nd$, in particular, continuity

$$w_n(2nd) - w_{n-1}(2nd) = a_n - a_{n-1}U(2d) - b_{n-1}G(2d) = 0, \tag{3.22}$$

and a given jump in the first derivative

$$\begin{aligned} w'_n(2nd) - w'_{n-1}(2nd) &= b_n - a_{n-1}U'(2d) - b_{n-1}G'(2d) \\ &= \begin{cases} Dp^{2n-1} & \text{for } n > 0 \\ D & \text{for } n = 0 \\ -Dp^{2|n|} & \text{for } n < 0 \end{cases}, \end{aligned} \tag{3.23}$$

where $D = -i\omega E/c_2^2$.

[6]The use of functions U and G is useful for numerical integration used later in this section.

The infinite set of equations (3.22) and (3.23) determine a_n and b_n if two additional boundary conditions, which can be chosen at will, are known. Thus, the $w(x)$, and in particular $w(d)$ is determined.

Inverting this derivation to obtain some approximation of $L(x)$ from the measured attenuation would be mathematically difficult and of limited utility, since usually only first two, at most three (not shown in the thesis), resonances have been measured, thus only limited information on the variation of the attenuation with frequency is known. Therefore, a different approach is chosen. For known, prescribed $L(x)$ resonance curves are calculated and subjected to the same analysis as the experimental ones, in particular, vortex line density is extracted via (1.8). Subsequently the influence of known inhomogeneity on the attenuation is studied.

Admittedly, this approach is not perfect. For example, the reflectivity p is impossible to determine a posteriori from the available data and must be chosen arbitrarily. This is certainly a flaw, but this sort of calculation, if not anything else, could place some estimation on the error of L obtained by (1.8) for inhomogeneous vortex tangles. The choice in the parameters is $p = 0.75$ and $\alpha_0 = 0.1$ cm^{-2}. Formula (1.8) depends only on the ratios of the velocities, therefore the amplitude of the forcing E is unimportant and can be set to 1.

In order to continue the analysis, some parametrisation of $L(x)$ must be chosen. $L(x)$ is, by construction, periodic with period d, so it is reasonable to represent it as first few terms of a Fourier series. In order to preserve the symmetry at $x = d$, only cosine terms are considered, hence

$$L(x) = \sum_{n=0}^{M} L_n \cos\left(2\pi \frac{x}{d}\right), \tag{3.24}$$

where $M \geq 0$ is some integer and L_n are the Fourier components of $L(x)$. In the following the $\boldsymbol{L} = (L_0, L_1, ..., L_M)$ notation will be used.

Material parameters $B = 1.144$ and $c_2 = 2037$ cm/s of LHe are taken at 1.65 K from [23]. The channel width d is set to 1 cm. From a chosen $\boldsymbol{L}$, $w(d, \omega)$ is calculated numerically using a program written in GNU Octave[7]. The program takes into account 7 reflections and closes the set of equations (3.22), (3.23) by assuming periodic boundary conditions.

Resonances were calculated at 1st, 2nd and 3rd resonant frequency for the following $\boldsymbol{L}$s (in cm^{-2}): 0, 10^4, $(10^4, 10^4)$, $\left(10^4, \frac{1}{2}10^3, \frac{1}{2}10^3\right)$, $(10^4, 0, 10^4)$, $\left(10^4, \frac{1}{3}10^4, \frac{1}{3}10^4, \frac{1}{3}10^4\right)$ and $(10^4, 0, 0, 10^4)$.

[7]Interested reader may find the complete program on the CD enclosed with the thesis.

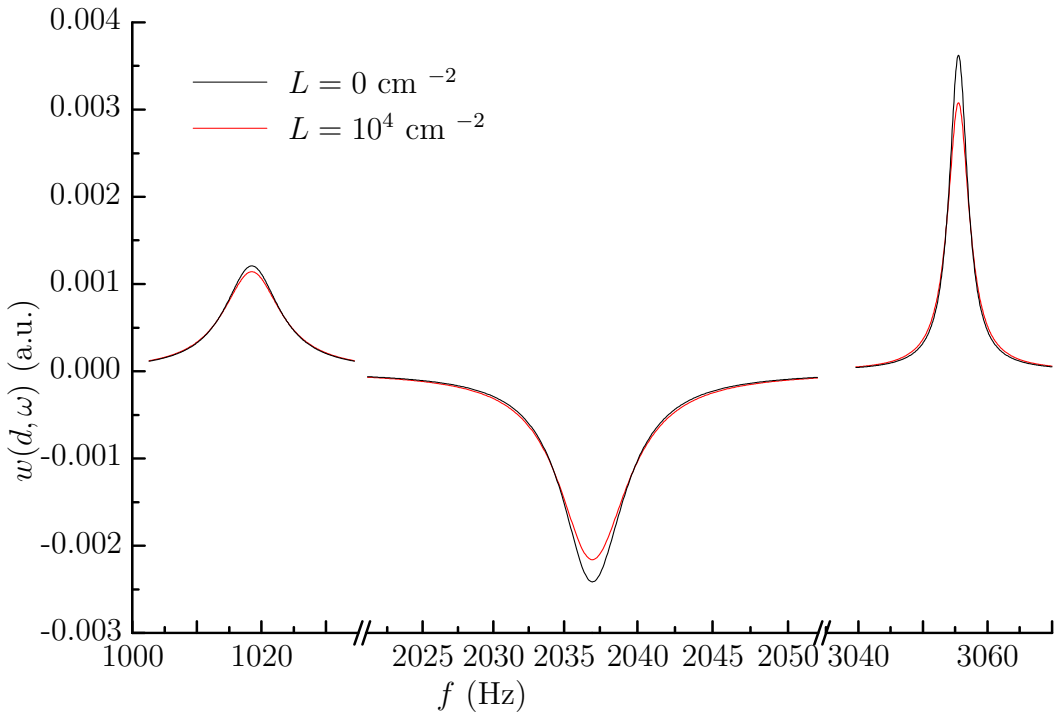

Figure 3.4: Real part of $w(d,\omega)$ as a function of ω for first 3 resonances. The sign flip for the second resonance is observed in the experiments. In these figures $L(x) = L_0$ is a constant of either 0 (taller black curves) or 10^4 cm^{-2} (shorter red curves). Note the two breaks in the x-axis.

The in-phase component (i.e, the real part) of $w(d,\omega)$ for homogeneous $L(x)$ is shown in Fig. 3.4. The model reproduces the sign flip for the consecutive resonances which is also observed in experiments, which increases the confidence in the model.

Modification of the first resonance by inhomogeneity is shown in Fig. 3.5. Compared to the case $\boldsymbol{L} = 10^4$, this resonance is unchanged by configurations that have $L_1 = 0$ (i.e., the first cosine in $L(x)$ in (3.24)). Similar observation holds for 2nd and 3rd resonance, as can be seen in Fig. 3.6.

The numbers in Fig. 3.6 can be extrapolated to a relation that nth resonance measures $L^{\{n\}}$ given by

$$L^{\{n\}} = L_0 + \frac{1}{2}L_n, \tag{3.25}$$

where the second term intuitively corresponds to "weighted averaging" of $L(x)$ (or simply the calculation of the nth Fourier component) $\int_0^d L(x)\cos(2\pi nx/d)\,\mathrm{d}\,x$.

It is worth noting that these values are meaningful and directly relatable to the density of the vortex tangle, thus the use of (1.8) is valid even in inhomogeneous environments.

Experimentally, it was found that $L^{\{2\}} \approx 2L^{\{1\}}$, or, using (3.25), $L_2 =$

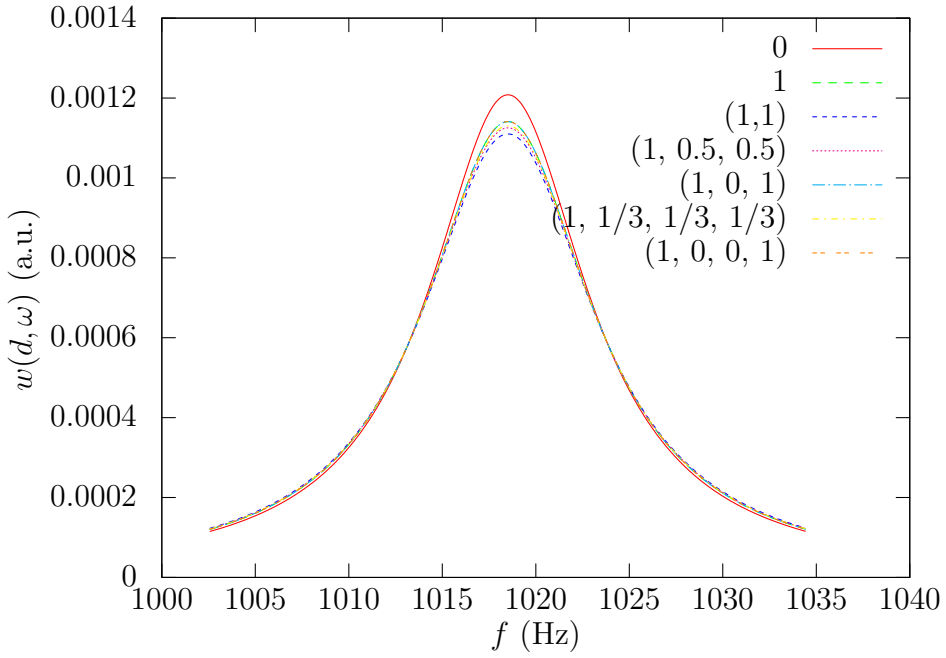

Figure 3.5: Modification of the first resonance by the presence of the inhomogeneity in $L(x)$. The shows $\boldsymbol{L}$ is in units of 10^4cm^{-2}.

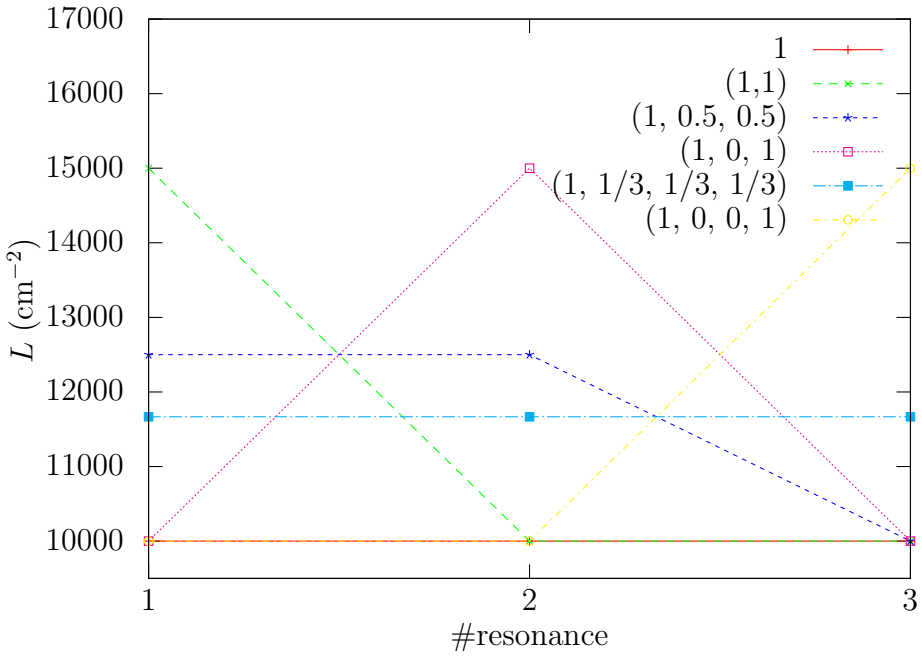

Figure 3.6: Vortex line density as detected by various resonances for different $\boldsymbol{L}$. Each resonance is sensitive only to its corresponding Fourier component of $L(x)$. The legend shows $\boldsymbol{L}$ in units of 10^4cm^{-2}.

$2(L_0 + L_1)$. The only occasionally measured 3rd resonance places $L^{\{3\}}$ somewhere between 1 and 2. Vortex line density must be everywhere non-negative, so it is reasonable to assume that L_2 will not be much larger than L_0, putting $L_2 = L_0$ we find that $L_1 = -L_0/2$ and that $L^{\{1\}} = 3L_0/4$, i.e. the measurement with the first resonance determines the mean vortex line density to within 25%. Note that due to possible unknown polarisation of the vortex tangle, formula (1.8) has an intrinsic uncertainty of about 33% (see Appendix A), thus in this case, within the first approximation, the inhomogeneity merely enlarges the error bars on L by less than a factor of two, which has already been included in the analysis of the effective kinematic viscosity derived from the dependence of vortex line density upon the mean flow.

Conclusion

Quantum turbulence in superfluid ^{4}He was studied in two different configurations of a co-flow of both the normal fluid and the superfluid component of He-II through a channel of a square cross-section. Both configurations had an upstream flow conditioner meant to destroy large eddies on the inflow to the channel, and in the second run an additional regular grid was added closely upstream from the detection region. The detection technique was the second sound attenuation and as the flow source a low-temperature stainless steel bellows was used.

Turbulence was studied by measuring vortex line density L either as a function of the mean flow velocity V in the steady state or its time dependence in the decay after the mean flow is stopped. The experimental results (chapter 2) are thus divided into two main areas:

- in the steady state (section 2.1), robust temperature-independent scaling of the form $L \propto V^{3/2}$ was observed for both configurations with absolute value of L being approximately twice as large for the run with the additional grid. These measurements extend the previously available experiments [12, 17] in both temperature range and small velocities.

  The $L \propto V^{3/2}$ scaling contrasts with the vastly different temperature-dependent $L \propto V^2$ scaling observed in the same channel with the flow conditioner replaced by a superleak, a silver sinter "plug" that allows only the superfluid component to flow through. The superflow measurements represent an earlier work of the author and were also the subject of the author's Bachelor thesis. This study was published in [9] (reproduced as Attachment 1).

  Different vortex line density is measured at different resonant frequencies of the second-sound resonator. This is interpreted as evidence of inhomogeneous distribution of the vortex line density within the turbulent tangle of vortices.

- in the decay of the quantum turbulence (section 2.2), in sufficiently late period a typical $L \propto t^{-3/2}$ decay law is observed. This late time decay is independent of the initial state of the turbulence and, if the time axes of individual $L(t)$ curves are appropriately shifted, all datasets collapse onto a single line.

To explain the $L \propto V^{3/2}$ scaling of vortex line density in the steady state, two models based on the counterflow theory, in particular the Vinen equation

(3.7), are explored in section 3.2. These models try to connect the mean flow velocity V with the mean *counterflow* velocity w entering the Vinen equation in the following two ways:

- in subsection 3.2.1 the mean counterflow velocity w arises as a consequence of differing velocity profiles of the normal and superfluid component of He-II across the channel. The velocity profiles of the two components are at present unknown, so such explanation is in principle possible, however, it is unlikely since its probable consequence is a gradual onset of the $L \propto V^{3/2}$ scaling, which is not observed experimentally.

- the second approach in subsection 3.2.2 replaces the mean counterflow velocity w in the Vinen equation with the RMS of counterflow velocity fluctuations. This approach relies on dimensional analysis that predicts an unlikely result that w decreases with increasing L. In addition, this model requires again that the intensity of turbulence is Reynolds-independent and uses classical scaling laws. Thus the set of assumptions of this model is not particularly reduced, or even changed, from the quasi-classical picture.

Both of the abovementioned models are based on the Vinen equation, and thus should contain temperature-dependent coefficients. No significant temperature dependence is observed in the experiments what makes these models an unlikely explanation for the observations.

In section 3.3 the effect of inhomogeneous vortex line distribution on the measurement technique is studied. A mathematical model of the second sound resonator is constructed and the attenuation by inhomogeneous tangle is simulated. A simple relation connecting the vortex line density deduced by (1.8), which assumes homogeneous vortex tangle, and the Fourier components of the vortex line density is found. As a first approximation, the error on the mean vortex line density as measured by the first resonant frequency of the second sound resonator due to the inhomogeneity is estimated to be around 25%.

The main approach to the experimental data is the framework of quasi-classical quantum turbulence explaining both the steady state and the decay experiments discussed in section 3.1. In this approach, He-II is described as a single fluid with some *effective kinematic viscosity* $\nu_{\mathtt{eff}}$ that describes the dissipation of turbulent energy through essentially classical theory. The decay experiments allow direct extraction of $\nu_{\mathtt{eff}}$ as described in [1]. It is also possible to extract $\nu_{\mathtt{eff}}$ from the steady state, however, additional assumptions are required. Namely the turbulence intensity and the large scale of the turbulence are unknown in the

present experiments, therefore they are treated as fitting parameters and their Reynolds number independence must be assumed. With these assumptions, deduction of $\nu_{\mathtt{eff}}$ is possible and the extracted values approximately agree with the current decay experiments and the original Oregon decay data [1].

The decay measurements were published in Journal of Low Temperature Physics [15] (reproduced as Attachment 2). The steady state measurements and the quasi-classical model explaining them are submitted to Europhysics Letters (latest draft at the time of writing reproduced as Attachment 3)[8].

[8]The models based on counterflow theory, together with the model of the second sound resonance, represent an independent work of the author of the thesis and are not related to these publications in terms of collaboration with their respective coauthors.

Bibliography

[1] Stalp, S. R., Skrbek, L., and Donnelly, R. J. Decay of grid turbulence in a finite channel. *Physical Review Letters*, 82, (1999), 4831–4834.

[2] Skrbek, L. and Stalp, S. R. On the decay of homogeneous isotropic turbulence. *Physics of Fluids*, 12 (8), (2000), 1997–2019.

[3] Skrbek, L. and Sreenivasan, K. R. Developed quantum turbulence and its decay. *Physics of Fluids*, 24 (1), (2012), 011301.

[4] Skrbek, L. *et al. Fyzika Nízkých Teplot, část I.* Matfyzpress (2011). ISBN 978-80-7378-168-2.

[5] Tilley, D. R. and Tilley, J. *Superfluidity and superconductivity*. Institute of Physics, 3rd. edition (1990). ISBN 0-7503-0033-7.

[6] Donnelly, R. J. *Quantized vortices in helium II*. Cambridge University Press (1991). ISBN 0-521-01814-5.

[7] Hall, H. E. and Vinen, W. F. The rotation of liquid helium II. II. the theory of mutual friction in uniformly rotating helium II. *Proceedings of the Royal Society of London. Series A. Mathematical and Physical Sciences*, 238 (1213), (1956), 215–234.

[8] Barenghi, C. F., Donnelly, R. J., and Vinen, W. F. *Quantized vortex dynamics and superfluid turbulence*, volume 571. Springer (2001). ISBN 3-540-42226-9.

[9] Babuin, S., Stammeier, M., Varga, E., Rotter, M., and Skrbek, L. Quantum turbulence of bellows-driven ^{4}he superflow: Steady state. *Physical Review B*, 86 (13), (2012), 134515.

[10] Gordeev, A. V., Chagovets, T. V., Soukup, F., and Skrbek, L. Decaying counterflow turbulence in he II. *Journal of low temperature physics*, 138 (3-4), (2005), 549–554.

[11] Chagovets, T. V., Gordeev, A. V., and Skrbek, L. Effective kinematic viscosity of turbulent he II. *Physical Review E*, 76 (2), (2007), 027301.

[12] Holmes, D. S. and Sciver, S. W. V. Attenuation of second sound in bulk flowing he II. *Journal of Low Temperature Physics*, 87 (1-2), (1992), 73–93.

[13] Varga, E. *Second sound as a tool to study quantum turbulence generated by superflow of He II.* Bachelor thesis, Charles University in Prague, Faculty of Mathematics and Physics, Ke Karlovu 3, 121 16 Praha 2 (2012).

[14] Vinen, W. F. Mutual friction in a heat current in liquid helium ii. iii. theory of the mutual friction. *Proceedings of the Royal Society of London. Series A. Mathematical and Physical Sciences*, 242 (1231), (1957), 493–515.

[15] Babuin, S., Varga, E., and Skrbek, L. The decay of forced turbulent coflow of he II past a grid. *Journal of Low Temperature Physics*, 175, (2014), 324–330.

[16] Smith, M. R., Donnelly, R. J., Goldenfeld, N., and Vinen, W. F. Decay of vorticity in homogeneous turbulence. *Physical Review Letters*, 71 (16), (1993), 2583.

[17] Salort, J., Roche, P.-E., and Lévêque, E. Mesoscale equipartition of kinetic energy in quantum turbulence. *Europhysics Letters*, 94 (2), (2011), 24001.

[18] Vinen, W. F. Classical character of turbulence in a quantum liquid. *Physical Review B*, 61 (2), (2000), 1410.

[19] Pope, S. B. *Turbulent flows.* Cambridge University Press (2000). ISBN 0-521-59886-9.

[20] Uruba, V. *Turbulence.* České Vysoké Učení Technické v Praze (2009). ISBN 978-8-00-104330-1.

[21] Wacks, D. H. and Barenghi, C. F. Shell model of superfluid turbulence. *Physical Review B*, 84 (18), (2011), 184505.

[22] Comte-Bellot, G. and Corrsin, S. The use of a contraction to improve the isotropy of grid-generated turbulence. *Journal of Fluid Mechanics*, 25, (1966), 657–682.

[23] Donnelly, R. J. and Barenghi, C. F. The observed properties of liquid helium at the saturated vapor pressure. *Journal of Physical and Chemical Reference Data*, 27 (6), (1998), 1217–1274.

A. Some second sound attenuation formulas

Derivation of the second-sound attenuation formulas used for the interpretation of the measurements is provided in this appendix. The basis of the calculations are the two-fluid Landau equations (1.5),

$$\rho_s \left(\frac{\partial \boldsymbol{v}_s}{\partial t} + (\boldsymbol{v}_s \cdot \nabla) \boldsymbol{v}_s \right) = -\frac{\rho_s}{\rho} \nabla p + \rho_s s \nabla T - \boldsymbol{F}_{ns}, \tag{A.1}$$

$$\rho_n \left(\frac{\partial \boldsymbol{v}_n}{\partial t} + (\boldsymbol{v}_n \cdot \nabla) \boldsymbol{v}_n \right) = -\frac{\rho_n}{\rho} \nabla p - \rho_s s \nabla T + \mu \Delta \boldsymbol{v}_n + \boldsymbol{F}_{ns} + \boldsymbol{F}, \tag{A.2}$$

and the equations of continuity of mass,

$$\frac{\partial \rho}{\partial t} = \frac{\partial}{\partial t}(\rho_n + \rho_s) = -\nabla \cdot (\rho_n \boldsymbol{v}_n + \rho_s \boldsymbol{v}_s), \tag{A.3}$$

and the entropy density,

$$\frac{\partial}{\partial t}(\rho s) = -\nabla \cdot (\rho s \boldsymbol{v}_n), \tag{A.4}$$

where $\boldsymbol{F}$ is arbitrary forcing on the normal fluid alone, s is the entropy per unit mass, $\boldsymbol{F}_{ns}$ is the mutual friction force (1.6) and $\rho = \rho_s + \rho_n$.

The aim is to obtain the wave equation for the second sound. The wave is considered weak so that it does generate turbulence on its own, thus the fluid velocities involved in the propagation of the second sound are considered small and the non-linear terms of the (A.1, A.2) can be neglected. For the same reasons derivatives of density ρ (or ρ_s, ρ_n), entropy density s and the force $\boldsymbol{F}$ are considered small as well. In the following, terms nonlinear in small quantities are neglected. It is further admissible to neglect the viscous dissipation in the normal fluid due to small viscosity of the normal component. Multiplying (A.1) by ρ_n/ρ_s and subtracting it from (A.2) (with the appropriate terms neglected),

$$\rho_n \frac{\partial}{\partial t} \boldsymbol{w} = \rho_n \frac{\partial}{\partial t}(\boldsymbol{v}_n - \boldsymbol{v}_s) = -\rho s \nabla T + \frac{\rho}{\rho_s} \boldsymbol{F}_{ns} + \boldsymbol{F}. \tag{A.5}$$

Multiplying (A.3) by s, subtracting it from (A.4),

$$\nabla \cdot \boldsymbol{w} = -\frac{\rho}{s\rho_s} \frac{\partial s}{\partial t} = -\frac{\rho}{s\rho_s} \frac{\partial s}{\partial T} \frac{\partial T}{\partial t}. \tag{A.6}$$

Applying ∇ to (A.5), exchanging time and space derivatives of the temperature T and expressing ∇T from (A.5),

$$\nabla T = \frac{1}{s\rho} \left(\frac{\rho}{\rho_s} \boldsymbol{F}_{ns} + \boldsymbol{F} \right) - \frac{\rho_n}{s\rho} \frac{\partial \boldsymbol{w}}{\partial t}, \tag{A.7}$$

the wave equation is obtained

$$\nabla(\nabla\cdot\boldsymbol{w})=\frac{\rho_n}{s^2\rho_s}\frac{\partial s}{\partial T}\frac{\partial^2\boldsymbol{w}}{\partial t^2}-\frac{\rho}{s^2\rho_s^2}\frac{\partial s}{\partial T}\frac{\partial\boldsymbol{F}_{ns}}{\partial t}-\frac{1}{s^2\rho_s}\frac{\partial s}{\partial T}\frac{\partial\boldsymbol{F}}{\partial t}. \tag{A.8}$$

Identifying the seconds sound velocity,

$$c_2=s\sqrt{\frac{\rho_s}{\rho_n}\frac{\partial T}{\partial s}}, \tag{A.9}$$

the wave equation reads

$$\nabla(\nabla\cdot\boldsymbol{w})=\frac{1}{c_2^2}\frac{\partial^2\boldsymbol{w}}{\partial t^2}-\frac{\rho}{\rho_s\rho_n}\frac{1}{c_2^2}\frac{\partial\boldsymbol{F}_{ns}}{\partial t}-\frac{1}{\rho_n c_2^2}\frac{\partial\boldsymbol{F}}{\partial t}. \tag{A.10}$$

Neglecting the non-dissipative second term in the mutual friction (1.6) (i.e, projecting it on $\boldsymbol{w}$), $\boldsymbol{F}_{ns}$ becomes

$$\boldsymbol{F}_{ns}=-B\kappa L\frac{\rho_s\rho_n}{2\rho}\boldsymbol{w}(\sin\vartheta)^2, \tag{A.11}$$

where ϑ is the angle between $\boldsymbol{w}$ and superfluid vorticity $\boldsymbol{\omega}$. This angle is in principle unknown, so an average over the all possible orientations of $\boldsymbol{\omega}$ and $\boldsymbol{w}$ is taken, i.e, the vortex lines are completely isotropic with their orientation having uniform probability distribution over the solid angle Ω, $\rho_l(\Omega)=1/4\pi$,

$$\left\langle(\sin\vartheta)^2\right\rangle=\frac{1}{4\pi}\int_0^{\pi}\int_0^{2\pi}(\sin\vartheta)^3\,\mathrm{d}\,\varphi\,\mathrm{d}\,\vartheta=\frac{2}{3}. \tag{A.12}$$

There are two extreme cases for possible polarisation: either the vortices are aligned parallel to $\boldsymbol{w}$, i.e, $\rho_l(\Omega)=\delta(\vartheta)/2\pi$, what would give $\langle(\sin\vartheta)^2\rangle=0$ or perpendicular to $\boldsymbol{w}$, $\rho_l(\Omega)=\delta(\vartheta-\pi/2)/2\pi$, what would give $\langle(\sin\vartheta)^2\rangle=1$. Therefore if all the vortices were perpendicular to the propagation of sound (i.e., all the vortices would be aligned stream-wise), assumption of isotropy would underestimate L by approximately 33%.

Substituting (A.11) to (A.10) with the assumption of isotropy gives (3.19). To derive the commonly used attenuation formula (1.8), $\boldsymbol{F}$ is further disregarded. The detailed derivation is in the appendix of the paper reproduced in Attachment 1.

List of Abbreviations

RMS – root-mean-square

He-I – liquid ^{4}He above the superfluid phase transition

He-II – superfluid phase of liquid ^{4}He

Attachments

In the articles in Attachments 2 and 3 the work of the author of the thesis consisted of performing the measurements themselves, creating the software necessary for data analysis and the initial analysis itself, except for the numerical simulations in the draft submitted to Europhysics Letters. For article in Attachment 1, the author performed a part of the measurements and analysis. The author of the thesis also created the temperature control system used in the second and the third article attached and the automated measurement system required for the ensemble averaging of the decay data in the article in Attachment 2.

The proposed models and interpretations in the following articles are the result of a collaborative effort of all of the coauthors. All other models and interpretations mentioned in this thesis represent an independent work of the author of the thesis.

Attachment 1. Quantum turbulence of bellows-driven ^{4}He superflow: Steady state

PHYSICAL REVIEW B **86**, 134515 (2012)

Quantum turbulence of bellows-driven ^{4}He superflow: Steady state

S. Babuin,[1] M. Stammeier,[2,*] E. Varga,[2] M. Rotter,[2] and L. Skrbek[2]
[1]*Institute of Physics ASCR, Na Slovance 2, 182 21 Prague, Czech Republic*
[2]*Faculty of Mathematics and Physics, Charles University, Ke Karlovu 3, 121 16 Prague, Czech Republic*
(Received 8 July 2012; published 11 October 2012)

Quantum turbulence in superfluid ^{4}He is studied by the attenuation of second sound in flow channels of 7-mm and 10-mm side square cross sections, and 115-mm length. The ends of the channels are plugged by sintered silver superleaks to allow a pure superflow (i.e., a net flow of the superfluid component only). Flows are generated by mechanically operating a low temperature bellows assembly, as opposed to the helium fountain pump commonly used for previous superflow turbulence studies. The temperature range is $1.35\ \mathrm{K} \leqslant T \leqslant 1.95\ \mathrm{K}$, at the saturated vapor pressure. The observed turbulent steady state is characterized by the vortex line density $L^{1/2} = \gamma(T)(v - v_c)$, where v is the mean superflow velocity and v_c is the critical velocity for the onset of turbulence. The character of the steady state agrees with the Vinen phenomenological model for thermal counterflow turbulence. The coefficient $\gamma(T)$ is in fair agreement with previous thermal pure superflow and counterflow experiments. The critical velocity $v_c \approx 0.2$ cm/s is roughly temperature independent.

DOI: 10.1103/PhysRevB.86.134515 PACS number(s): 67.25.dg, 67.25.dk, 67.25.dm

I. INTRODUCTION

Quantum turbulence (QT)[1] is the most general form of motion of quantum fluids displaying superfluidity, and represents an interesting physical system for a deeper understanding of turbulence in classical fluids, too. QT in superfluid ^{4}He at finite temperature is physically richer than conventional turbulence in viscous fluids because of the two-fluid nature of superfluid helium.[2] The zero-entropy superfluid component can flow without dissipation at low velocity, while being subject to quantum mechanical constraints: The only form of rotational motion allowed is a thin vortex line, whose circulation around the core is not arbitrary as in classical fluids, but quantized in units of $\kappa = 0.997 \times 10^{-7}\ \mathrm{m}^2/\mathrm{s}$.

Unlike the $T \to 0$ K limit where the normal component is absent, at finite temperatures, say for $T \gtrsim 1$ K, QT in superfluid ^{4}He involves the dynamics of a tangle of such quantized vortices coupled by the mutual friction force to the viscous normal fluid component, that itself can easily become turbulent.[3] QT in superfluid ^{4}He at finite temperature thus represents the experimentally easily accessible but intellectually most challenging case. Experimental investigation is instrumental here, as at present neither purely theoretical nor numerical studies are capable of taking into account with sufficient precision all details of mutually interacting turbulent superfluid and normal velocity fields.

In most early works, starting with the pioneering experiments of Vinen,[4] QT was studied in counterflow, the thermally activated motion of normal and superfluid components in opposite directions. Thermal counterflow has a turbulent steady state (in fact, three different turbulent states have been identified by Tough;[5] see later) with no obvious classical counterpart, but displays a classical-like character of its late time decay.[6–9]

When instead QT is generated with methods used for classical flows (resulting in so-called co-flows), similarities with classical turbulence appear more clearly, both in the steady-state properties (Kolmogorov inertial range in energy spectrum in various flows, e.g., between counter-rotating propellers,[10] grid and wake flows in pressurized wind tunnel and "chunk" turbulence flow;[11] Kolmogorov "4/5-law" in pipe flow[12]) as well as in the character of the decay (towed grid,[6,13,14] spin down[15]), despite quantum-mechanical restrictions on the motion of the superfluid component. Experimental research proceeded hand in hand with theoretical and computational studies, starting from the influential work of Schwarz.[16] Comprehensive consideration of theoretical and computational aspects lays beyond the scope of our article, however, two theoretical works closely related to the present project will be discussed in due course.

In general, three distinct cases of ^{4}He QT at $T \gtrsim 1$ K are of particular interest: (i) thermal counterflow, (ii) co-flowing normal and superfluid components, and (iii) pure superflow (i.e., the net flow of the superfluid component only). In this project we have studied properties of QT in pure superflow, generated for the first time mechanically, as opposed to thermally by helium fountain pump, as reported in previous works.[17–19] Low temperature bellows for the generation of superfluid helium pipe flows have been already used by Van Sciver and co-workers who studied pressure drop for steady forced co-flow.[20]

Our project focuses on the single component net flow, integrating measurements of vortex line density by second sound attenuation, in steady and decaying turbulence. Let us stress that, despite that this flow is generated by classical means (mechanical bellows compression), thanks to the ability of superleaks to filter out the normal fluid flow, the resulting steady net pure superflow inside the channel does not have any obvious classical analog. In this article we discuss the steady state and onset of such turbulent flow, while a forthcoming article will be dedicated to its decay. The article is organized as follows: Sec. II describes our experimental setup and protocol, Sec. III contains our experimental results, which are discussed and compared with relevant previous experiments in Sec. IV; we conclude in Sec. V. A step-by-step derivation of the relationship between the vortex line density and the measured amplitude of second sound [which is essential in this work; Eq. (2)], is given in the appendix.

II. APPARATUS AND METHOD

A. Flow channel, flow generation, and thermometry

The apparatus used is illustrated in Fig. 1. A net flow of superfluid component through a flow channel is generated by compressing a stainless steel bellows filled with superfluid ^{4}He and immersed in the open cryostat bath.

Two brass flow channels have been used, with internal square cross section of side 7 mm and 10 mm, and finely polished walls. Both channels are 115-mm long and have an outer dimension of 32 mm. The channel ends are plugged by silver-sintered superleaks (i.e., filters constituted by packing of silver spheres with a 1/2 volume filling fraction), resulting in submicron-sized pores to prevent a net flow of the viscous normal component through the channel on any flow time scale relevant to the experiment.[21] The superleaks are designed having in mind not to plug the internal cross section directly: The channel ends have a roughly conical expansion of diameter 16 mm (not shown in Fig. 1) to which the 2-mm-thick sintered silver superleaks are sintered *in situ*, thus the effective output cross section for the flow through the superleaks is not smaller than the cross section seen by the flow in the channel.

The bellows is driven by a computer-controlled motor located on the cryostat flange at room temperature, and connected to the bellows via gear box and shaft. The motor can perform micron-accuracy positioning and can control the velocity to within about 1%. The mean channel superflow velocity v is calculated by requiring that the mass flow rate of liquid out of the bellows equals the mass flow rate into the channel, assuming the liquid incompressible. The bellows volume has been calibrated at room temperature to within about 2% accuracy. The mean flow velocity in the channel is given by

$$v = v' \frac{\partial V}{\partial h} \frac{1}{A}, \tag{1}$$

where v' is the velocity of the shaft along the vertical displacement h (measured by the motor's encoder), V is the bellows volume, and A is the cross section of the flow channel. The maximum volume that can be displaced by the bellows is about 400 ml, and from the calibration we obtained $\partial V/\partial h = 4.25 \pm 0.08$ ml/mm; overall the flow velocity is known to within 3% accuracy. During cool-down, the bellows is filled with helium gas; liquid helium enters it below the lambda transition via the channel, and it easily fills the whole volume. Flows are studied only when generated by compressing the bellows, not expanding it, that is to say, when the flow velocity can be deduced unambiguously from Eq. (1).[22] Once the bellows is fully compressed, liquid helium is recharged by expanding it.

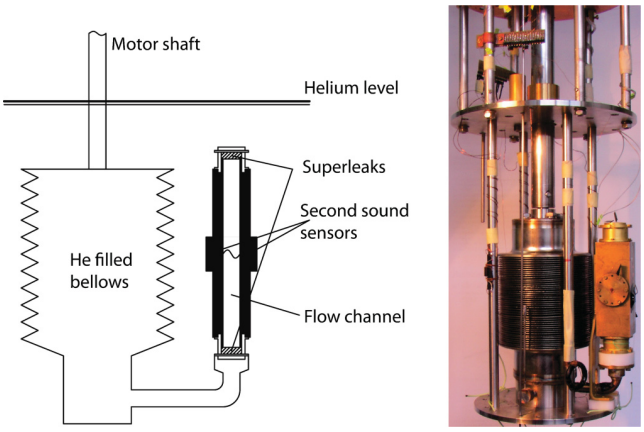

FIG. 1. (Color online) Schematic diagram and photograph of the bellows with the flow channel.

The experiments have been carried out in the temperature range 1.35 K $\leqslant T \leqslant$ 1.95 K, at the saturated vapor pressure. The absolute temperature of the bath is deduced from the vapor pressure (measured via a separate line ending in the cryostat close above the liquid bath level) and its fluctuations are measured with a carbon resistance thermometer immersed in the bath near the channel, itself calibrated against the vapor pressure. The bath temperature is controlled either by manual regulation of the pumping rate, or with a temperature controller which uses as a reference the carbon thermometer and a manganin heater wire immersed in the bath. We choose whichever method gives a temperature control of about 1 mK or better. Other two calibrated carbon thermometers are located inside the bellows. All carbon thermometers are used primarily as relative thermometers, since they are slightly affected by thermal cycling. Their absolute reading is accurate to within about 10 mK. No thermometers are installed inside the channel to avoid disturbing the flow.

B. Second sound attenuation

QT is detected by the attenuation of second sound propagating in a direction perpendicular to the mean superflow. The second sound experiences attenuation additional to bulk viscous losses when the thermal excitations constituting the normal component are scattered by the vortex filaments. The second sound speaker and receiver are circular membranes of 9-mm diameter with micron-size holes, located at mid channel length (see Fig. 1; additionally, a blow-up drawing of the channel and more construction details are given in Ref. 19). The speaker membrane induces a second sound wave by oscillating and displacing only the viscous normal component of helium, thereby causing higher local concentration of normal component and hence higher temperature. The channel walls constitute a resonator for such wave. The membranes have one gold-plated side in contact with the channel body biased typically with 100 V and a circular brass electrode is spring loaded against the other side, thus forming a capacitor with one vibrating plate. In order to achieve the highest signal-to-noise ratio, the drive amplitude is adjusted close below the level at which the second sound signal versus drive dependence starts to deviate from linearity—typically between 6 and 10 V.

An example of the signal detected by the second sound receiver is shown in Fig. 2. The figure shows how the resonant curve for quiescent helium is attenuated and broadened as flows of increasing steady-state velocity are produced in the channel. The frequency spectra have been acquired in conditions of fully developed steady flow. Note the existence of additional smaller peaks that most likely occur due to weak coupling to longitudinal second sound resonances in the channel. Experimentally, we always tried to use the harmonics

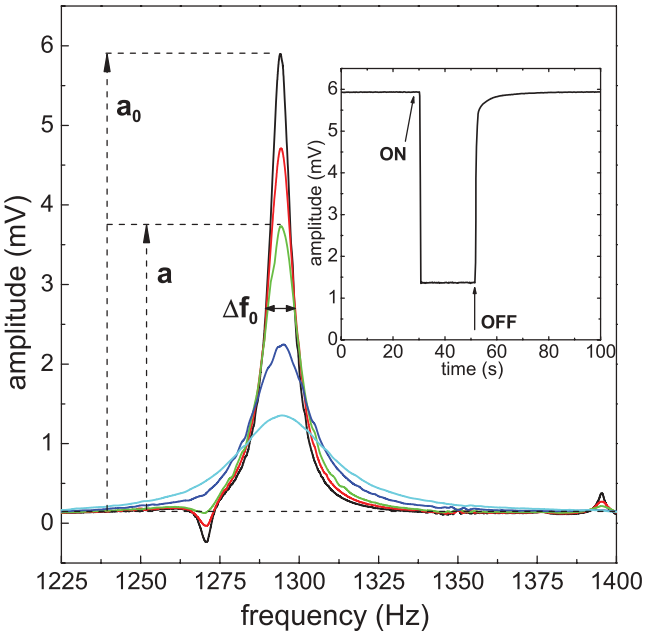

FIG. 2. (Color online) Second sound resonance curves (first mode) for different steady-state flow velocities in the 7-mm wide channel at $T = 1.35$ K. The tallest curve corresponds to the case of no flow in the channel, while others correspond to flow velocities of, from top to bottom, 1.73, 2.60, 4.33, and 6.07 cm/s. (Inset) The second sound amplitude at resonance monitored in time as a flow of steady velocity 6.07 cm/s is switched on and off (same flow velocity as most attenuated curve in main plot).

(in most cases the fundamental or its first overtone) which for particular conditions were least affected by these parasitic resonances. We have, however, thoroughly verified that results are in no way affected by the choice of harmonic.

One can see in Fig. 2 that the central frequency is not changed by the flow. This enables one to carry out a simplified experiment where one samples in time the second sound amplitude *at* the resonant frequency, observing the changes occurring upon switching on a flow, maintaining its steady state, and switching it off. An example of one such time series is shown in the inset and provides the basis for the study of the decay transient.

In this article we shall be solely concerned with the steady-state properties of the flow. The decay transient also contains valuable physical information and will be discussed in a follow-up article. In the steady state the signal is sampled at a rate of 5 points per second, and each point is averaged with a lock-in amplifier time constant of 100 ms (for comparison, the time for a second sound wave traveling at $\approx$20 m/s to complete a return trip in the 1-cm wide channel is 1 ms). The amplitude averaged during the steady state has a standard deviation of less than 1% and during that process the temperature is usually kept constant to better than 1 mK.

The second sound attenuation technique does not detect the absolute vortex line length, but a quantity proportional to the average of the square of the sine of the angle between the vortex lines and the second sound propagation direction.[23] Therefore, to infer the absolute length one needs to know the actual spatial distribution of the lines. This is in general not known, and perhaps cannot be known with certainty unless directly visualized, which is not possible in this setup. Therefore an assumption on the vortex line distribution is necessary. Assuming that the vortex tangle is homogeneous and isotropic, the total length of vortex lines per unit volume L can be deduced from the measurement of the second sound amplitude a as follows:

$$L = \frac{6\pi \Delta f_0}{B\kappa}\left(\frac{a_0}{a} - 1\right), \tag{2}$$

where a_0 and Δf_0 are the amplitude and the full width at half maximum of the second sound resonance without flow, and B is the mutual friction coefficient (tabulated in Ref. 24). All vortex line density computed in this article originates from this equation. Another limiting case exists, that of vortex lines all lying in planes parallel with the direction of second sound propagation, and randomly oriented within that plane. In that case L in Eq. (2) is reduced by a factor 4/3. Hints on the derivation of this equation are provided, for example, in Refs. 25 and 9 but a full derivation is given here for convenience in the appendix. The non-attenuated resonance width Δf_0 is obtained from a Lorentzian fit of the full resonant curve as shown in Fig. 2, while a_0 and a have been obtained both from fits and from averaging the amplitude signal of the type shown in the inset.

C. Temperature gradients

In this final section we turn to a discussion of the distribution of temperature in the system. During steady flow the helium *inside the bellows* becomes warmer (as measured by local thermometers), due to the reduction of the superfluid component fraction. Such increase is roughly linear with flow velocity, and roughly independent of mean temperature; it is at most 3 mK for the highest flow velocities considered in this article, of about 20 cm/s. The temperature in the bath, instead, is almost unchanged.

It is important to realize that the warming up of helium inside the bellows cannot alter the mass flow rate through the channel—which is entirely set by the rate of bellows compression—therefore it does not affect the determination of v discussed before. The helium in the channel is in fact thermally well separated from both the helium in the bellows and in the bath, because of low thermal conductivity of brass walls and silver sinter.[26]

Regarding the temperature gradient in the helium *inside the channel*, since no local thermometers are present, an estimation is possible from the two-fluid equations of motion. Subtracting the superfluid from the normal fluid momentum conservation equations in the steady state [see Eqs. (A3) and (A4) in the appendix], and neglecting nonlinear terms and viscous dissipation, one can show that a thermal gradient $\nabla T = \mathbf{F}_{ns}/(\rho_s \sigma)$ arises to balance the mutual friction force $\mathbf{F}_{ns}$, where ρ_s is the density of the superfluid component and σ is the entropy of helium per unit mass. For a tangle of randomly oriented vortex lines we estimate $\nabla T \approx -\kappa \rho_n B L(\mathbf{v}_n - \mathbf{v}_s)/(3\rho\sigma)$, where for $\mathbf{F}_{ns}$ we have used Eqs. (A6) and (A18), $\mathbf{v}_n$ and $\mathbf{v}_n$ are the normal and superfluid velocities, and ρ and ρ_n are, respectively, the total density of helium and of the normal component. For our channel, assuming the normal fluid is at

rest ($\mathbf{v}_n = 0$), we arrive at a maximal temperature difference of order 10 mK for the highest attainable flow velocities, with the temperature increasing along the direction of the superflow. Note incidentally that such thermal gradient exists irrespectively of whether the superflow is driven mechanically (by a bellows) or thermally (by a fountain pump, as in Ref. 19), and has the same orientation.

III. RESULTS

A. Vortex line density versus mean velocity

The steady-state vortex line density is plotted as $L^{1/2}$ versus the mean superflow velocity v in Fig. 3, for the 7-mm-wide channel. Symbols distinguish values of L obtained from the second sound amplitude a, extracted from a Lorentzian fit of the full resonant curve (open symbols), from those for which a is measured directly at resonance (solid symbols), as described in Sec. II B. This second approach is required for $v \gtrsim 10$ cm/s, when the time for the bellows to complete a compression becomes shorter than the time required for a sufficiently detailed scan of the resonance; both approaches agree very well. The data sets are fitted with straight lines of the form,

$$L^{1/2} = \gamma(T)(v - v_c), \tag{3}$$

and the fit is weighted against the relative importance of the experimental error on L. The inset shows that the fitted lines extrapolate to a nearly temperature independent intercept $v_c \approx 0.1$ cm/s. This form of $L(v)$ agrees with the steady-state solution of Vinen's phenomenological equation,[4] which describes well steady-state counterflow.

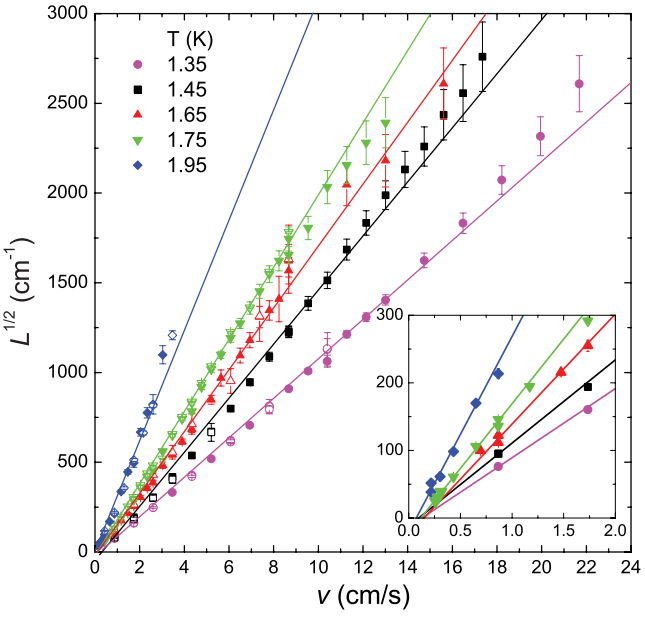

FIG. 3. (Color online) The square root of the steady-state vortex line density L, as a function of mean superflow velocity v, for the 7-mm wide channel, at different temperatures. Open symbols relate to L obtained from the second sound amplitude a extracted from a Lorentzian fit of the full resonant curve, while solid symbols relate to a directly measured at resonance. Straight lines are fits to the data weighted by the uncertainty in L. The inset highlights the existence of a positive intercept, v_c.

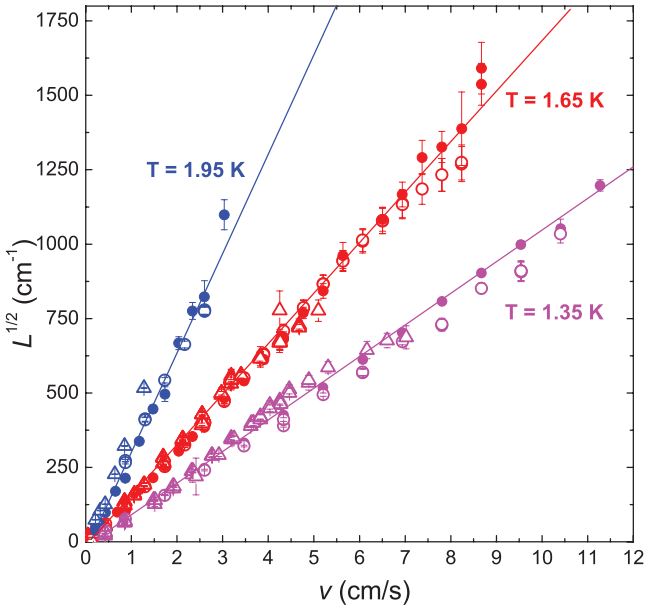

FIG. 4. (Color online) Comparison of results from three different channel configurations. (i) Solid circles, 7-mm channel with both superleaks (as in Fig. 3); (ii) open circles, 7-mm channel with downstream superleak removed; (iii) open triangles, 10-mm channel with both superleaks. Straight lines guide the eye.

In Fig. 4 we show a comparison of some of the data just presented, with results from runs where the downstream superleak was removed from the 7-mm channel and runs with the 10-mm channel with both superleaks present. We see that removal of the downstream superleak does not lead to any appreciable change in the observed steady-state vortex line density in the 7-mm channel, suggesting that the flow is of the same character. Additionally, we find that the observed steady-state vortex line densities in the 7-mm and in the 10-mm channels agree within experimental scatter, again in agreement with Vinen's phenomenological equation.[4]

B. $\gamma(T)$ coefficients

The $\gamma(T)$ coefficients of Eq. (3) are plotted as a function of temperature in Fig. 5, for a variety of systems. Let us first describe the results of the present work. The five slopes of Fig. 3, relating to the 7-mm-wide channel, are represented as solid blue circles, while the green solid squares relate to the same channel with the downstream superleak removed, leading to no appreciable change in γ. The open up-pointing blue triangles are from the 10-mm-wide channel, showing marginally but systematically higher γ than the 7-mm channel. Whether this is attributable to a size effect cannot be easily concluded since, first, only two channel sizes are available, and secondly, the performance of the second sound sensors was poorer in the 10-mm channel run, leading to lower accuracy.

Let us now turn to a comparison with related previous works, starting with two pure superflow experiments. The closest comparison is, in principle, with a previous experiment run in Prague by Chagovets and Skrbek,[19] where the same flow channels and detection technique were used, but the superflow was generated by helium fountain pump, instead of

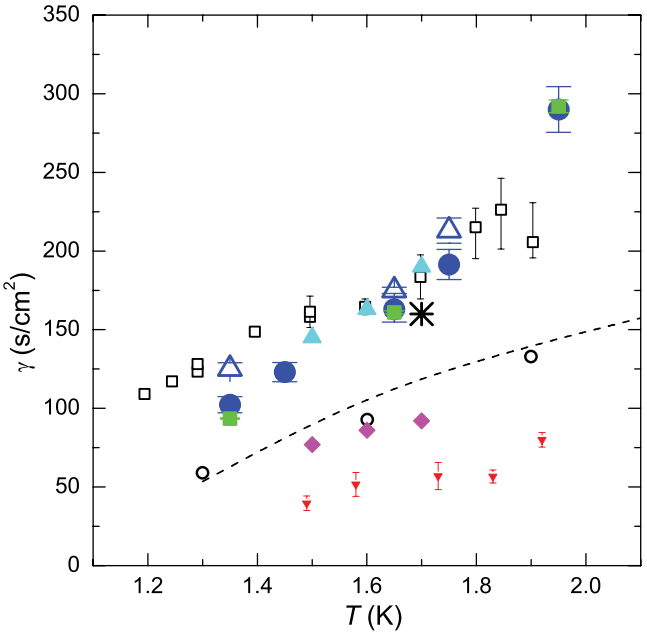

FIG. 5. (Color online) The quantity $\gamma(T)$ of Eq. (3) calculated for available pure superflow and counterflow experiments and simulations. Present work: solid blue circles, 7-mm channel; solid green squares, 7-mm channel, downstream superleak removed; open blue up-triangle, 10-mm channel. Other works: (i) thermally induced pure superflow, open squares, Ashton *et al.*, 0.13-mm diameter glass channel;[17] solid red down-triangle, Chagovets and Skrbek, 7-mm channel as present work, A-state turbulence;[19] (ii) counterflow, solid blue up-triangle, solid magenta diamond, Martin and Tough, TII and TI states, 1-mm diameter glass channel;[27] open circles, Childers and Tough, TI state, 0.13-mm diameter glass channels;[28] asterisk, TII state, 7-mm channel as present work, unpublished; dashed line, *Adachi et al.*, numerical simulation.[29]

bellows. For low velocities (there defined as the A state of pure superflow turbulence) the authors found $L^{1/2} = \gamma(T)(v - v_c)$, while at higher velocities they reported a transition to a B state with $L \propto v$. The A-state slopes are shown here as full down-pointing red triangles: They are very different from the bellows version of the experiment, and also significantly lower than any other surveyed work. As it will be outlined in more detail in Sec. IV, we have now evidence that the flow velocity in the fountain experiment was overestimated by a factor roughly between 2 and 4, depending on temperature and heat current: If corrected by this factor, γ from the fountain-driven flow would be roughly in agreement with the bellows-driven flow. Therefore, for the time being, we shall not be concerned with these results.

We offer instead as relevant comparison the results by Ashton *et al.*,[17] where pure superflow was driven by fountain pump in a cylindrical glass channel, 0.13 mm in diameter, shown as black open squares, in fair agreement with the present work, despite L was deduced from measurements of temperature difference along the channel. Although their channel was very narrow, the average intervortex distance, $1/\sqrt{L}$, was becoming comparable with the channel size only at very low velocity, suggesting that finite size effects did not play an important role, and therefore justifying a comparison with our system.

Let us now consider thermal counterflow experiments. The asterisk marks an unpublished datapoint obtained in Prague with the same 7-mm-wide channel used in this work, but in thermal counterflow. The up-pointing full cyan triangles and the magenta diamonds are from Martin and Tough[27] in a 1-mm-diameter glass channel, relating, respectively, to the TII and TI state of counterflow turbulence. As a reminder, thermal counterflow turbulence in channels with a cross-sectional aspect ratio close or equal to unity and absolute width of order 1 mm or less has been classified by Tough as possessing two turbulent regimes,[5] TI, which immediately follows the laminar state, and TII, occurring above a critical line density, both satisfying $L^{1/2} = \gamma(T)(v - v_c)$ with γ in TII state considerably larger than in TI. These two regimes are not a universal property of counterflow turbulence: A single state has been observed in channels with a very large cross-sectional aspect ratio (although small absolute dimensions, below 1 mm), termed TIII[5] and also in the seminal work of Vinen in channels with cross-sectional aspect ratio of order 1/2, with absolute dimensions of several mm.[4]

In pure superflows only a single regime has ever been observed—the existence of A and B states reported by Chagovets and Skrbek is presently under scrutiny on account of uncertainties on flow velocities occurring in that experiment, as further discussed in Sec. IV B.

The TII state measured by Martin and Tough[27] agrees well with the pure superflow experiments; their corresponding TI state agrees with the TI state in a channel of about 10 times smaller diameter (Childers and Tough, black open circles[28]) and with the numerical simulation of Adachi *et al.*[29] (dashed line). This numerical simulation is based on the solution of the full Biot-Savart integral[23] and therefore takes into account long-range interactions between vortices, and is solved in a domain with periodic boundary conditions. Due to current limitations in computational power, the simulation can reach only modest vortex line densities, within the TI regime.

C. Critical velocities

In the present work we have investigated the critical velocity that corresponds to the onset of QT, by producing long-lasting steady flows (several tens of seconds), gradually increasing the velocity from zero up to a value well into the turbulent regime, and from there reducing it back to zero, observing changes in the second sound amplitude tracked at resonance. An example of such raw data is provided in Fig. 6, where the second sound amplitude is plotted as function of time while the flow velocity is increased in steps of 0.05 cm/s, lasting 50 s each. In this particular case the first departure from noise occurs at around $t = 180$ s, when $v = 0.16$ cm/s. The temperature stability in the bath was 0.1 mK.

Figure 7 shows the mean critical velocity for different systems. Regarding the present work, the ramp-up, and ramp-down critical velocities, averaged over several measurements, are plotted as black open circles and blue open squares, respectively, for the 7-mm channel and as stars for the 10-mm channel (average of very similar ramp-up and ramp-down measurements). These measurements show, within the available resolution, no temperature dependence and no hysteresis effects.

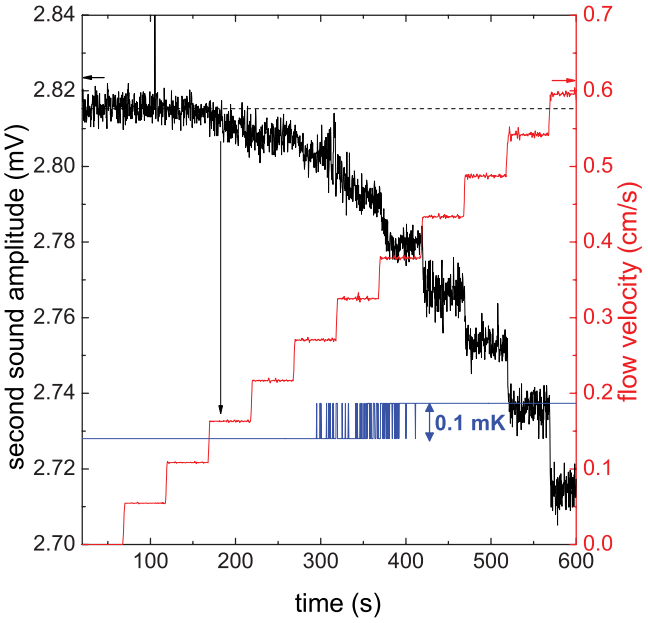

FIG. 6. (Color online) Example of raw data for the determination of critical velocity. The second sound amplitude is tracked at resonance, while the flow velocity is suddenly increased with 0.05 cm/s resolution steps lasting 50 s. Here a change in attenuation distinguishable from the noise floor (dashed line) first appears at around 180 s, when $v = 0.16$ cm/s. The blue line shows the temperature of the bath, stable to within 0.1 mK.

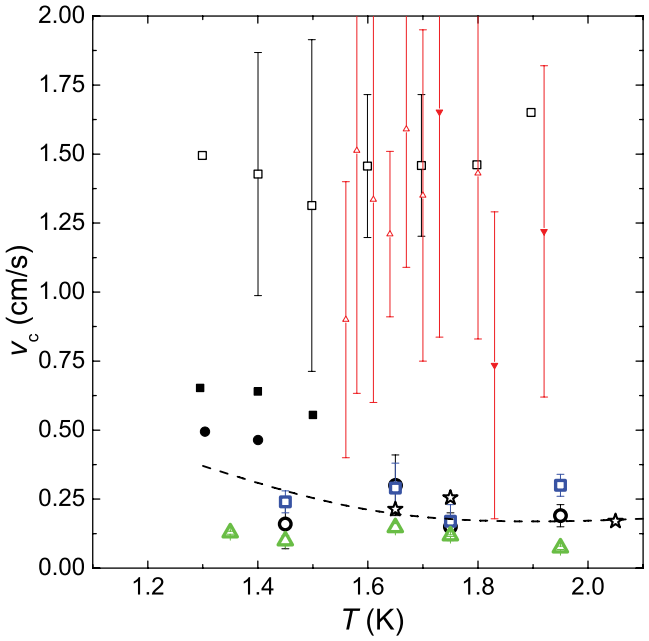

FIG. 7. (Color online) The critical velocity for the onset of turbulence from different experiments and simulations. Present work: open black circles, open blue squares, open green up-triangles = ramp-up, ramp-down, fit extrapolation, 7-mm channel; stars = average of ramp-up and ramp-down, 10-mm channel. Other works: (i) thermal pure superflow, open black squares = Baehr *et al.*, 0.13-mm glass channel;[18] solid red down-triangles = Chagovets and Skrbek, 7-mm and 10-mm channels as in present work;[19] solid black squares, solid black circles = Vinen, 2.4×6.5 mm^2 and 4×7.8 mm^2 channels;[4] dashed line = Adachi *et al.*, numerical simulation.[29]

The results also do not depend on whether the flow velocity is increased (or decreased) quasi-continuously as opposed to in discrete steps, nor do they depend on whether or not the flow velocity is reduced to zero in between each increment in velocity. The averages of ramp-up and ramp-down critical velocities at different temperatures for the 7-mm channel are, respectively, 0.20 ± 0.07 cm/s and 0.25 ± 0.06 cm/s, while the average in the 10-mm channel in 0.21 ± 0.05 cm/s, all agreeing within the uncertainty. For these low flow velocities, the extent of second sound attenuation becomes comparable to the signal noise, as shown in Fig. 6, therefore we conclude that the real critical velocity must be at least as measured, or lower.

The critical velocity can also be estimated from the intersection with the x axis of the straight line fits of Fig. 3 (inset), although this method assumes that the same slope continues to hold at very low velocities. For the 7-mm channel this intercept is 0.11 ± 0.03 cm/s: similar, but a little lower than the direct measurement; this is consistent with the situation in thermal counterflow as summarized by Tough.[5]

Critical velocities found in thermally generated superflow experiments are also provided in Fig. 7. The black open squares are from Baehr *et al.* who used a 0.13-mm diameter glass channel,[18] the same which yielded the black open squares data in Fig. 5, but here the difference with the present work is substantial. Whether or not this counts as a disagreement will depend on whether the critical velocity is an intrinsic property of the flow or depends on channel geometry. Evidence discussed in the next section suggests that the latter is the case.

The red triangles are the critical velocities in the 7-mm and 10-mm-wide channels as used in the present work, but with the fountain-driven superflow.[19] As discussed above, these points are very likely to be incorrect because of the overestimation of superflow velocity, and should for the present purposes be disregarded. If, however, the same temperature-independent correction—which makes the γ coefficients agree—is applied here, we would arrive at a value (temperature-averaged, on account of the large error bars) of 0.50 ± 0.22 cm/s for the thermally induced critical velocity in the 7-mm channel: higher, but consistent with the present bellows experiment which, incidentally, allows for much better control of very low velocities than the fountain method.

The pioneering work of Vinen[4] is also included, with the 2.4×6.5 mm^2 and 4×7.8 mm^2 channels, respectively, in solid black squares and circles.

The simulation of Adachi *et al.*[29] for counterflow with periodic boundary conditions is also shown.

IV. DISCUSSION

A. Pure superflow in the framework of Vinen's counterflow model

The steady-state properties of pure superflow have been analyzed in the previous section according to Eq. (3), in agreement with the steady-state solution of Vinen's model for counterflow.[4] In this model the key parameter which governs the dynamical state of the flow is the counterflow velocity $(\mathbf{v}_n - \mathbf{v}_s)$—no boundary effects are taken into account. The

question now arises as to whether such counterflow framework is sufficient to describe the physics of pure superflow, in other words whether pure superflow can be regarded merely as counterflow in the frame of reference of the normal component ($\mathbf{v}_n = 0$).

From our analysis we conclude that the steady-state solution of the Vinen model gives an equally good *formal* account of both pure superflow and counterflow, and that, further, the γ coefficients for pure superflow are in good quantitative agreement with TII counterflow. However, the fact that a TI counterflow state with much lower γ exists in channels with aspect ratio around unity and sufficiently small absolute cross-sectional dimensions, strongly suggests that the finite size of the channel should be, in general, an additional parameter of the problem.

The transition from TI to TII state has been suggested to be triggered by the transition to turbulence in the normal component,[30] and more recently a convincing experimental evidence that the normal component indeed becomes turbulent for sufficiently high heat currents has been given.[3] What is still missing is a detailed explanation of how the channel cross-section dimensions and shape could control such transition.

What is already well established is that if the channel aspect ratio is sufficiently large, only one regime of counterflow turbulence is observed (TIII, perhaps meaning that the normal component becomes turbulent near or before the onset of turbulence in the superfluid component), and for such regime the γ coefficients are very similar to those of pure superflow. To conclude unequivocally though that counterflow and pure superflow are entirely equivalent, is still a contentious issue, since, for example, the properties of the temporal decay of turbulence are different, especially in the early stages of the decay. This open issue will be explored in a future dedicated article.

Regarding the critical velocity for the onset of turbulence, if the points from Chagovets and Skrbek[19] in Fig. 7 are disregarded on account of their very likely overestimation, it is apparent that the critical velocity decreases in some fashion with increasing channel cross section, a fact which has been long known. The critical velocity for pure superflows and counterflows has been measured in a variety of systems during the decades, and several attempts have also been made to account theoretically for its scaling with channel geometry, which, according to the 1982 review by Tough[5] did not lead to a conclusive theoretical understanding of the problem.

A new theory, however, has recently been proposed by Kruglov,[31] based on the interaction of roton excitations with the walls of the channel. Some results from this work, together with a (partial) survey of experimental data are presented in Fig. 8. The critical velocity v_c is plotted as a function of the smallest dimension of channel cross sections, d. We distinguish pure superflow experiments (solid symbols) from counterflow experiments (open symbols).

Regarding pure superflows, a large compilation of classic results was provided almost half a century ago by Van Alphen *et al.*,[39] from which we have extracted a few, for $d > 10^{-3}$ mm, and present them here (error bars are not provided in the source article); these pure superflow results are temperature independent. We also show the pure superflow data from the 0.13-mm diameter channel of Baehr *et al.*[18] (already shown in Fig. 7, and here temperature averaged) and the two values for our

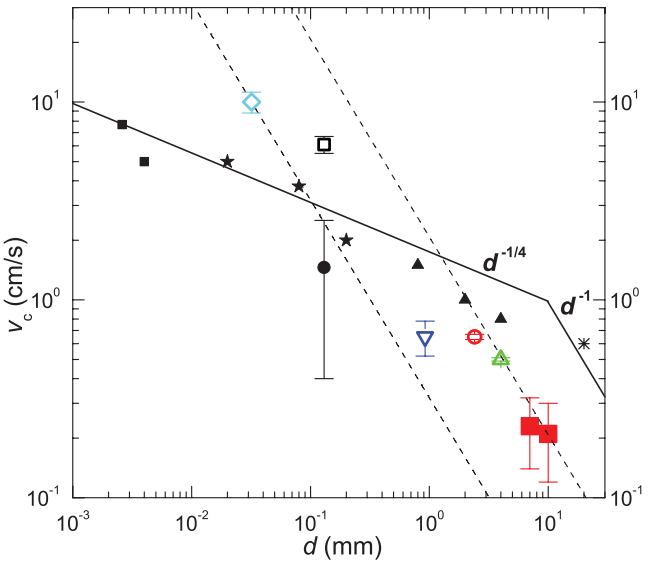

FIG. 8. (Color online) The critical velocity v_c for the onset of turbulence as a function of the smallest dimension of channel cross section d for different systems. Pure superflow experiments (solid symbols), black squares = Hammel & Keller, isothermal flow;[32] stars = Van Alphen *et al.*, adiabatic flow rate;[33] circle = Baehr *et al.*, temperature average of data in Fig. 7;[18] up-triangles = Chase, heat conduction;[34] asterisk = Craig and Pellam, superfluid wind tunnel;[35] red squares = 7×7 mm^2 and 10×10 mm^2, present work, temperature averaged and ramp-up and ramp-down averaged. Counterflow experiments (open symbols), open blue diamond = Ladner and Tough, 0.032×0.32 mm^2;[36] black open square = Childers and Tough, 0.13-mm diameter;[37] blue down-triangle = Yarmchuk and Glaberson, 0.92×11.3 mm^2;[38] open red circle, open green up-triangle = Vinen, 2.4×6.5 mm^2 and 4×7.8 mm^2.[4] Kruglov theory,[31] solid line = predicted absolute scaling of pure superflow critical velocity; dashed lines = predicted scaling for counterflow critical velocity (with undetermined prefactor); lines give a lower and upper bound for the experimental data.

7- and 10-mm channels, also averaged over temperature and ramp-up/ramp-down directions, since we have observed that the critical velocity is almost independent of these parameters. For completeness, we have also added experimental points from some counterflow experiments, for which generally the critical velocity does change with temperature. Here we have chosen values relating to temperatures roughly between 1.3 and 1.35 K, where comparison between different experiments was possible.

The tendency of the critical velocity to decrease with increasing channel size is confirmed, and, although the data points are somehow scattered, it is possible to distinguish different trends for pure superflows and for counterflows. The main part of Kruglov's theory is developed for the case of ideal pure superflows, where the normal component is fully immobilized. The theory predicts $v_c = \Lambda d^{-1/4}$ and $v_c = \Lambda' d^{-1}$, respectively, for $d < 10$ mm and $d > 10$ mm, where Λ and Λ' are calculated theoretical prefactors. This prediction is shown as a solid line. We see that the scaling agrees quite nicely with most pure superflow experimental data, except for the two data points from the present work, which lie about a factor of 5 lower than the prediction.

Van Alphen *et al.*[39] show that in experiments where the normal component is *not* firmly immobilized, a lower critical velocity than predicted by the $d^{-1/4}$ scaling is observed. They argue that in these cases the onset of superfluid turbulence is triggered by a transition to turbulence of the classical type in the normal component, associated with a Reynolds number $\mathrm{Re_n} = v_\mathrm{n} d/\nu_\mathrm{n}$, where ν_n is the effective kinematic viscosity of the normal component. This way, for a given critical $\mathrm{Re_n}$, $v_\mathrm{n} \sim d^{-1}$, and the superfluid critical velocity would scale the same way, from the counterflow conservation of mass condition $\rho_\mathrm{n}\mathbf{v}_\mathrm{n} = -\rho_\mathrm{s}\mathbf{v}_\mathrm{s}$. The authors point out that, conversely, if the normal component is properly immobilized by the use of superleaks, the $d^{-1/4}$ scaling is observed to hold up to rather large channel sizes, as exemplified by the 2-cm wide superfluid wind tunnel used by Craig and Pellam,[35] shown as an asterisk in Fig. 8.

This confirms the view that the turbulence onset is regulated by different physical processes occurring in the normal and superfluid component (classical Reynolds number criterion, versus quantized vortices nucleation) each of which has its own dependence on channel size. Whenever the geometry conditions are such that turbulence onset in the normal component occurs first (at lower velocity) than would occur in the superfluid in its own accord, the transition is triggered in the superfluid, too.

These ideas perhaps suggest that, although our channel is indeed plugged by superleaks, *inside* the channel $\mathbf{v}_\mathrm{n} \neq 0$. This need not imply that there is a net flow of a normal component across the superleaks, merely internal motion of the normal component in the channel. This fact may play a very important role later, in the understanding of the character of turbulence decay.

The Kruglov theory also predicts $v_\mathrm{c} \sim d^{-1}$ scaling for counterflow, where the normal component is free to move, although the prefactor of the scaling is not determined. We have drawn two dashed lines where such prefactor is tuned by a factor of 6.5 in order to enclose all the reported counterflow experimental data. The fact that our two points fall within this band may strengthen the hypothesis that the normal component is not stationary during the observed steady state in the present experiment. This was already suggested by Chagovets and Skrbek[19] about their experiments in Prague performed in identical channels. In the following section we take a closer look at those experiments.

B. Discrepancies between mechanically and thermally driven superflow

In Sec. III we have shown how the present work yielded considerably different $\gamma(T)$ and v_c than its previous realization where the superflow was driven by a heater located inside a nozzle on top of the upper superleak, and held just below the bath surface.[19] In principle one would not expect such a difference to occur solely due to a change in the method of flow generation, because the essential physics of the flow inside the superleak-plugged channel depends on the temperature gradient established along the channel (as argued in Sec. II C) and such gradient would not be conceivably affected by a change of flow source. Therefore we proceed with the assumption that the two turbulent flows ought to have similar properties, and we set out to seek other reasons for the discrepancy.

First, we have carefully re-examined the raw second sound attenuation data from the fountain-driven experiment, and independent evaluation confirms that values of L were determined correctly. We therefore reconsidered the determination of mean superflow velocity. This quantity is unambiguous in the bellows experiment, since it is simply related to the measurement of rate of change of bellows volume. In the fountain experiment, however, the mean superflow velocity was not measured directly, but deduced from the power supplied to the fountain heater placed in the nozzle above the upper superleak $\dot{Q}$ as

$$v = \frac{\dot{Q}}{A\rho_\mathrm{s}\sigma T}. \tag{4}$$

This relationship was shown to be valid under the assumption that $\dot{Q}$ is used *entirely* to drive the flow. However, recent direct measurements in the fountain setup revealed that this is not so, since, for example, a sizeable fraction of the heat provided by the heater is spent to enhance evaporation of liquid helium contained in the nozzle.

We have arranged a few replicas of the original fountain experiment to allow for a direct visual determination of the rate of filling of a calibrated volume downstream the channel, from which we have calculated actual channel velocities. A full account of these measurements, which in themselves for various reasons did not constitute a trivial experiment, will be presented in a dedicated article submitted to the Journal of Low Temperature Physics.

The main message is that Eq. (4) always overestimates the directly measured velocity. In short, for low heat currents v is a few times smaller than predicted (depending on T and $\dot{Q}$) and roughly linear with $\dot{Q}$. This correction brings the γ coefficients of the A state of turbulence of Ref. 19 in rough agreement with those of the bellows-driven flow presented in this article.

An exact correction cannot however be expected, because the flow velocity can be measured - by construction - only while the fluid is filling the calibrated volume, hence before it flows out into the bath, a condition that in principle is different from that of the steady state in Ref. 19. At low heat currents it was also possible, in limited circumstances, to measure second sound attenuation simultaneously. This also confirmed that $L(v)$ of fountain and bellows driven flows are in reasonable agreement. At higher heat currents the measured v grows with $\dot{Q}$ at even slower rate than at low heat currents, and therefore v is even further reduced from the prediction. This suggests that the reported transition from A ($L \propto v^2$) to B ($L \propto v$) states of pure superflow turbulence might be spuriously produced by this effect, hence casting doubts over all conclusions pertaining to steady-state turbulence in Ref. 19.

Precise quantitative conclusions unfortunately cannot be drawn because of the limitations of this direct velocity measurements technique. We stress, however, that the data and discussion of the temporal decay of L in Ref. 19 remains valid, as it is fully independent of knowledge of steady-state flow velocity.

V. CONCLUSIONS

We have presented new measurements of the onset and steady-state turbulence of a net flow of ^{4}He superfluid

component in channels of square cross sections of 7- and 10-mm sides, generated mechanically by a low temperature bellows assembly and detected by the second sound attenuation technique.

The dependence of vortex line density L on mean superflow velocity v from both channels satisfies $L^{1/2} = \gamma(T)(v - v_c)$, and therefore it would seem that this system is formally understood within the framework of Vinen's model for thermal counterflow, which treats superflow as counterflow in the frame of reference of the normal component. The $\gamma(T)$ coefficients indeed agree with previous pure superflows and counterflows in the TII regime (i.e., the regime observed in channels of a large cross section of order unity, and sufficiently high vortex line density). We observed a single turbulence regime across the entire velocity range explored. The onset of turbulence occurs at critical velocities v_c not higher than about 0.2 cm/s, a value that within the experimental resolution is roughly independent of temperature. No hysteresis effects have been observed. However, the critical velocity, when examined in the context of other pure superflow experiments of greatly varying channel width d, is lower than predicted by the law $v_c \sim d^{-1/4}$, which otherwise holds rather generally. This suggests that the normal component, although not flowing past the superleaks, may not be at rest in the channel, therefore triggering turbulence in the superfluid at lower velocities.

This work strengthens what is currently known and understood about fully developed turbulent superfluid channel flows in the temperature range where the interaction between the two velocity fields is important, and also draws attention to the still open and complex problem of transition to turbulence in the two-fluid system. Further characterization of the problem, with more open issues, is provided by the observation of the temporal decay of vortex line density upon suddenly stopping the bellows drive, an aspect which will be discussed in a follow-up article.

ACKNOWLEDGMENTS

The authors greatly acknowledge stimulating discussions with and help from T. V. Chagovets, M. La Mantia, P. Roche, D. Schmoranzer, and W. F. Vinen. This work was supported by Grant No. GAČR 202 08/0276.

APPENDIX: DERIVATION OF AN EXPRESSION TO DEDUCE VORTEX LINE DENSITY FROM SECOND SOUND ATTENUATION

We present here a step-by-step derivation for Eq. (2). The plan is to derive the second sound wave equation from the two-fluid equations of motion; set up the resonant conditions for the flow channel; find an expression for the attenuation by vortex lines of the second sound amplitude; and obtain workable equations for the vortex line density L from assumptions on the spacial distributions of the vortex lines.

Let us start from the set of two-fluid model equations, in the limit of small normal and superfluid velocities $\mathbf{v}_n$ and $\mathbf{v}_s$ and in the presence of the mutual friction force $\mathbf{F}_{ns}$.[23] The following equations are, respectively, the conservation of mass, entropy (σ, per unit mass), and momentum for the superfluid and normal components:

$$\frac{\partial}{\partial t}(\rho_n + \rho_s) = -\nabla \cdot (\rho_n \mathbf{v}_n + \rho_s \mathbf{v}_s), \tag{A1}$$

$$\frac{\partial(\rho\sigma)}{\partial t} = -\nabla \cdot (\rho\sigma \mathbf{v}_n), \tag{A2}$$

$$\rho_s \left(\frac{\partial \mathbf{v}_s}{\partial t} + (\mathbf{v}_s \cdot \nabla)\, \mathbf{v}_s \right) = -\frac{\rho_s}{\rho}\nabla p + \rho_s \sigma \nabla T - \mathbf{F}_{ns}, \tag{A3}$$

$$\rho_n \left(\frac{\partial \mathbf{v}_n}{\partial t} + (\mathbf{v}_n \cdot \nabla)\mathbf{v}_n \right) = -\frac{\rho_n}{\rho}\nabla p - \rho_s \sigma \nabla T + \eta_n \nabla^2 \mathbf{v}_n + \mathbf{F}_{ns}. \tag{A4}$$

Symbols still undefined are the pressure p and the dynamic viscosity of the normal component η_n. The mutual friction force per unit volume is given by[40]

$$\mathbf{F}_{ns} = B\frac{\rho_n \rho_s}{\rho}\hat{\mathbf{\Omega}} \times [\mathbf{\Omega} \times (\mathbf{v}_n - \mathbf{v}_s)] + B'\frac{\rho_n \rho_s}{\rho}\mathbf{\Omega} \times (\mathbf{v}_n - \mathbf{v}_s), \tag{A5}$$

which applies to the case of a cylindrical container of superfluid rotating around the central axis with angular velocity $\mathbf{\Omega}$ (i.e., the case in which the vortex lines are oriented parallel with the axis of rotation). The coefficient B is of order unity; the second nondissipative term in B' is assumed small enough to be neglected.

Since in the uniformly rotating container the full length of vortex lines contributes to the angular velocity (no self-canceling lines oriented in random directions) we can write $\mathbf{L} = 2\mathbf{\Omega}/\kappa$, where the orientation of $\mathbf{L}$ gives the orientation of the lines at a given point. Neglecting the second term, Eq. (A5) reduces to

$$\mathbf{F}_{ns} = -B\kappa\frac{\rho_s \rho_n}{2\rho} L(\mathbf{v}_n - \mathbf{v}_s)\sin^2\theta, \tag{A6}$$

where θ is the angle between $\mathbf{L}$ and $\mathbf{v}_{ns} = \mathbf{v}_n - \mathbf{v}_s$. For the sake of clarity, notice that in this derivation by $\mathbf{v}_{ns}$ we do not mean the main counterflow velocity along the channel direction caused by the bellows, but the counterflow velocity associated with the second sound wave, propagating perpendicular to the channel. The fact that the mutual friction force is proportional to $\sin^2\theta$ is referred to as the "sine squared law".[41]

To proceed, we can neglect the nonlinear terms in velocity on the left-hand side of Eqs. (A3) and (A4) (this is possible because in experiments we work in a regime where the second sound driving amplitude is small enough to prevent generation of turbulence) and we neglect the viscous dissipation in Eq. (A4) (because of the small viscosity of the normal component), then by multiplying Eq. (A3) by ρ_n/ρ_s and subtracting it from Eq. (A4) we obtain

$$\rho_n \frac{\partial \mathbf{v}_{ns}}{\partial t} = -\rho\sigma\nabla T + \frac{\rho}{\rho_s}\mathbf{F}_{ns}. \tag{A7}$$

If we further assume that the counterflow velocity $\mathbf{v}_{ns}$ and derivatives of density and entropy are small, combining Eqs. (A1) and (A2) and neglecting terms nonlinear in small quantities we get

$$\nabla \cdot \mathbf{v}_{ns} = -\frac{\rho}{\sigma\rho_s}\frac{\partial\sigma}{\partial t}. \tag{A8}$$

Now we seek a solution for a second sound traveling wave in the form of small perturbations σ' and T' around constant values of σ_0 and T_0 of entropy and temperature, while leaving pressure and density constant. With these simplifications Eq. (A8) can be written as

$$\nabla \cdot \mathbf{v}_{\rm ns} = -\frac{\rho\sigma}{\rho_{\rm n} c_2^2}\frac{\partial T}{\partial t}, \tag{A9}$$

where

$$c_2 = \sigma\sqrt{\frac{\rho_{\rm s}}{\rho_{\rm n}}\left(\frac{\partial T}{\partial \sigma}\right)_\rho} \tag{A10}$$

is the velocity of second sound. Substituting Eq. (A6) to Eq. (A7) and solving for ∇T leads to

$$\nabla T = -\frac{\rho_{\rm n}}{\sigma\rho}\left(\frac{B\kappa L}{2}(\sin^2\theta)\mathbf{v}_{\rm ns} + \frac{\partial \mathbf{v}_{\rm ns}}{\partial t}\right). \tag{A11}$$

Taking the gradient of Eq. (A9) and interchanging time and space derivatives we obtain

$$\nabla(\nabla\cdot\mathbf{v}_{\rm ns}) = \frac{1}{c_2^2}\left(\frac{B\kappa L}{2}(\sin^2\theta)\frac{\partial \mathbf{v}_{\rm ns}}{\partial t} + \frac{\partial^2 \mathbf{v}_{\rm ns}}{\partial t^2}\right). \tag{A12}$$

We now consider a second sound plane wave traveling along the z direction with angular frequency ω and wave vector $k\mathbf{e}_z$.

$$\mathbf{v}_{\rm ns} = \mathbf{e}_z v_{ns0} e^{i(\omega t - kz)}. \tag{A13}$$

Substituting this to Eq. (A12) we obtain

$$k = \pm\frac{\omega}{c_2}\sqrt{1 - i\frac{B\kappa L}{2\omega}\sin^2\theta}. \tag{A14}$$

The vortex line density measured in experiments usually ranges from 10^4 to 10^6 cm^{-2}, making κL of order of 1–100 Hz. The frequency of second sound used in experiments is of order 1 kHz.

We can therefore usually (see later) limit ourselves with the first two terms of Taylor expansion of the square root, and since only the negative sign solution is physically meaningful we obtain

$$k = -\frac{\omega}{c_2}\left(1 - i\frac{B\kappa L}{4\omega}\sin^2\theta\right). \tag{A15}$$

Substituting this back to Eq. (A13) we get the propagation of an attenuated wave,

$$\mathbf{v}_{\rm ns} = \mathbf{e}_z v_{ns0}\exp\left[i\left(\omega t - \frac{\omega}{c_2}z\right) - \alpha z\right], \tag{A16}$$

where the attenuation constant is

$$\alpha = \frac{B\kappa L}{4c_2}\sin^2\theta. \tag{A17}$$

Now we need to replace $\sin^2\theta$ by its mean value, making an assumption on the spatial distribution of vortex lines. Assuming a homogeneous and isotropic distribution, and choosing a coordinate system so that $\mathbf{v}_{\rm ns}$ always lies along the z axis, we get

$$\langle\sin^2\theta\rangle = \frac{1}{4\pi}\int_0^{2\pi}\int_0^{\pi}(\sin^3\theta)d\theta{\rm d}\phi = \frac{2}{3}, \tag{A18}$$

and thus the attenuation constant for randomly oriented vortex lines is

$$\alpha = \frac{B\kappa L}{6c_2}. \tag{A19}$$

Note that if the tangle were completely polarized in the direction perpendicular to the propagation of second sound, the result in Eq. (A18) would be 1/2. So if the assumption of homogeneity and isotropy were wrong, Eq. (A19) would be at worst a factor 4/3 higher than the true value. The attenuation of the second sound amplitude by mutual friction adds to the ordinary bulk viscous attenuation. To account for this, we decompose the attenuation constant to a part independent of flow, and one given by Eq. (A19):

$$\tilde{\alpha} = \alpha_0 + \alpha. \tag{A20}$$

The attenuation constant is related to the quality factor of a resonator $Q = f_0/\Delta f$ where f_0 is the resonance frequency and Δf is full width at half maximum of resonance the curve, through

$$\tilde{\alpha} = \frac{\pi}{\lambda Q} = \frac{\pi\Delta f}{c_2}, \tag{A21}$$

where λ is the resonant wavelength.

When the second sound is excited at resonant frequency the waves reflected at the receiver will constructively interfere with the waves emitted from the transducer, giving the total measured amplitude,

$$a = a_e\sum_{n=1}^{+\infty}e^{-\tilde{\alpha}D} = \frac{a_e}{e^{\tilde{\alpha}D}-1} \approx \frac{a_e}{\tilde{\alpha}D}, \tag{A22}$$

where D is channel width and a_e is amplitude of the wave excited by the transducer. Using Eqs. (A20) and (A21) we arrive at

$$\alpha = \frac{\pi\Delta f}{c_2}\left(\frac{a_0}{a} - 1\right). \tag{A23}$$

Here a_0 is the amplitude when there is no flow in the channel and a is the amplitude with the flow. Finally, using Eq. (A19) we obtain

$$L = \frac{6\pi\Delta f}{B\kappa}\left(\frac{a_0}{a} - 1\right). \tag{A24}$$

This is the required formula (2) that gives vortex line density as a function of directly measurable quantities.

If further terms in the Taylor expansion of Eq. (A14) are considered one can arrive at the following more exact expression (see also Ref. 9):

$$L' = \frac{3c_2}{B\kappa D}\ln\left(\frac{1 + p^2P + \sqrt{2p^2P + p^4P^2}}{1 + P + \sqrt{2P + P^2}}\right), \tag{A25}$$

where $p = a_0/a$ and $P = 1 - \cos(2\pi D\Delta_0/c_2)$, with $D\Delta_0/c_2$ small. The version of Eq. (A24) becomes an overestimation of the true vortex line density provided by Eq. (A25) at extremely high L. From a practical point of view, there is no need to use L' instead of L as long as $(L - L')/L'$ remains much lower than about 30%, which is the maximum uncertainty in L introduced by not knowing the exact spacial distribution of vortex lines. For our channels with $D = 7$ mm, we find $(L - L')/L' = 30\%$ at $L' \approx 3\times10^7$ cm^{-2}. The maximum L reported in this paper is about 8×10^6, for which $(L - L')/L' \cong 8\%$.

*Department of Physics, ETH Zurich, Schafmattstr. 16, CH-8093 Zürich, Switzerland.

[1]W. F. Vinen and J. J. Niemela, J. Low Temp. Phys. **128**, 167 (2002); L. Skrbek and K. R. Sreenivasan, Phys. Fluids **24**, 011301 (2012).

[2]D. R. Tilley and J. Tilley, *Superfluidity and Superconductivity*, 3rd ed. (Institute of Physics Publishing, Bristol and Philadelphia, 1990).

[3]W. Guo, S. B. Cahn, J. A. Nikkel, W. F. Vinen, and D. N. McKinsey, Phys. Rev. Lett. **105**, 045301 (2010).

[4]W. F. Vinen, Proc. R. Soc. **240**, 114 (1957); **240**, 128 (1957); **242**, 493 (1957); **243**, 400 (1958).

[5]J. T. Tough, in *Progress in Low Temperature Physics*, Vol. VIII (North-Holland, Amsterdam, 1982).

[6]M. R. Smith, R. J. Donnelly, N. Goldenfeld, and W. F. Vinen, Phys. Rev. Lett. **71**, 2583 (1993).

[7]L. Skrbek, A. V. Gordeev, and F. Soukup, Phys. Rev. E **67**, 047302 (2003).

[8]A. V. Gordeev, T. V. Chagovets, F. Soukup, and L. Skrbek, J. Low Temp. Phys. **138**, 549 (2005).

[9]C. F. Barenghi and L. Skrbek, J. Low Temp. Phys. **146**, 5 (2007).

[10]J. Maurer and P. Tabeling, Europhys. Lett. **43**, 29 (1998).

[11]J. Salort, B. Baudet, B. Castaing, F. Chabaud, T. Daviaud, P. Didelot, B. Diribarne, Y. Dubrulle, F. Gagne, A. Gauthier, B. Girard, B. Hebral, B. Rousset, P. Thibault, and P. E. Roche, Phys. Fluids **22**, 125102 (2010).

[12]J. Salort, B. Chabaud, E. Leveque, and P. E. Roche, Europhys. Lett. **97**, 34006 (2012).

[13]S. R. Stalp, L. Skrbek, and R. J. Donnelly, Phys. Rev. Lett. **82**, 4831 (1999).

[14]L. Skrbek, J. J. Niemela, and R. J. Donnelly, Phys. Rev. Lett. **85**, 2973 (2000).

[15]P. M. Walmsley, A. I. Golov, H. E. Hall, W. F. Vinen, and A. A. Levchenko, J. Low Temp. Phys. **153**, 127 (2008); P. M. Walmsley and A. I. Golov, Phys. Rev. Lett. **100**, 245301 (2008).

[16]K. W. Schwarz, Phys. Rev. B **18**, 245 (1978); **31**, 5782 (1985); **38**, 2398 (1988).

[17]R. A. Ashton, L. B. Opatowsky, and J. T. Tough, Phys. Rev. Lett. **46**, 658 (1981).

[18]M. L. Baehr, L. B. Opatowsky, and J. T. Tough, Phys. Rev. Lett. **51**, 2295 (1983).

[19]T. V. Chagovets and L. Skrbek, Phys. Rev. Lett. **100**, 215302 (2008); J. Low Temp. Phys. **153**, 162 (2008).

[20]S. Fuzier, B. Baudouy, and S. W. Van Sciver, Cryogenics **41**, 453 (2001).

[21]To test this assumption, we have forced normal liquid helium (above the lambda transition) against the superleak using the maximum force provided by the motor, 320 N, applied on the bellows effective area of 42.5 cm^2, thereby causing an overpressure in the helium of about 75 kPa. The motor encoder did not measure any displacement during tens of minutes, indicating no measurable viscous flow occurred through the superleak.

[22]On expanding the bellows the flow through the channel faithfully follows the bellows motion only up to a limited, rather low, velocity, due to the small (few Torr, depending on the temperature) overpressure of the helium vapor above the liquid helium in the bath.

[23]C. F. Barenghi and Y. A. Sergeev, *Vortices and Turbulence at Very Low Temperature* (Springer, Wien/New York, 2008).

[24]R. J. Donnelly and C. F. Barenghi, J. Phys. Chem. Ref. Data **27**, 1217 (1998).

[25]C. F. Barenghi, A. V. Gordeev, and L. Skrbek, Phys. Rev. E **74**, 026309 (2006).

[26]Heat transport through helium-filled silver-sintered superleaks can occur via conduction through the silver material and via conduction through the normal component (negligible), since the superfluid cannot carry heat and the viscous normal component cannot convect because it is immobilized in the pores. To estimate heat conduction through the silver itself we used the typical electrical resistivity of silver sinters with $\approx 1/2$ volume packing and purity RRR = 10–20, used for dilution refrigerators, $R \approx 10\ \mu\Omega$cm;[42] we applied the Wiedemann-Franz law to convert electrical resistivity into thermal conductivity (due to electrons, neglecting the lattice contribution) $k_c = \mathcal{L}T/R$, where $\mathcal{L} = 2.44 \times 10^{-8}$ WΩK^{-2} is the Lorenz number. We find $k_c \approx 10^{-2}$ Wcm^{-1}K^{-1}. From the Fourier law for heat conduction we arrive at the power transferred across the superleak $\dot{Q} = k_c A \Delta T/d \approx 10^{-4}$ W, for surface area $A \approx 2$ cm^2 and thickness $d = 0.2$ cm, and for the typical excess temperature in the bellows $\Delta T \approx 1$ mK. Note that this calculated heat input would cause a maximum counterflow velocity in the channel $v_{ns} = v_n - v_s = \dot{Q}/(A\rho_s \sigma T) = 3 \times 10^{-3}$ cm/s,[2] where v_n and v_s are the normal and superfluid velocities, ρ_s is the superfluid density, and σ the entropy per unit mass of helium. Such counterflow velocity is negligible compared with any flow velocity relevant to this experiment, hence the finite thermal conductivity of the superleaks is not an important issue. A similar argument rules out thermal losses through brass walls, even smaller than through superleaks.

[27]K. P. Martin and J. T. Tough, Phys. Rev. B **27**, 2788 (1983).

[28]R. K. Childers and J. T. Tough, Phys. Rev. B **13**, 1040 (1976).

[29]H. Adachi, S. Fujiyama, and M. Tsubota, Phys. Rev. B **81**, 104511 (2010).

[30]D. J. Melotte and C. F. Barenghi, Phys. Rev. Lett. **80**, 4181 (1998).

[31]V. I. Kruglov, Phys. Lett. A **375**, 4058 (2011).

[32]E. F. Hammel and W. E. Keller, Cryogenics **5**, 245 (1965).

[33]W. Vermeer, W. M. Van Alphen, J. F. Olijhoek, K. W. Taconis, and R. De Bruyn Ouboter, Phys. Lett. **18**, 265 (1965).

[34]C. E. Chase, Phys. Rev. **127**, 361 (1962).

[35]P. P. Craig and J. R. Pellam, Phys. Rev. **5**, 1109 (1957).

[36]D. R. Ladner and J. T. Tough, Phys. Rev. B **20**, 2690 (1979).

[37]R. K. Childers and J. T. Tough, Phys. Rev. Lett. **31**, 911 (1973).

[38]E. G. Yarmchuk and W. I. Glaberson, J. Low Temp. Phys. **36**, 381 (1979).

[39]W. M. Van Alphen, G. J. Van Haasteren, R. De Bruyn Ouboter, and K. W. Taconis, Phys. Lett. **20**, 474 (1966).

[40]H. E. Hall and W. F. Vinen, Proc. R. Soc. **238**, 204 (1957); **238**, 215 (1957).

[41]H. A. Snyder and Z. Putney, Phys. Rev. **150**, 110 (1966); P. Mathieu, B. Placais, and Y. Simon, Phys. Rev. B **29**, 2489 (1984).

[42]F. Pobell, *Matter and Methods at Low Temperature*, 3rd ed. (Springer, New York, 2007).

Attachment 2. The Decay of Forced Turbulent Coflow of He II Past a Grid

J Low Temp Phys (2014) 175:324–330
DOI 10.1007/s10909-013-0938-y

The Decay of Forced Turbulent Coflow of He II Past a Grid

S. Babuin · E. Varga · L. Skrbek

Received: 9 July 2013 / Accepted: 30 September 2013 / Published online: 8 October 2013

Abstract We present an experimental study of the decay of He II turbulence created mechanically, by a bellows-induced flow past a stationary grid in a 7×7 mm^2 superfluid wind tunnel. The temporal decay $L(t)$ originating from various steady-states of vortex line length per unit volume, L_0, has been observed based on measurements of the attenuation of second-sound, in the temperature range $1.17\ \text{K} < T < 1.95\ \text{K}$. Each presented decay curve is the average of up to 150 single decay events. We find that, independently of T and L_0, within seconds past the sudden stop of the drive, all the decay curves show a universal behavior lasting up to 200 s, of the form $L(t) \propto (t - t_0)^{-3/2}$, where t_0 is the virtual origin time. From this decay process we deduce the effective kinematic viscosity of turbulent He II. We compare our results with the bench-mark Oregon towed grid experiments and, despite our turbulence being non-homogeneous, find strong similarities.

Keywords Quantum turbulence · Decay · Superfluid ^{4}He · Second-sound · Grid

1 Introduction

We are interested in quantum turbulence (QT) in ^{4}He [1–3] in the temperature range $1\ \text{K} \lesssim T \leq T_\lambda$ where both superfluid and normal components interact and may become turbulent [4]. The turbulence in the superfluid component takes generally the form of a tangle of vortex lines with Å-size cores and total length per unit volume L,

S. Babuin ( )
Institute of Physics ASCR, Na Slovance 2, 182 21 Prague, Czech Republic
e-mail: babuin@fzu.cz

E. Varga · L. Skrbek
Faculty of Mathematics and Physics, Charles University in Prague, Ke Karlovu 3, 121 16 Prague, Czech Republic

along which superfluid vorticity is concentrated and around which superfluid velocity circulation is quantized in units of $\kappa \cong 10^{-3}$ cm^2/s. The nature of turbulence in the normal component is largely unknown; however, it is assumed to obey principles of classical turbulence in incompressible viscous fluids. When quantized vortices are present, the superfluid and normal velocity fields are coupled by the mutual friction force [1, 2]. At small scales of order the mean inter-vortex separation, $\delta = L^{-1/2}$, the two velocity fields must differ, because of quantum mechanical constraints on the superfluid velocity field. At large scales, however, the coupling yields a two-fluid system displaying effectively classical behavior. It is therefore of interest to study the case when both components of He II are forced simultaneously. Here we do so mechanically, by a bellows forcing a flow of both components (coflow) into a superfluid wind tunnel, and observing at a fixed location downstream from a stationary grid the temporal decay of L. This work closely relates to experiments performed in Oregon, where a grid of bars was pulled with steady velocity through a test section of a stationary sample of He II [5–8], and which have become a bench-mark for the current understanding of QT decay [9].

2 Experimental Setup and Method

The flow source [10] is a calibrated low temperature bellows immersed in an open bath cryostat and operated by a computer-controlled motor. It provides flow velocities up to about 1 m/s controlled with 3 % accuracy. The bellows can be stopped within 10 ms, providing a good tool for studying the decay of the vortex tangle.

The flow channel is shown in the inset of Fig. 1. The internal straight section is 10.5 cm long and has a square 7×7 mm^2 profile. The grid is located 14 mm upstream from the center of second-sound sensors intended to sample a fully developed turbulence; these are 9 mm diameter nuclepore disk membranes, nearly flush with the walls. The grid is held in position by a thin frame of wires running along the channel corners and is made of 11 perpendicular stainless steel tines per side, of about 0.1 mm thickness, forming square meshes of about 0.5 mm side. The lower entry of the channel has a flow conditioner in the form of a 18 mm diameter, 10 mm long cylinder packed with a stack of parallel stainless steel tubes of diameter $d = 1$ mm and wall thickness about 0.1 mm. For a typical He II flow velocity $v = 10$ cm/s and effective kinematic viscosity $\nu_{\text{eff}} \approx 10^{-4}$ cm^2/s, the Reynolds number of the flow through the tubes is $Re = vd/\nu \approx 10^4$ i.e. the flow injected is turbulent but with eddies limited in size by d. Larger eddies that might have been created in a curved pipe connecting bellows to channel are filtered out.

The vortex line density, L, is deduced from the attenuation of the second-sound standing wave perpendicular to the mean flow direction. For a homogeneous and isotropic vortex tangle with $L \lesssim 10^7$ cm^{-2}, it was shown that [10]:

$$L(t) = \frac{6\pi\,\Delta f_0}{B\kappa}\left(\frac{A_0}{A(t)} - 1\right), \tag{1}$$

where Δf_0 and A_0 are line-width and amplitude of the second-sound resonant Lorentzian curve for stationary He II, $A(t)$ is the attenuated amplitude in the presence of QT, and B is the mutual friction coefficient [11]. The resonant frequency is

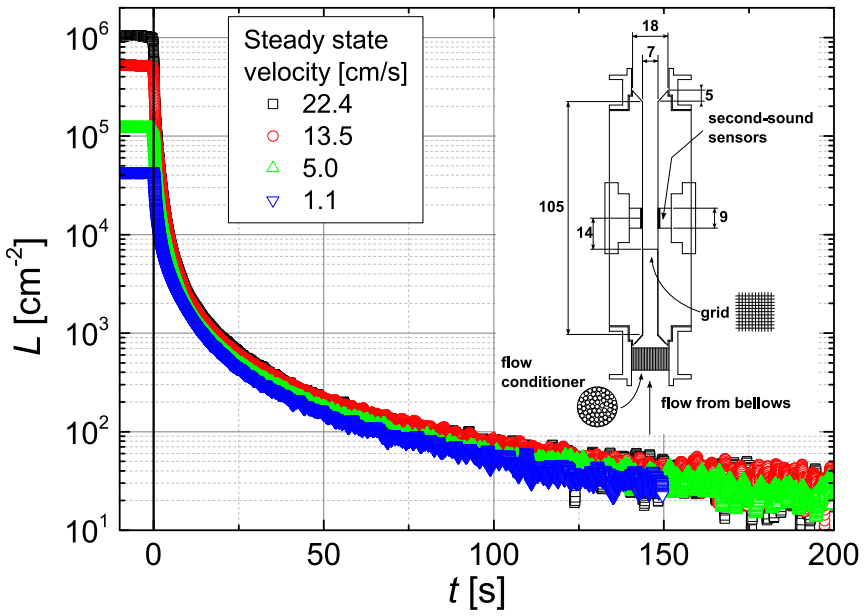

Fig. 1 The total length of quantized vortex lines per unit volume as a function of time, detected by the attenuation of second-sound past the grid. Four different starting line densities are displayed, at $T = 1.45$ K. *Each curve* is the average of 150 decay events. At $t = 0$ the steady flow is suddenly switched off. *Inset*: the flow channel containing the grid; He II flows from *bottom* to *top* (Color figure online)

not significantly altered by the presence of QT. $A(t)$ is sampled at 60 Hz by a lock-in amplifier operating with 10 ms time constant. The second-sound resonator can detect changes in L with a time resolution $\Delta f^{-1} \approx 10$ ms at the beginning and for most of the decay duration, except towards the end when the stationary amplitude recovers and $\Delta f^{-1} \approx 100$ ms. The temperature of the bath is maintained stable to ≈ 0.1 mK during measurements. As the same stability level is measured inside the bellows, we assume the same also inside the channel.

3 Results and Discussion

Figure 1 displays four decays measured at $T = 1.45$ K originating from different steady-state vortex line density, L_0, corresponding to the velocities indicated in the legend (the measured critical velocity for turbulence onset is ≈0.1 cm/s). Each curve is the result of averaging about 150 decay events. The steady flow lasted for ≈30 s, assuring the turbulence is in steady-state.

In Fig. 2 we zoom-up the first 4 s of the same decays. To compare, we show in the inset a decay from an earlier pure superflow experiment performed with the same apparatus and channel, but where superleak plugs at the channel ends allowed net through-flow of the superfluid component only and the channel had no grid. The superflow decay has the same T and L_0 of the lowest density coflow decay, but it is substantially faster at the onset. To qualify this we have plotted as a solid line the decay solution of the Vinen equation for counterflow turbulence [12], $L(t) = (1/L_0 + 2\pi\chi_2 t/\kappa)^{-1}$, where for χ_2 we have used standard values [1]. The pure superflow, which as far as steady-state properties can approximately be understood as counterflow in the frame of reference of the normal component [10],

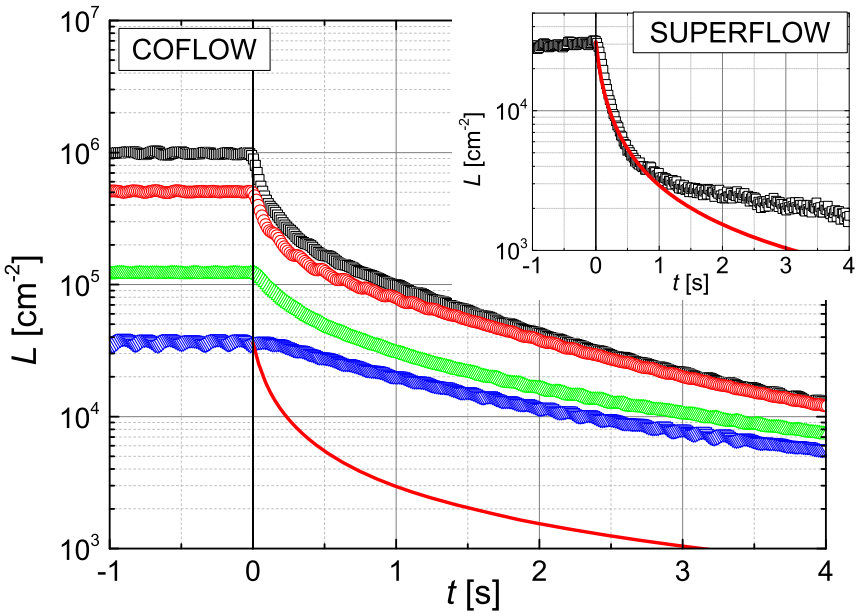

Fig. 2 A detail of the first 4 s of the decay process shown in Fig. 1. *Inset*: comparison with an experiment in the same flow channel where superleak plugs allowed a net flow of the superfluid component of He II only. The superflow decay and the lowest coflow decay originate from the same L_0, but display very different initial decay behavior. The *solid line* is the solution of the Vinen equation for counterflow decay, $L(t) = (1/L_0 + 2\pi\chi_2 t/\kappa)^{-1}$ (Color figure online)

obeys this prediction for the first 1 s, whilst the coflow decay is distinctly different in character. The pure superflow decay too departs from the counterflow prediction at later times, or (not shown here) if L_0 is increased, but this will be the subject of another study. The considerably slower decay of the coflow relative to pure superflow may partly be due to a greater degree of randomization of the tangle in the superflow, and due to the fact that the grid introduces an inhomogeneity along the flow direction, since the vortex lines are presumably denser near the grid then further downstream. This gradient in L would cause the tangle to spatially diffuse past the sensor, as well as decaying in time, a process which might alter the decay rate and would not occur in the absence of the grid in the pure superflow experiment.

We now turn to the main focus of this article, the decay at later times. In Fig. 3 we re-plot the data from Fig. 1 in log-log coordinates, using the adjusted quantities $L^* = L - L_r$ and $t^* = t - t_0$, where L_r and t_0 are respectively the remanent value of L persisting at $t \to \infty$ (of order 10 cm^{-2}) and the virtual time origin, for a decay process of the form $L(t) = A(t - t_0)^{-3/2} + L_r$. L_r and t_0 are determined by fitting the latter equation to the curves in Fig. 1, starting the fit at $L \approx 0.2L_0$, where L_0 is the initial density, to avoid the initial transients where the decay is not yet of $t^{-3/2}$ form. The dependence of t_0 on L_0 and T is shown inset in Fig. 4.

From Fig. 3 we learn that decays starting from different L_0 eventually collapse into a universal decay behavior of the form $L^* \propto t^{*-3/2}$. This is confirmed by the inset, where the compensated quantity $L^* t^{3/2}$ is plotted showing a constant value beginning at $t \approx 10$ s and lasting up to 200 s. The use of t in place of t^* in the inset prevents distorsions of the initial transients, but it worsens the collapse between parallel lines at later times, compared to the main plot. In the inset, for $t \lesssim 10$ s we note deviations from the constant value, indicating the existence of different decay

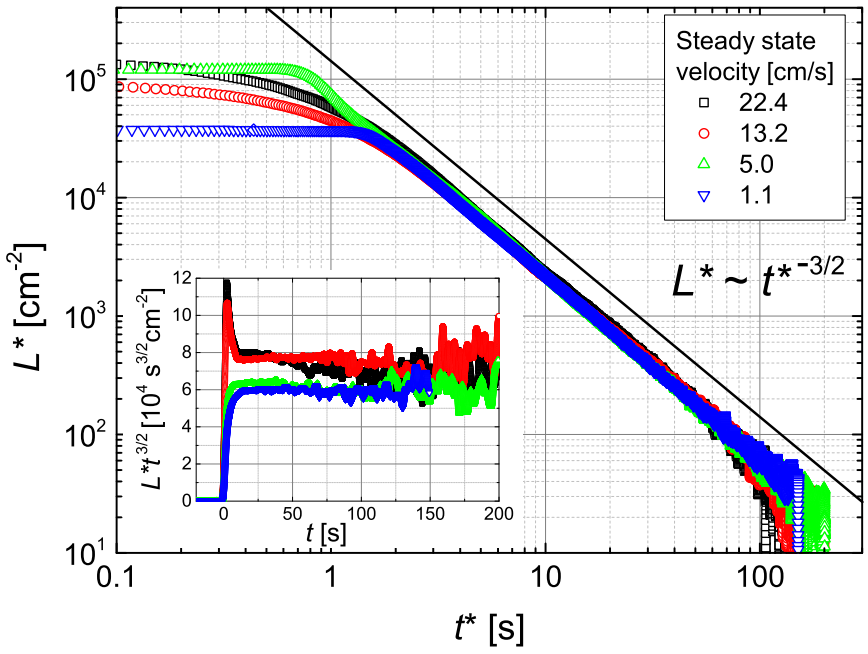

Fig. 3 The decays from Fig. 1 plotted here in log-log coordinates, with $L^* = L - L_r$ and $t^* = t - t_0$, where L_r and t_0 are the remanent vortex line density and the virtual time origin of a decay process of the form $L(t) = A(t - t_0)^{-3/2} + L_r$. *Inset*: the quantity $L^* t^{3/2}$ confirms that after an initial transient of about 10 s, a decay with power law exponent $-3/2$ persists up to 200 s (Color figure online)

regimes that might be characterized by different power exponents. For the two higher L_0 curves a peak is produced because the asymptote of the $t^{-3/2}$ power law is located at $t_0 > 0$, as shown in Fig. 4. Decays at other temperatures are similar to those shown here at $T = 1.45$ K.

The universal behavior $L \propto t^{-3/2}$ observed here is in agreement with the Oregon towed grid experiments [6–8]. Those were understood [9, 13] based on the following assumptions: (i) the turbulence is homogeneous and isotropic; (ii) the kinetic energy per unit mass is imputed at rate ε at scales of order the grid mesh size where quasi-classical eddies of coupled superfluid and normal components are present; (iii) the energy Richardson-cascades to smaller length scales within the inertial quasi-classical range of the 3D energy spectrum of the Kolmogorov K41 form $\phi = C\varepsilon^{2/3}k^{-5/3}$ (with $C \approx 1.5$) which is terminated by dissipation at scales of order δ. Assuming further [14] that (iv) $\varepsilon = \nu_{\text{eff}}(\kappa L)^2$, where ν_{eff} is the effective kinematic viscosity of He II, and that (v) the energy containing eddies grow during the initial stages of the decay, reaching the channel size D and remaining constant for the rest of the decay, it was shown that at late times:

$$L(t) = \frac{D(3C)^{3/2}}{2\pi\kappa\nu_{\text{eff}}^{1/2}} t^{-3/2}. \tag{2}$$

It is interesting to note that the same scaling is observed in the present work, although we have evidence that the turbulence is non-homogeneous across the channel width. This is deduced from the observation that in steady-state the second harmonic of the second-sound standing wave (nodes near the sensors and at the center) detects about 1.3 times larger L than the first harmonic (nodes near the sensors only), used for the

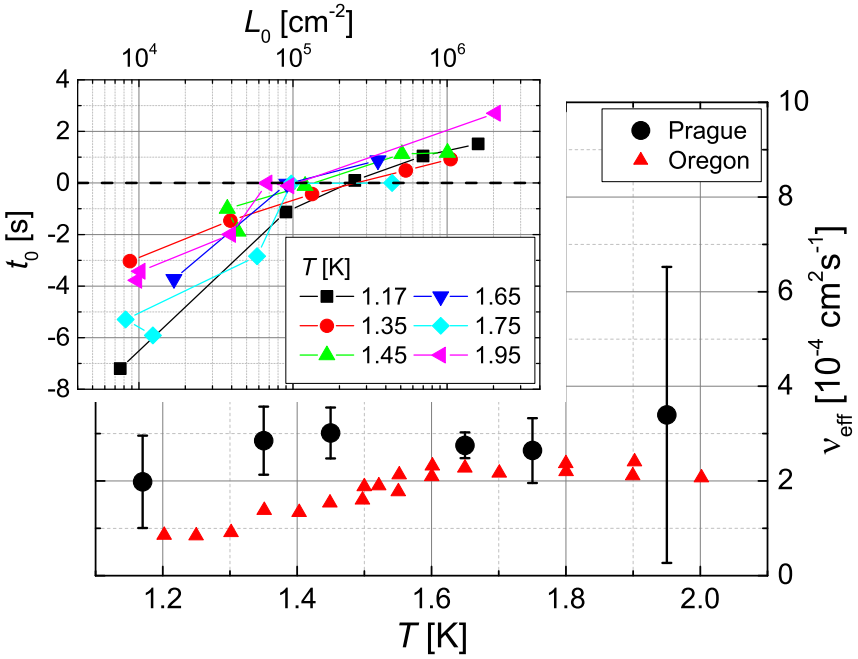

Fig. 4 The effective kinematic viscosity of He II deduced from the prefactor A of the $L^* = At^{*-3/2}$ decay process, as explained in the text, compared to the Oregon results [8]. *Inset*: the virtual time origin of the $t^{-3/2}$ decay as a function of initial line density and temperature (Color figure online)

presented decay measurements. This suggests that the tangle is denser away from the center. The fact that the decay remains of $L \propto t^{-3/2}$ form as in the supposedly more homogeneous Oregon towed grid turbulence, reinforces the notion [9, 13, 15, 16] that assuming homogeneity and Kolmogorov spectrum is not essential in deriving the scaling in Eq. (2). The reduced assumption that large eddies of velocity U and turnover time D/U satisfy $\varepsilon = U^3/D$ leads to the same scaling of Eq. (2), but with prefactor $2D/(\kappa \nu_{\rm eff}^{1/2})$, 31 % higher [9, 16].

In Fig. 4 we plot $\nu_{\rm eff}(T)$ calculated by fitting Eq. (2) to the data in Fig. 3, for comparison with the Oregon experiments [8], although the lack of homogeneity does not fully justify this. Our values are similar, but proper comparison is difficult for lack of error bars on the Oregon data. In general, the Prague values are slightly higher, from 1.1 to 2.1 times, with slightly different T dependence. In fact both sets are subjected to downward correction. (i) L from Oregon has been computed from an underestimation of L seen by second-sound [17] which leads to an overestimation of $\nu_{\rm eff}$ by a factor $\approx$1.4. (ii) Assuming for the Prague data a better estimation for L based on the mean density sampled by first and second harmonics, then $\nu_{\rm eff}$ would have to be reduced by a factor $\approx$1.3. Thus overall, the ratio would not change significantly. At any rate, due to lack of knowledge about the vortex tangle distribution, errors of order 30 % on L are intrinsic, and therefore disagreements in $\nu_{\rm eff} \propto L^{-2}$ up to 60 % might be expected.

4 Conclusions

To conclude, we have presented measurements of the decay of a turbulent He II coflow past a stationary grid in a superfluid wind tunnel, with the flow being forced

mechanically by a bellows, and detected by the attenuation of second-sound. We have found that independently of temperature and starting vortex line density, all decays enter within seconds a universal decay regime of the form $L \propto t^{-3/2}$ lasting for up to 200 s. This is in agreement with the bench-mark Oregon towed grid experiments [6–9], despite our flow being probably less homogeneous than that due to the towed grid. This type of decay is consistent with conceiving He II as a coupled two-fluid system with eddies up to the size of the channel and effective classical behavior. With this assumption, we have extracted the effective kinematic viscosity of He II, and found it in reasonable agreement with the Oregon towed grid data.

Acknowledgements We acknowledge the valuable help of M. Rotter and J. Šebek with the development of cryostat, flow source, and thermometry; of L. Doležal for the construction of grid and flow conditioner; and of F. Soukup for instrumentation. We also thank J. Boháč and P. Vacek for smooth supply of liquid helium. We acknowledge financial support of Charles University in Prague under GAUK No 366213 and SVV-2013-267303.

References

1. W.F. Vinen, J.J. Niemela, J. Low Temp. Phys. **128**, 167 (2002)
2. L. Skrbek, K.R. Sreenivasan, Phys. Fluids **24**, 011301 (2012)
3. S.K. Nemirovskii, Phys. Rep. **524**, 85 (2013)
4. W. Guo, S.B. Cahn, J.A. Nikkel, W.F. Vinen, D.N. McKinsey, Phys. Rev. Lett. **105**, 045301 (2010)
5. M. Smith, R.J. Donnelly, N. Goldenfeld, W.F. Vinen, Phys. Rev. Lett. **71**, 2583 (1993)
6. S. Stalp, L. Skrbek, R. Donnelly, Phys. Rev. Lett. **82**, 4831 (1999)
7. L. Skrbek, J.J. Niemela, R. Donnelly, Phys. Rev. Lett. **85**, 2973 (2000)
8. J.J. Niemela, K.R. Sreenivasan, R.J. Donnelly, J. Low Temp. Phys. **138**, 534 (2005)
9. L. Skrbek, K.R. Sreenivasan, How similar is quantum turbulence to classical turbulence? in *Ten Chapters in Turbulence*, ed. by P.A. Davidson, Y. Kaneda, K.R. Sreenivasan (Cambridge University Press, Cambridge, 2013)
10. S. Babuin, M. Stammeier, E. Varga, M. Rotter, L. Skrbek, Phys. Rev. B **86**, 134515 (2012)
11. R.J. Donnelly, C.F. Barenghi, J. Phys. Chem. Ref. Data **27**, 1217 (1998)
12. W.F. Vinen, Proc. R. Soc. **242**, 493 (1957)
13. L. Skrbek, S. Stalp, Phys. Fluids **12**, 1997 (2000)
14. W.F. Vinen, Phys. Rev. B **61**, 1410 (2000)
15. A.I. Golov, P.M. Walmsley, J. Low Temp. Phys. **156**, 51 (2009)
16. W.F. Vinen, J. Low Temp. Phys. **161**, 419 (2010)
17. T.V. Chagovets, A.V. Gordeev, L. Skrbek, Phys. Rev. E **76**, 027301 (2007)

Attachment 3. Effective viscosity in quantum turbulence: a steady-state approach

Effective viscosity in quantum turbulence: a steady-state approach

Simone Babuin[1], Emil Varga[2], Ladislav Skrbek[2], Emmanuel Lévêque[3,4] and Philippe-E. Roche[5,6]

[1] *Institute of Physics ASCR, Na Slovance 2, 182 21 Prague, Czech Republic*
[2] *Faculty of Mathematics and Physics, Charles University in Prague, Ke Karlovu 3, 121 16 Prague, Czech Republic*
[3] *Laboratoire de Physique, Ecole Normale Supérieure de Lyon & CNRS, Université de Lyon, 46 allée d'Italie, F-69364 Lyon cedex 7, France*
[4] *Laboratoire de Mécanique des Fluides et d'Acoustique, Ecole Centrale de Lyon & CNRS, Université de Lyon, 36 avenue Guy de Collonge F-69134, Ecully, France*
[5] *Univ. Grenoble Alpes, Inst NEEL, F-38042 Grenoble, France, EU*
[6] *CNRS, Inst NEEL, F-38042 Grenoble, France, EU*

PACS 47.37.+q – Hydrodynamic aspects of superfluidity; quantum fluids
PACS 67.57.De – Superflow and hydrodynamics
PACS 67.40.Vs – Vortices and turbulence

Abstract. - The concept of "effective viscosity" ν_{eff} of superfluid helium, widely used to interpret decaying turbulence, is tested in the steady-state case. We deduce ν_{eff} from measurements of vortex line density, $\mathcal{L}$, in a grid flow. The scaling of $\mathcal{L}$ with velocity confirms the validity of the heuristic relation defining ν_{eff}, $\epsilon = \nu_{\text{eff}} (\kappa\mathcal{L})^2$, where ϵ is the energy dissipation rate and κ the circulation quantum. Within $1.17 - 2.16\,\text{K}$, ν_{eff} is consistent with that from decays, allowing for uncertainties in flow parameters. Numerical simulations of the two-fluid equations yield a second estimation of ν_{eff} within an order of magnitude with all experiments. Its temperature dependence, more pronounced in numerics than experiments, shows a cross-over from a viscous-dominated to a mutual-friction-based dissipation as temperature decreases, supporting the idea that the effective viscosity of a quantum turbulent flow is an indicator of the dissipative mechanisms at play.

Introduction. – Quantum turbulence (QT) is the turbulent state of a superfluid [1–3], a fluid with quantum mechanical effects at macroscopic scale. Here we focus on He-II, the superfluid phase of liquid ^{4}He occurring below a transition temperature $T_\lambda \approx 2.18$ K. According to Landau and Tisza's two-fluid-model, He-II can be viewed as a mixture of a normal component which is viscous and entropic and a superfluid component which is inviscid and entropy-free. When He-II is stirred, the normal component supports a vorticity field as in a classical fluid while the situation for the superfluid is unique. Since the superfluid velocity is proportional to the phase gradient of a macroscopic wave function, all its vorticity is concentrated along Å-thick vortex filaments with quantized velocity circulation. The classical limit of macroscopic superfluid rotation can be recovered thanks to the partial polarisation of large number of such quantized vortices. Their presence allows exchange of momentum between the normal and superfluid components. In co-flow turbulent He-II (when both components are forced simultaneously by mechanical means), this coupling is so efficient that both superfluid and normal fluid are locked at large scales of the flow [1,2], but what happens at intermediate and microscopic scales is an active field of research.

Over the last decades, the experimental exploration of ^{4}He QT followed two independent approaches, based either on steady-state or on temporal decay. In the steady-state approach, measured quantities are often compared to their well-established counterparts in classical turbulence: examples are the pressure drop along pipes [4] and velocity spectra [5]. In the decay approach, a model has been widely used to analyse measurements and determine an "effective (kinematic) viscosity" ν_{eff} of He-II from $\simeq 100\,\text{mK}$ up to nearly T_λ [6–9][1]. To the best of our knowledge this concept of "effective viscosity" has never

[1] For an alternative model of decay, see [3, 10]

been transposed to steady-state QT. The motivation of this work is to revisit and test this concept for such flows, by experimental and numerical means.

It is useful to recall here the definition of $\nu_{\rm eff}$. To interpret the time dependence of the mean vortex line density $\mathcal{L}(t) \sim t^{-3/2}$ observed in decaying QT experiments [11], a proportionality relation has been assumed between $\mathcal{L}^2$ and the decay rate $\epsilon \equiv -dE/dt$ of the kinetic energy per unit mass [11–14]:

$$\epsilon = \nu_{\rm eff} \left(\kappa \mathcal{L}\right)^2 , \tag{1}$$

where $\kappa \simeq 10^{-7}$ m^2/s is the quantum of circulation of superfluid ^{4}He. Eq. (1) lacks a rigorous theoretical justification and was motivated by analogy with the classical turbulence equation, $\epsilon = \nu \langle \omega^2 \rangle$, linking dissipation with viscosity, ν, and vorticity, ω. When complemented with additional hypothesis discussed later, Eq. (1) has proven operational reliability in various flows undergoing turbulence decay [9]. Continuing this analogy with classical turbulence, it is interesting to recast Eq. (1) by defining the superfluid Reynolds number:

$$Re_\kappa \equiv \frac{\epsilon^{1/3} H^{4/3}}{\kappa} \equiv \frac{vH}{\kappa} , \tag{2}$$

where v and H are characteristic velocity and length scales of the flow: v is defined as the root mean square (rms) of velocity fluctuations[2], and H, representing the typical large scale of the flow, is defined as

$$H \equiv v^3/\epsilon. \tag{3}$$

In classical homogeneous isotropic turbulence, $H \simeq 2L_{11} \simeq 4L_{22}$, where L_{11} and L_{22} are the longitudinal and transverse integral scales of the flow defined from the autocorrelation function of longitudinal or transverse velocity fluctuations [15]. Introducing the mean inter-vortex spacing $\delta \equiv \mathcal{L}^{-1/2}$, Eq. (1) becomes:

$$\frac{\delta}{H} = \left(\frac{\nu_{\rm eff}}{\kappa}\right)^{1/4} Re_\kappa^{-3/4} . \tag{4}$$

This equation is equivalent to the heuristic relation (1), but turns out to be more convenient to analyze steady-state QT. As pointed out in Ref. [16], Eq. (4) is reminiscent of the equation in classical turbulence relating the Kolmogorov's viscous scale η to the integral scale: $\eta/H \simeq Re^{-3/4}$, where Re is defined as Re_κ after substitution of the kinematic viscosity for κ. Interestingly, the prefactor $\nu_{\rm eff}/\kappa$ can be seen as the effective "Schmidt number" of He-II, accounting for the ratio of a viscous dissipative process and vortex diffusivity process.

We next present a systematic experimental test of Eq. (1) over 8 orders of magnitude. The explored temperature range $1.17\,{\rm K} \leq T \leq 2.16\,{\rm K}$ generalizes the only previous experimental determination restricted around 1.55 K [16]. We then present and discuss our numerical simulations over the same temperature range.

[2]In co-flow He-II QT, as in classical turbulence, most kinetic energy resides at large scales where both components are locked, thus v is defined as the common velocity fluctuation of the two components, $v = v_n = v_s$ along an arbitrary direction.

The experiment. – The steady-flow is a mechanically forced turbulent He-II co-flow through a square cross-section channel, illustrated with dimensions in the insert of Fig. 1. It is installed vertically next to a stainless steel bellows (shown in Ref. [17]) in a liquid ^{4}He bath. The bellows is operated by a computer-controlled motor and can produce flow velocities constant to within 3%. According to the thermometers in the bath and inside the bellows, the helium temperature is maintained constant to within 0.1 mK. The lower entry of the channel has a flow conditioner made by 10 mm long capillaries of 1 mm diameter, cutting larger scale turbulent eddies. In one experiment a grid has been added to the channel, with square openings 0.5 mm wide and tine size 0.1 mm.

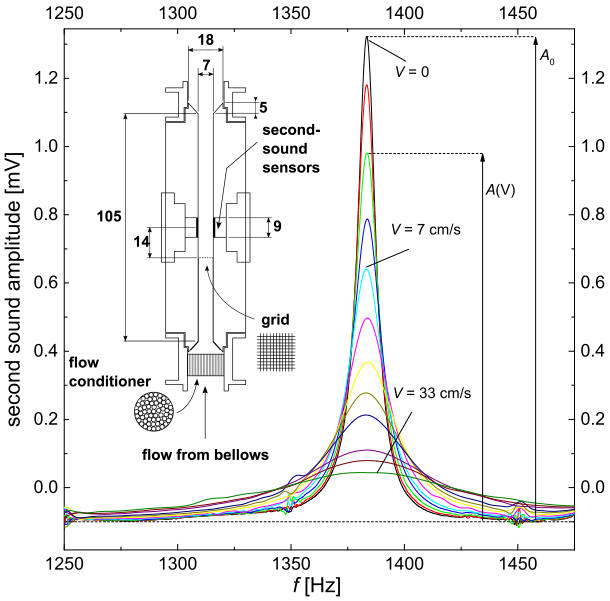

Fig. 1: Second-sound resonances for flows of different mean velocities, past the grid, at $T = 1.65$ K. The amplitude reduction relative to the $V = 0$ case enters the calculation of the vortex line density, $\mathcal{L}$. Inset: flow channel (units are mm). The flow is driven at constant velocity by a bellows.

QT is detected by the second-sound attenuation technique [17]. Quantized vortex lines scatter thermal excitations composing the normal component of He-II, thereby attenuating second-sound – here its standing wave resonance perpendicular to the mean flow direction is modified compared to quiescent helium (see Fig. 1), allowing to deduce the density of quantized vortex lines, $\mathcal{L}$. Assuming a homogeneous and isotropic tangle with $\mathcal{L} \lesssim 10^7$ cm^{-2}, then $\mathcal{L}$ can be estimated as [17]

$$\mathcal{L}(V) = \frac{6\pi \Delta f_0}{B\kappa} \left(\frac{A_0}{A(V)} - 1 \right) , \tag{5}$$

where Δf_0 and A_0 are the width and the amplitude of the

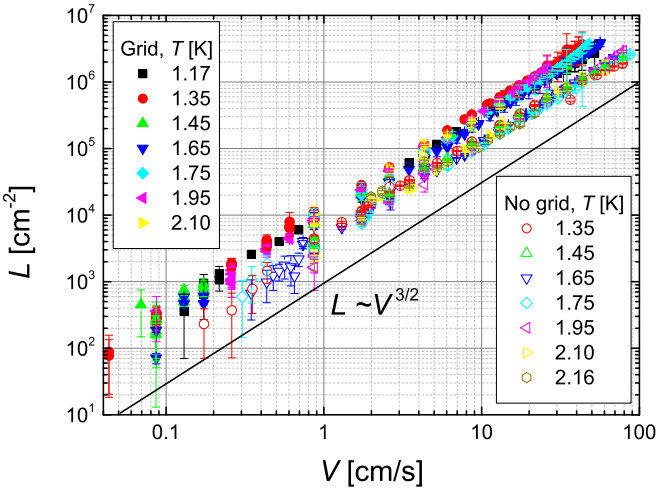

Fig. 2: The measured vortex line density as a function of mean flow velocity for the experiments with and without grid. Four decades of $\mathcal{L}$ exhibit a $V^{3/2}$ scaling, without appreciable temperature dependence, despite varying ρ_s/ρ_n from 45 to 0.1.

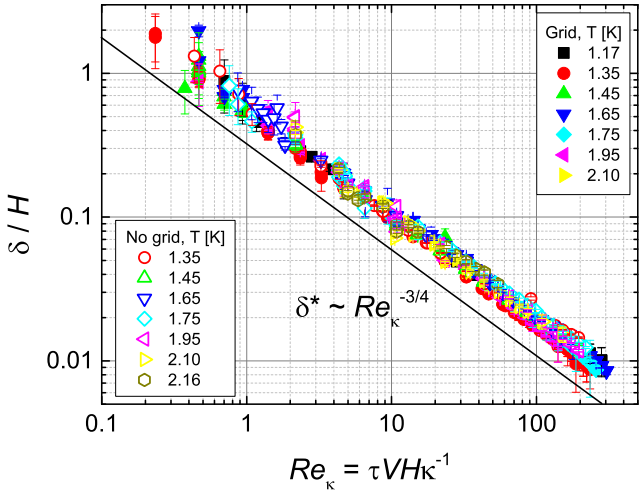

Fig. 3: Data from Fig. 2 presented as dimensionless inter-vortex spacing vs superfluid Reynolds number. The small scale of QT scales with large scale Reynolds number in analogy to viscous dissipation scale in classical turbulence. Fourteen grid and no-grid datasets collapse with an appropriate choice of the large scale of the flow, H, and turbulence intensity, τ.

resonant second-sound curve for quiescent helium, whilst $A(V)$ is the attenuated amplitude for flow velocity V; B is the mutual friction coefficient.

Experimental results. – Fig. 2 represents the primary experimental result of this paper, showing the vortex line density $\mathcal{L}$ as a function of mean flow velocity V. The data display a robust power law of the form $\mathcal{L} \propto V^{3/2}$, over about 4 orders of magnitude in $\mathcal{L}$, holding true upon changing ρ_s/ρ_n from 45 to 0.1. The presence of the grid does not change the scaling but produces about twice $\mathcal{L}$ at all velocities.

The data in Fig. 2 are replotted in Fig. 3 with coordinates δ/H versus $Re_\kappa = \tau V H/\kappa$, as suggested by Eq. (4), with $\tau = \sqrt{\langle v^2 \rangle}/V$ being the turbulence intensity. In this experiment H and τ cannot be measured directly, and are therefore treated as adjustable parameters. We make a choice of H and τ to collapse the data in Fig. 3, with the additional assumption that these parameters do not depend on Re_κ. This procedure yields H and τ consistent with typical values from classical and QT grid turbulence. We stress however that we cannot independently and directly verify the independence on Re_κ, nor the exact nature of the turbulence in the probed region, which in general would be a mix of grid and channel turbulence. In the case of flow without grid, we obtain $H = 1\,\mathrm{mm}/2 = 0.5\,\mathrm{mm}$ (1 mm is the flow conditioner capillary diameter, $2 \sim \sqrt{s_{in}/s_{out}}$ is the channel contraction estimated from cross-sections ratio [20]) and $\tau = 5\%$, a typical value for grid turbulence. In the case with grid, we obtain $H = 0.6\,\mathrm{mm}$ (mesh size) and $\tau = 9\%$, an reasonable value for turbulence in the probed region which spans from 16 to 31 mesh sizes behind the grid. At 31 meshes, $\tau \simeq 4\%$ is expected [20] while τ is expected to be more typical of jet turbulence ($\tau = 25\%$) a few mesh-sizes behind the grid[3]. With this choice of τ and H we obtain a collapse of our fourteen grid and no-grid datasets in Fig. 3 and Eq. (4) suggests that, in the explored temperature range, $\nu_{\mathrm{eff}}/\kappa$ is roughly constant.

Numerical simulations. – To estimate the effective viscosity from simulations, the numerical model should account consistently for the dominant dissipative processes in our steady turbulent flow: the viscosity of the normal component and the dissipative energy exchange between the normal and superfluid components. At present, only the so-called continuous model (where the details of individual vortices are smoothed out) has demonstrated such capacity [21]. We solve those equations in a cubic domain with periodic boundary conditions in the three directions. Accounting for this periodicity, the equations are integrated in the Fourier domain up to a truncating wavenumber $k_{\max} \equiv \pi/\delta_{\min}$, where the resolution $\delta_{\min}$ is of the order of the mean vortex line spacing δ. In order to avoid arbitrariness, the ratio $r = \delta_{\min}/\delta$ is kept as a free parameter (close to unity). The inter-vortex spacing δ is

$$\kappa.\delta^{-2} = \kappa.\mathcal{L} = \sqrt{\langle |\omega_s|^2 \rangle}, \qquad (6)$$

where brackets denote a space average and ω_s is the (macroscopic) superfluid vorticity. Let us notice that the second equality in Eq. (6) does not account for a possible fraction of excitations along individual vortices at scales

[3] Alternative estimations of H consistent in magnitude are from (a) the downstream growth of the classical integral length scale in grid turbulence [20]; (b) analogy with the towed grid He-II experiment [12] which yielded the time at which H is assumed to reach the channel width. In steady flow, this time translates into a ≈ 20 cm downstream distance (120 mesh units), suggesting that H is still significantly smaller than the channel width at our probe location.

smaller than δ, which would contribute to $\mathcal{L}$ but not to ω_s. Such excitations, continuously generated by vortex reconnections, are efficiently damped above 1 K compared to random excitations larger that δ [22] and are therefore expected to represent a small correction absorbed into the free parameter r. The mutual friction force per unit volume between the superfluid and the normal fluid is approximated at first order by $\mathbf{F} = \pm\frac{B}{2}\frac{\rho_n\rho_s}{\rho}|\omega_s|\,(\mathbf{v_s}-\mathbf{v_n})$. Further details about this model, and a physical justification of its relevance above 1 K, are provided in Ref. [16].

Present simulations extend [16] by accounting for possible variations of the scale ratio r, the temperature dependence of the mutual friction parameter B and the normal fluid viscosity μ. The effective viscosity, defined by Eq. (1), is directly computed from the rate of energy injection by $\nu_{\rm eff} = \epsilon/\langle|\omega_s|^2\rangle$, without the need to compute τ and H.

A random forcing is applied at low wavenumbers on both fluid components (in proportion to their relative densities) in such a way that the total rate of energy injection ϵ remains constant over time. A pseudo-spectral method [23] is used for spatial discretization with resolution 512^3 (1024^3 at the lowest temperature). The solution is advanced in time using the second-order Adams-Bashforth scheme. Validation tests have been performed to check that $\nu_{\rm eff}$ is not significantly affected by a threefold change of Re_κ. Calculations are performed at eight temperatures between 1.19 and 2.16 K, for values of the scale ratio $r \simeq 0.6$, 1.2 and 2.4 $\pm 20\%$ (for each temperature) and within $533 \lesssim Re_\kappa \lesssim 1719$.

The calculated effective viscosities are shown in Fig. 4. At high temperature, $\nu_{\rm eff}$ approaches the kinematic viscosity μ/ρ (orange line) irrespective of r. In particular, we note a sharp increase of $\nu_{\rm eff}$ between 2 and 2.16 K. This is consistent with the expectation that at high temperature the two-fluid dynamics becomes governed by the normal component, which itself follows the classical result $\epsilon = \mu/\rho\langle|\omega_n|^2\rangle$. Indeed, the strong mutual friction between the two components then entails:

$$\nu_{\rm eff} = \frac{\epsilon}{\langle|\omega_s|^2\rangle} \simeq \frac{\epsilon}{\langle|\omega_n|^2\rangle} \simeq \mu/\rho. \qquad (7)$$

At lower temperature, $\nu_{\rm eff}$ is found to depart from the kinematic viscosity μ/ρ and some dependence with the adjustable parameter r appears. For $r \simeq 2.4$ and $T \simeq 1.19$ K, where $\rho_s/\rho_n = 40$, $\nu_{\rm eff}$ is typically one decade smaller than in the high temperature limit. To interpret this we consider that in the limiting case of a random vortex tangle moving in a quiescent normal component: it is straightforward[4] to derive the energy dissipation rate (per unit mass) from the friction of a vortex against the normal component: $\epsilon = (\rho_s\rho_n/\rho^2)(B/2)\kappa\,(\kappa\mathcal{L})^2$. This asymptotic model of pure mutual-friction dissipation leads to:

$$\nu_{\rm eff} = \frac{\epsilon}{(\kappa\mathcal{L})^2} = \frac{\rho_s\rho_n}{\rho^2}\frac{B}{2}\kappa\ , \qquad (8)$$

[4]E.g. from Eq. (62) in [1] where $2\alpha\rho = B\rho_n$ and taking $v_L \simeq \kappa/\delta$.

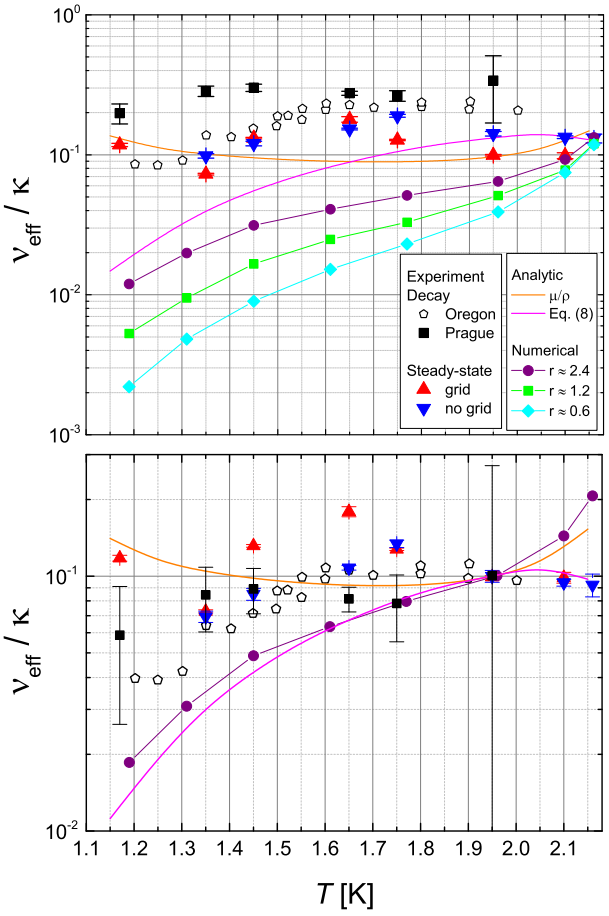

Fig. 4: (top) Dimensionless effective kinematic viscosity versus temperature. Experimental data from decay and present steady-state experiments are shown, as well as the present simulations and analytic models. The Prague decay data was measured in the same grid experiment which yielded the steady-state values of $\nu_{\rm eff}$. The numerical simulations are for three values of the scale ratio r. The solid lines represent analytic models of viscosity discussed in the text. (bottom) The data from the top panel are shown here with an offset along the y-axis so that $\nu_{\rm eff}/\kappa = 0.1$ at $T \simeq 1.96$ K for all datasets. Since the absolute value of $\nu_{\rm eff}$ is subject to uncertainties discussed in the text, this plot focusses on the temperature dependence.

shown in Fig. 4 as a solid magenta line. The temperature dependence of Eq. (8) on the low temperature side is found in good agreement with the numerical simulation data, suggesting that mutual friction, contributes significantly to dissipation below ≈ 1.5 K. The simple analytical models shows that the temperature dependence of $\nu_{\rm eff}$ found in numerical simulations can therefore be interpreted calling in a viscous dissipation process at high temperature, gradually supplemented by a mutual-friction dissipation process at lower temperature[5].

[5]Below 1 K, alternative dissipation mechanisms are expected to become relevant (e.g. see review in [10]).

Discussion on the validity of the heuristic equation $\epsilon = \nu_{\rm eff}\,(\kappa\mathcal{L})^2$. – As mentioned above, Eq. (1) is often assumed in order to interpret the temporal decay of $\mathcal{L}(t)$ in QT experiments, however, the interpretation also relies on additional hypothesis, the key one being that H grows in the early stages of the decay, till it saturates due to finite container size and remains constant at later times [9]. Assuming that the saturation of H is verified, it is straightforward to derive a late decay law from Eqs. (1) and (3):

$$\kappa\mathcal{L}(t) = \frac{H}{\sqrt{\nu_{\rm eff}}} \cdot t^{-3/2}. \tag{9}$$

Proportionality between $\mathcal{L}(t)$ and $t^{-3/2}$ has been reported in a number of experiments. This tends to support the validity of Eq. (1), but it cannot be considered as a direct evidence, due to the additional hypothesis on the saturation of H. For instance, another decay scenario has been proposed to interpret the $\mathcal{L}(t)$ dependence without resorting to Eq. (1), and simply assuming that the decrease of $\mathcal{L}(t)$ results from a diffusion process of the vortex tangle [3, 10] (note however arguments against it in Ref. [2]).

Steady-state studies are able to provide a direct test of proportionality between ϵ and $\mathcal{L}^2$. Indeed, Eq. (4), which is equivalent to the heuristic Eq. (1), can be written in a form analogous to Eq. (9):

$$\kappa\mathcal{L} = \sqrt{\frac{\tau^3}{\nu_{\rm eff} H}} \cdot V^{3/2}. \tag{10}$$

Proportionality between $\mathcal{L}$ and $V^{3/2}$ has been reported in a narrow temperature range around 1.55 K [16]. We note also however, that a study [24] with bellows-driven He-II and second-sound pulse probe yielded $\mathcal{L} \sim V^p$, with p displaying a significant temperature dependence from 1.3 at 1.5 K to 0.9 at 2.0 K. In the present work instead, proportionality between $\mathcal{L}$ and $V^{3/2}$ is found from 1.17 up to 2.16 K in runs with and without grid (see Fig. (2)). This result can therefore be interpreted as a strong direct evidence of the validity of Eq. (1) if we take for granted that τ and H are independent of Reynolds number and temperature, which is generally admitted in classical turbulence [19] and has been verified in superfluid grid turbulence down to ~ 1.6 K [5]. Noteworthily, proportionality is verified down to Re_κ of order 1; this observation is consistent with the surprising ability of Eq. (9) to account for the decay of turbulence down to very low Re_κ.

On the accuracy in the determination of $\nu_{\rm eff}$. – Accuracy in determination of $\nu_{\rm eff}$ from decay and steady-state experiments is limited by uncertainties in H and τ in Eqs. (9) and (10). In decay experiments, the saturated value of H has to be estimated from the container size D i.e. the channel width, which implies some modeling of flow at large scales. This is often done using the model proposed in [12] which assumes that, in the late decay, a Kolmogorov energy spectrum $E(k) = C_k\epsilon^{2/3}k^{-5/3}$ extends up to the scale $k = 2\pi/D$ where it is truncated abruptly, which leads to Eq. (9) with $H = D(3C_k)^{3/2}/2\pi \simeq 1.5D$ (where $C_k \simeq 1.5$ is the Kolmogorov constant). This model does not account for second-order effects, such as the anisotropy resulting from the saturation on the container walls, the geometrical shape of the container, the triadic interactions around $k = 2\pi/D$, etc. If we assume uncertainty on H/D of a factor 2, the resulting uncertainty on $\nu_{\rm eff}$ is a factor 4. In the steady-state approach, both H and τ have to be estimated to determine $\nu_{\rm eff}$ from Eq. (10). In the present experiment, the uncertainty is typically a factor of 2.5 for H and a factor of 1.5 for τ, so the resulting uncertainty on $\nu_{\rm eff}$ can wind up to a factor of about 8. Moreover, both for the decay and steady-state approaches when the second-sound attenuation technique is used, $\mathcal{L}$ suffers intrinsic uncertainties of order 30% due to unknown vortex tangle distribution [17], and for our steady-state experiment an additional underestimation of $\mathcal{L}$ of order 30% is due to a denser distribution of vortex lines near the walls where the fundamental second-sound resonant mode used here is less sensitive. Cumulatively, uncertainties on L, τ and H can lead to an uncertainty on $\nu_{\rm eff}$ up to a factor of 10. These estimations illustrate the challenge of obtaining accurate experimental values of $\nu_{\rm eff}$. At any rate, a favourable constraint for the tuning of H and τ is that $\nu_{\rm eff}$ is expected to join the known value of viscosity of He-I $\nu \cong 0.167\kappa$ across the λ-point, assuming that $\kappa\mathcal{L} \to \langle|\omega_{\rm n}|^2\rangle^{1/2}$ for $T \to T_\lambda$. The accuracy could be improved by directly measuring velocity statistics at large scales for more direct inference of H and τ.

In Fig. 4 (top), $\nu_{\rm eff}/\kappa$ is obtained by fitting Eq. (10) to the data in Fig. 2 using H and τ as for Fig 3. Here error bars only reflect uncertainty on relative temperature dependence. We also show values of $\nu_{\rm eff}$ deduced from the Oregon [25] and recent Prague decay experiments [26]. The latter are significant because these are decay measurements of the flow which yielded the steady-state grid data: they are performed in the same channel, and during the same run. Given the difficulty in obtaining accurate values of $\nu_{\rm eff}$, the experiments can be considered in relatively good agreement with each other, and in the light of the almost factor 10 uncertainty, the agreement can be regarded as rough but real with the simulation too, in particular for the adjustable parameter $r \simeq 2.4$.

On the temperature dependence of $\nu_{\rm eff}$. – A comparison of the temperature dependencies is delicate because: (i) we lack experimental proof that H and τ are truly temperature independent; (ii) the experimentally observed temperature dependence of the vortex tangle polarization [27] may affect $\nu_{\rm eff}$ via Eq.(1) in ways unaccountable by the models; (iii) the pronounced frequency dependence of the mutual friction parameter $B(T)$, known to exhibit a two-fold variation from 1 Hz to 10 kHz for $1.2 < T < 2$ K [28], is ignored in the numerics and models where we chose intermediate values of B. Bearing this in mind, we shall now discuss Fig. 4 (bottom), where an arbitrary vertical offset is applied to the data in the top

panel, to focus on the temperature dependence.

In the range $1.35\,K \leq T \leq 2.05\,K$ the temperature dependence from all results exhibits no significant difference within the scatter of points. For $T \gtrsim 2$ K, the sharp increase of $\nu_{\rm eff}(T)$ seen in the simulations is not found in experiments. This discrepancy is not understood. At low temperature, some datasets experience a drop of $\nu_{\rm eff}$ compatible with the mutual-friction dissipation model (see simulations and Oregon decay experiment) while the Prague experiments found no significant temperature dependence, in particular in the steady-state case. We have no explanation for this disagreement, but we note that it almost vanishes if the steady-state grid datapoint at 1.17 K is ignored, despite we found no sufficient reason to experimentally distrust it. Further pressure on this datapoint comes from the fact that as the temperature is lowered below 1 K, $\nu_{\rm eff}$ is known to drop further, as deduced from the Manchester turbulence decay experiments [29], which yielded $\nu_{\rm eff}/\kappa \approx 3 \times 10^{-3}$ in the $T \to 0$ limit.

Conclusions. – We have explored the concept of effective kinematic viscosity in steady-state turbulent He-II by experimental and numerical means, within $1.17\,\mathrm{K} \leq T \leq 2.16\,\mathrm{K}$. Our channel flow experiments revealed a robust scaling of vortex line density with mean flow velocity of the form $\mathcal{L} \propto V^{3/2}$, holding upon changing ρ_s/ρ_n by a factor 450. From this we inferred the validity of the heuristic definition of the effective viscosity, $\epsilon = \nu_{\rm eff}\,(\kappa\mathcal{L})^2$. The new values of $\nu_{\rm eff}$ deduced from our steady-state approach are consistent with known values deduced from decaying turbulence if we consider that an accurate determination of $\nu_{\rm eff}$ is in fact very difficult, both in decaying and steady-state turbulence, due to uncertainties in flow properties at large scales. This could be overcome in the future by exploring steady-state flows with well-known velocity statistics at large scales. Numerical simulations yield $\nu_{\rm eff}$ consistent with measurements in the range $1.35 \lesssim T \lesssim 2.05$ K. Outside this range the temperature dependence of simulations is steeper, requiring dedicated studies at these temperature extremes. The temperature dependence produced by the simulations can be usefully interpreted as a dissipative cross-over from a high temperature regime, where normal viscosity is the main dissipative process, to a low temperature regime where mutual friction becomes a significant one. This suggests that the temperature dependence $\nu_{\rm eff}(T)$ of turbulent He-II is an indicator of dissipation mechanisms. One contribution of this paper is to open the way for the determination of $\nu_{\rm eff}$ from a steady-state approach, making use and further validating governing equations already employed in analysis of QT decay.

* * *

We are grateful to the Ens de Lyon for providing access to PSMN computing center, supported by the Région Rhône-Alpes (CPER-CIRA) and EQUIP@MESO. E.V. and L.S. acknowledge grants GAČR 203/14/02005S and GAUK 366213, and P.-E.R. grant ANR-09-BLAN-0094.

REFERENCES

[1] Vinen W. F. and Niemela J. J., *J. Low Temp. Phys.* , **128** (2002) 167.
[2] Skrbek, L. and Sreenivasan, K. R., *Phys. Fluids 24*, **2012** (011301) .
[3] Nemirovskii S. K., *Physics Reports* , **524** (2013) 85.
[4] Fuzier S., Baudouy B. and Van Sciver S. W., *Cryogenics* , **41** (2001) 453.
[5] Salort J. *et al.*, *Phys. Fluids* , **22** (2010) 125102.
[6] Niemela J. J., Sreenivasan K. and Donnelly R. J., *J. Low Temp. Phys.* , **138** (2005) 537.
[7] Walmsley P. M. and Golov A. I., *Phys. Rev. Lett.* , **100** (2008) 245301.
[8] Chagovets T. V., Gordeev A. V. and Skrbek L., *Phys. Rev. E* , **76** (2007) 027301.
[9] Skrbek L. and Sreenivasan K. R., *Chapter 10 in Ten chapters of turbulence* (Cambridge University Press) 2013.
[10] Kondaurova L. and Nemirovskii S. K., *Phys. Rev. B* , **86** (2012) 134506.
[11] Smith M., Donnelly R. J., Goldenfeld N. and Vinen W. F., *Phys. Rev. Lett.* , **71** (1993) 2583.
[12] Stalp S., Skrbek L. and Donnelly R. J., *Phys. Rev. Lett.* , **82** (1999) 4831.
[13] Vinen W. F., *Phys. Rev. B* , **61** (2000) 1410.
[14] Skrbek L., Niemela J. J. and Donnelly R. J., *Phys. Rev. Lett.* , **85** (2000) 2973.
[15] Tennekes H. and Lumley J. L., *A first Course in Turbulence* (The MIT Press) 1994.
[16] Salort J., Roche P. E. and Leveque E., *Europhysics Lett. 94*, **2011** (24001) .
[17] Babuin S., Stammeier M., Varga E., Rotter M. and Skrbek L., *Phys. Rev. B* , **86** (2012) 134515.
[18] Lumley J. L. and McMahon J. F., *ASME J. Basic Eng.* , **89D** (1967) 764.
[19] Roach P. E., *Int. J. Heat and Fluid Flow* , **8** (1987) 83.
[20] Comte-Bellot G. and Corrsin S., *J. Fluid Mech.* , **48** (1971) 273.
[21] Salort J., Chabaud B., Leveque E. and Roche P. E., *Europhysics Lett. 97*, **2012** (34006) .
[22] Samuels D. C. and Kivotides D., *Phys. Rev. Lett.* , **83** (1999) 5306.
[23] Orszag S. and Patterson G., *Phys. Rev. Lett.* , **28** (1972) 76.
[24] Holmes D. S. and Van Sciver S. W., *J. Low Temp. Phys.* , **87** (1992) 73.
[25] Niemela J. J., Sreenivasan K. R. and Donnelly R. J., *J. Low Temp. Phys.* , **138** (2005) 534.
[26] Babuin S., Varga E. and Skrbek L., *J. Low Temp. Phys.* , (2013) .
[27] Wang R. T., Swanson C. E. and Donnelly R. J., *Phys. Rev. B* , **36** (1987) 5240.
[28] Swanson C. E., Wagner W. T., Donnelly R. J. and Barenghi C. F., *J. Low Temp. Phys.* , **66** (1987) 263.
[29] Golov A. I. and Walmsley P. M., *J. Low Temp. Phys.* , **156** (2009) 51.